The spectral energy distribution of polars

vorgelegt von
Diplom-Physiker
Justus Vogel
aus Königs Wusterhausen

Von der Fakultät II – Mathematik und Naturwissenschaften
der Technischen Universität Berlin
zur Erlangung des akademischen Grades

Doktor der Naturwissenschaften
– Dr. rer. nat. –

genehmigte Dissertation

Promotionsausschuss:

Vorsitzender: Prof. Dr. Hans-Joachim Eichler
Berichter: PD Dr. A. Schwope
Berichter: Prof. Dr. E. Sedlmayr

Tag der wissenschaftlichen Aussprache: 10. Juli 2008

Berlin 2008

D 83

Zusammenfassung

Magnetische kataklysmische Veränderliche, nach ihrem Prototypen auch AM Her Sterne genannt, sind enge Doppelsternsysteme mit Materietransfer (Akkretion), bestehend aus einem Hauptreihenstern späten Spektraltyps und einem schwereren Weißen Zwerg mit starkem Magnetfeld. Der Massetransfer findet vom Hauptreihenstern auf den Weißen Zwerg statt. Während die überfließende Materie zuerst einer ballistischen Bahn folgt, wird sie im weiteren Verlauf vom Magnetfeld eingefangen und entlang der Feldlinien auf den Weißen Zwerg geleitet. Die dabei freigesetzte Gravitationsenergie wird in Wellenlängenbereichen vom Infraroten bis zum Röntgen abgestrahlt. Das beobachtbare Licht eines AM Her Sternes ist zusammengesetzt aus dem Licht der beiden Sternkomponenten und der in der Akkretionssäule und der Akkretionsregion auf dem Weißen Zwerg freigesetzen Strahlung. Die Beiträge der beiden letzteren Strahlungskomponenten sind nicht nur von der aktuellen Akkretionsrate abhängig, sondern auch von der räumlichen Orientierung des Magnetfeldes. Da das Magnetfeld mit dem Weißen Zwerg rotiert und dieser synchron mit dem Doppelsternsystem, führt dies gewöhnlich zu einer starken Veränderung des beobachtbaren Lichtes während einer Umdrehung des Doppelsternsystems. Die Zerlegung des beobachtbaren Lichtes in die Bestandteile der verschiedenen Komponenten ermöglicht dem Beobachter die einzelnen Komponenten dieses Systems zu analysieren.

In dieser Arbeit wird genau diese Zerlegung für drei AM Her Sterne vorgenommen. Für WX LMi konnte durch die Analyse der Beiträge des Weißen Zwerges gezeigt werden, daß dieses Doppelsternsystem ein Vorläufer eines normalen AM Her Sternes ist. Der Röntgenbeitrag konnte in die Beiträge des Hauptreihensternes und des Akkretionsplasmas zerlegt werden und offenbarte einen röntgenaktiven Hauptreihenstern. Der Beitrag des Akkretionsplasmas im Röntgen und im Optischen diente der Überprüfung aktueller Akkretionsmodelle für geringe Akkretionsraten. Für den neu entdeckten AM Her Stern 2XMM1312 wurden erstmalig optische und Röntgenbeobachtungen analysiert und daraus die Parameter des Systems bestimmt. 2XMM1312 zeigte sich als einer der wenigen AM Her Sterne mit einer ungewöhnlichen Energieverteilung im Röntgenbereich. Für das AM Her System HU Aquarii wurden aus optischen hoch zeitaufgelösten Beobachtungen die Parameter des Systems mit hoher Genauigkeit neu bestimmt. Dies ermöglichte im weiteren ein Absinken der Orbitalperiode des Doppelsternsystems nachzuweisen. Es konnte gezeigt werden, daß dieses Absinken wesentlich stärker ist, als man es nach den Standardmodellen für die zeitliche Entwicklung von AM Her Sternen anhand des Drehimpulsverlustes erwartet. Mögliche andere Erklärungen werden diskutiert. Es wird weiterhin ein Programm vorgestellt , welches

entwickelt wurde, um aus dem bereits separierten Beitrag des Weißen Zwerges eine Temperaturverteilung auf seiner Oberfläche zu bestimmen.

Abstract

Magnetic cataclysmic variables, also called AM Her stars or 'polars', are close binaries with mass transfer (accretion), consisting of a late-type main-sequence star (commonly called *secondary*) and a more massive white dwarf with a strong magnetic field. The late-type star is losing mass to the white dwarf. The overflowing matter firstly follows a ballistic trajectory and is then captured by the magnetic field of the white dwarf and guided along the field lines onto the white dwarf. The released gravitational energy is radiated away in all wavelength ranges from infra-red to X-ray. The observed light of an AM Her system is composed of the contributions from the stellar components and the contributions of the accretion column and the accretion region on the white dwarf. The last two components are not only depending on the actual mass transfer rate but also from the spatial orientation of the magnetic field. Since the white dwarf is locked in synchronous rotation, this leads to emission that varies with orbital phase. The decomposition of the observed light from an AM Her system makes it possible to analyse the different components within this system.

This work presents the decomposition for three AM Her stars. For WX LMi the analysis of the white dwarf contribution revealed the system as a progenitor of normal polars. The X-ray emission was decomposed into the contributions of the late-type star and the contribution of the accretion plasma and showed an X-ray active secondary. The contribution of the accretion plasma in X-rays and in the optical could be used to test predictions of accretion models for low accretion rates. For the newly discovered polar 2XMM1312 X-ray and optical observations were analyzed and the system parameters derived. 2XMM1312 is one of a few AM Her systems which exhibit an unusual energy distribution in the X-ray regime. For the AM Her HU Aquarii high-speed photometry was used to redetermine the system parameters with high accuracy. This could be used to measure a significant orbital period decrease. According to the standard model of the AM Her evolution an angular momentum loss and thus a period decrease is expected. It could be shown that the observed period decrease is larger than the predicted period decrease. Possible explanations are discussed. Furthermore a code is presented, which was developed to derive a temperature distribution of the white dwarf surface from observations showing the naked white dwarf.

Contents

Contents

List of Figures

List of Tables

Chapter 1

Introduction

1.1 Polars or magnetic cataclysmic variables

Cataclysmic variables (CVs for brevity) are close binaries consisting of a white dwarf and a less massive red dwarf, with the red dwarf losing matter via Roche-lobe overflow. The term "*cataclysmic*" comes from the greek word "*κατακλνσμος*" meaning "*Flood*" and refers to the mass transfer from the donor star onto the white dwarf and the observable outcome of this mass tranfer – namely regular or irregular outbursts in brightness due to the matter being accreted. The orbital period of cataclysmic variables ranges from 1.3 hours to two days, with a significant lack of systems with orbital periods between 2 and 3 hours, the so-called *period gap*. The reasons for this gap are discussed in Sect. 1.6.

The actual observable characteristics of the outbursts are used as the criterion to classify the different types of CVs. There are mainly four classes of CVs, each with various subclasses: classical Novae (CN), dwarf Novae (DN), recurrent Novae (RN) and nova-like variables (NL). A comprehensive overview of the different types can be found in Warner (1995).

The underlying reasons for the different observable features are differences in the structure and physical properties of the binary components. One of the main differences is the existence or absence of a magnetic field of the white dwarf. Without a magnetic field the overflowing matter forms an accretion disc around the white dwarf, where it can lose angular momentum and finally settle down onto the white dwarf. Instabilities of the accretion disc or the ignition of H-burning in the accreted matter onto the white dwarf then lead to the mentioned outbursts in brightness. If the white dwarf possesses a magnetic field the overflowing matter is affected by this field. With increasing field strength the accretion disc is more and more truncated and for sufficiently high field strengths the formation of an accretion disc is totally prevented. Instead the overflowing matter is caught by the magnetic field and guided along the field lines onto the white dwarf. An artistic illustration of such a system is shown in Fig. 1.1. These magnetic cataclysmic variables belong to the class of nova-like variables (NL). If the spin of the white dwarf is synchronized with the orbital period of the binary these systems are called – after its prototype – AM Her systems or –
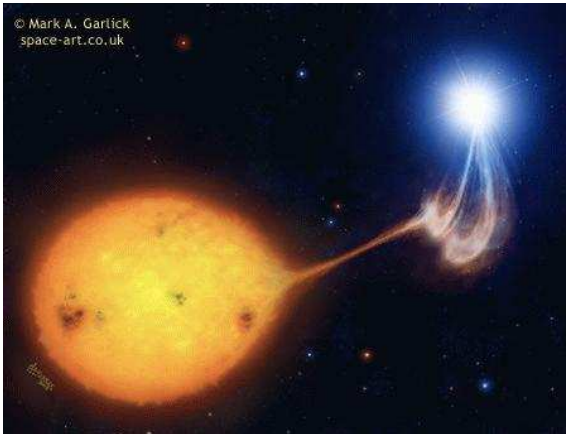
Figure 1.1:
Artists impression of an AM Her
System (by Mark Garlick). Matter
streams-off from the late-type donor
star following a ballistic trajectory,
is then caught by the magnetic
field forming a fragmented magnetic
stream and finally falls onto the
white dwarf, generating a high ac-
cretion luminosity.

after the polarized radiation from the accretion region – polars (Krzeminski & Serkowski
1977). The field strength of the white dwarf ranges from 7 MG up to more than 200 MG.
Nearly 90 AM Her systems are known today, forming a fraction of more than one tenth of
all CVs.
Cataclysmic variables of AM Her type are the leading actors of this work and are introduced
in more detail in the following sections. Fig. 1.2 illustrates the conventions used for
the spatial coordinates and angles inside an AM Her system and Fig. 1.3 illustrates the
gravitational potential of a binary system and the important Roche-lobe (named after
Edouard Roche (1820-1883), a French mathematician).

1.2   The accretion process

Accretion is the main observable feature of polars and turns them into highly variable
sources in all wavelength ranges. A schematic sketch of a typical accretion scenario is
provided in Fig. 1.4. The effluent matter from the donor star follows initially a ballistic
trajectory. This part of the accretion stream is called *ballistic stream*. With decreasing
distance to the white dwarf the magnetic pressure becomes more and more important
compared to the ram pressure of the ballistic stream and affects shape and density profile
of the accretion stream. Due to arising Kelvin-Helmholtz and Rayleigh-Taylor instabilities
the stream gets fragmented (Kuijpers & Pringle 1982, Frank et al. 1988) and couples over
a more or less extended range in azimuth to the magnetic field. This coupling region is
commonly called *threading region*.
The plasma now follows the magnetic field lines and is – not surprisingly – termed *magnetic
stream* or if it is extended in azimuth *accretion curtain*. Depending on the actual orientation
and strength of the magnetic field the plasma is guided onto one or both magnetic poles.
Both scenarios are observed. The released gravitational energy is converted into kinetic
energy, the plasma accelerated to a velocity of several thousand kilometers per second.
The gyrating plasma particles cause strong cyclotron emission in the infra-red, optical and
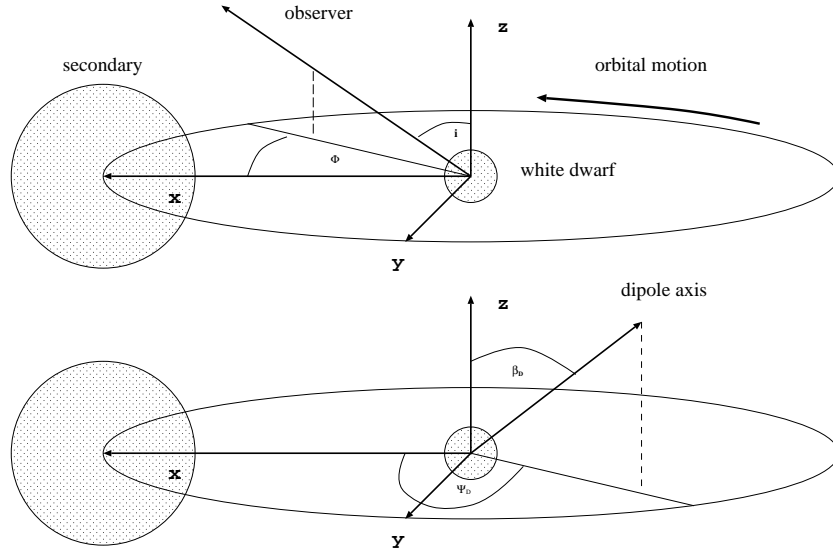
Figure 1.2:
This figure illustrates the commonly used definition of coordinates systems in AM Her stars. The upper panel shows phase angle Φ and inclination i. The lower panel shows azimuth Ψ_D and colatitude β_D.

ultraviolet wavelength range. The supersonic infalling plasma leads to a hydrodynamic stand-off shock front above the white dwarf surface (≤ 0.1 R_{WD}). The cooling plasma in the post-shock region emits bremsstrahlung in the hard X-ray regime. The temperatures in the post-shock region are mainly of the order of 10 - 40 keV (10^7 - 10^8 K). The accretion region on the white dwarf is called "hot spot". Its geometry and size depends on the magnetic field. In general the size decreases with increasing magnetic field strength. A fraction of the hard X-rays and the cyclotron radiation is absorbed by the photosphere of the white dwarf, re-processed and re-radiated in the soft X-ray regime. This leads to a heating of the white dwarf photosphere in the vicinity of the accretion spot. The size and location of this so-called "pole cap" depends on the orientation of the accretion column (with respect to the white dwarf surface) and the height of the shock, i.e. the white dwarf mass M_{WD}, the specific mass accretion rate $\dot{m}$ and the magnetic field strength B. The spectrum of the soft X-ray component can be described best with a black body with typical temperatures in the range 15 - 40 eV (10^4 - 10^5 K). A schematic sketch of an accretion column is provided in Fig. 1.5.

The standard accretion model (King & Lasota 1979, Lamb & Masters 1979) predicts roughly equal luminosities for the cooling accretion plasma, i.e. bremsstrahlung and cyclotron component, and the re-processed soft component. This raised problems, since the observed energy content of the soft component turned out to be much larger. The excess of the soft component – the "soft X-ray puzzle" – is hard to understand in terms
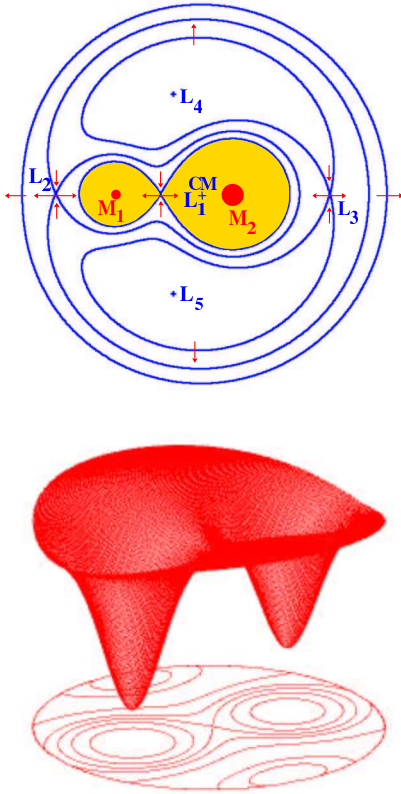
Figure 1.3: Illustration of the gravitational potential of a binary system, assuming two point masses with ($M_1 < M_2$). *Top*: Equipotential lines in the orbital plane. The yellow sections indicate the Roche-lobe for each of the point masses. A particle inside the Roche-lobe belongs exclusively to one of the stars. Outside the Roche-lobe the particle is subjected to the gravitational forces of both stars. The Lagrangian points L_1 to L_5 indicate points of metastable equilibrium. At L_1 the gravitational forces of both stars are equal, this is the location where the mass transfer from one star to the other happens, the so-called Roche-lobe overflow. L_4 and L_5 indicate local minima of the gravitational potential, where the gradient of the potential equals zero. Particles outside L_2 and L_3 can escape from the system – since the centrifugal forces outbalance the gravitational forces. *Bottom*: Three-dimensional illustration of the gravitational potential (at bottom the two-dimensional projection). The potential minima at the locations of the point masses are truncated (Podsiadlowski 2004).

of a white dwarf atmosphere heated by radiation from the standard accretion column. Kuijpers & Pringle (1982) proposed a *"blobby accretion"* scenario for the case of high mass flows ($\dot{m} \geq 10\frac{g}{cm^2s}$) and low field strength, where the accretion stream is fragmented into *blobs* due to interaction with the magnetic field. Confinement and compression of these blobs lead to buried shocks inside the atmosphere of the white dwarf. The hard bremsstrahlung is released in sub-photospheric layers, heating the atmosphere from below. The reprocessed energy is re-radiated in the soft X-ray regime and the EUV. For the case of low mass flows ($\dot{m} \leq 1\frac{g}{cm^2s}$) and high field strength the *"bombardment solution"* was proposed (and later numerically treated by Woelk & Beuermann 1996). For low specific mass accretion rates cyclotron cooling becomes so efficient that a hydrodynamic shock is inhibited, thus suppressing the hard bremsstrahlung component. With increasing $\dot{m}$ a shock front forms and the cooling process becomes more and more dominated by bremsstrahlung. Both ideas are confirmed by ROSAT observations of polars, which show a correlation between the soft X-ray excess and the magnetic field strength of the white dwarf.

Other explanations (Cropper et al. 2000, Ramsay et al. 2001) suggest that the simplified modeling of the post-shock region with one-temperature plasma models accounts for the soft X-ray excess. This excess is here an apparent excess, since a fraction of the soft com-
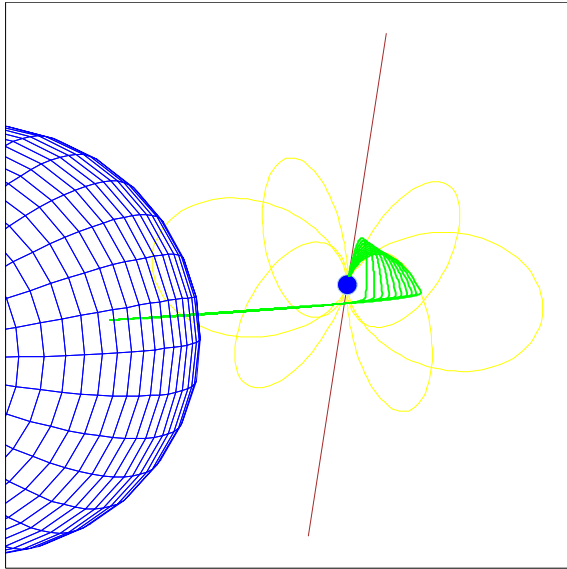
Figure 1.4:
Schematic sketch of the accretion stream in polars for an one pole accretion scenario. The accretion stream (green) firstly follows a ballistic trajectory and is then gradually caught by the magnetic field and guided onto the white dwarf. Field lines are shown in yellow, the magnetic dipole axis in red. Orientation of magnetic field and coupling points of the ballistic stream are chosen arbitrarily.
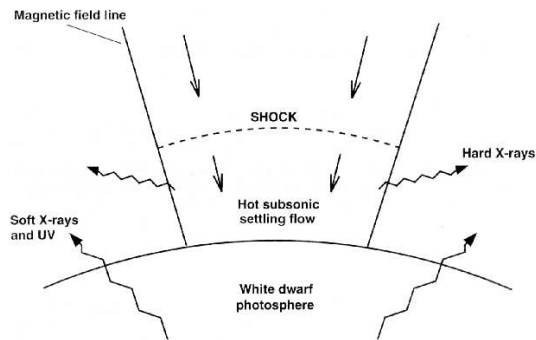
Figure 1.5:
A homogeneous accretion column above the surface of the white dwarf showing the origin of the hard and soft component. From King (1995)

ponent is not of re-processed origin, but originates in the lowest layers of the post-shock region. This is not taken into account correctly when using one-temperature models.

On a timescale of years down to weeks the accretion in polars switches between *high states* of accretion and *low states* of accretion with a considerably reduced brightness of the system in all wavelength ranges compared to a high state. The change can be abrupt or involve an *intermediate state* of accretion. There is no periodicity and the state of accretion can not be predicted for a given date. The reasons for the different accretion states are not clear. A change in radius of the donor star can be excluded, since the time-scale is much longer (10^4 - 10^5 yr), but possible explanations involve irradiation of the donor star by the hot spot (King 1989) or star spots on the donor star (Livio & Pringle 1994, King & Cannizzo 1998, Hessman et al. 2000). While in the former case an ionisation front below the L1 point causes a change of the mass transfer rate, in the latter case star spots below the L1 points lead to a cooler and thus less dense local photosphere, decreasing the mass transfer rate.

1.3   The white dwarf

Although white dwarfs belong to the well-known objects in the sky, the very special environment and evolution of CV white dwarfs separates them from isolated white dwarfs. It is important to know about the differences between single white dwarfs and accreting CV white dwarfs.

The prime difference compared to an isolated white dwarf is the accretion of matter from the donor star. This leads to a heating of the white dwarf and thus a change in cooling time. The temperature is the key for determining the age of the white dwarf. If the temperature of the white dwarf is used to set constraints on the evolutionary time-scale of polars, one has to account for the additional heating of the white dwarf.

The white dwarf gains energy due to different processes: Firstly, absorption of radiation from the accretion column (or accretion spot on the accretion disc) and, secondly, the release of gravitational energy from the matter being accreted. Both processes lead to a heating of the white dwarfs photosphere. The time-scale for re-radiation of this energy is not well constrained – after entering a low state of accretion the accretion spot in some systems remains visible for a long time into the low state, in some systems it vanishes with the end of the high state (Sion 1999) – but it is considerably shorter than the time-scale for entering and heating the white dwarf core (Townsley & Bildsten 2002). The main driver for the heating of the white dwarf is compressional heating – the gravitational energy release of the white dwarf due to the increase in mass from the matter being accreted (Sion 1995). Indeed there are no polars observed with white dwarf temperatures below ∼11000 K (Gänsicke 2000), while single white dwarfs with much lower temperatures can be observed. This subject is further addresses in Chapter 2.

Concerning the temperature another problem arises in polars. For non-magnetic isolated white dwarfs the spectra can be reproduced by theoretical models with high accuracy (Koester 2002), at least if one ignores the low temperature white dwarfs, making it possible to determine the effective temperature and g of the white dwarf very reliably by fitting hydrogen absorption line profiles and continuum with model spectra. For the white dwarfs in polars the spectrum is contaminated by contributions from the accretion stream. Furthermore the white dwarf in polars is magnetic by definition. Thus the Stark broadening of the lines is affected by the individual Zeeman components of the lines. Both facts complicate the temperature determination of polar white dwarfs.

Other differences between isolated white dwarfs and white dwarfs in polars are less obvious or it is unclear if there is a difference at all. For interacting binary systems the stellar parameters can very often not be determined independently. One has to assume certain parameters derived from single stars. One of these parameters is the mass of the white dwarf. While the continuous accretion of matter leads to an increase of the white dwarf mass, every Nova eruption removes more mass from the white dwarf than has been accreted before. The bottom line is that CV white dwarfs should be less massive than single white dwarfs. But this can not be confirmed by observations.
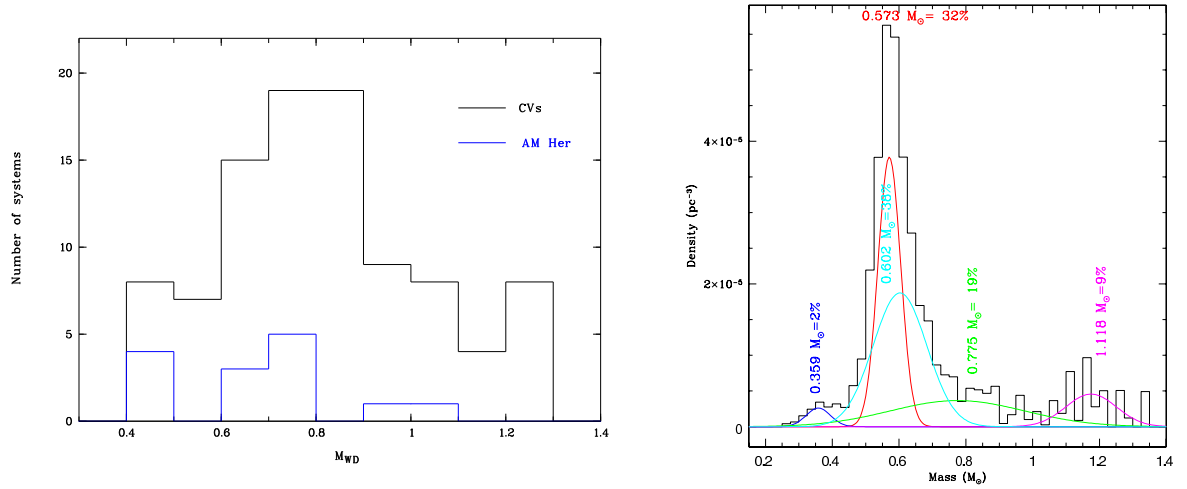
Figure 1.6: *Right*: White dwarf mass distribution for a volume corrected sample of 1733 DA white dwarfs from Sloan DR4 with g > 19 and T_{eff} > 12000 K (Kepler et al. 2007). *Left*:White dwarf mass distribution with a binning of 0.1 $M_\odot$ for 99 CV white dwarfs with determined masses out of 672 from the Ritter & Kolb catalog RKcat7.8 (Ritter & Kolb 2003). Despite statistically non-significant the 14 AM Her white dwarfs with known masses are overplotted in blue.

The mass of isolated (non-magnetic) white dwarfs clusters strongly at ∼0.6 $M_\odot$. Fig. 1.6 (right panel) shows the mass distribution of a sample of more than 1700 DA white dwarfs from the Sloan Digital Sky Survey (Kepler et al. 2007). The sample is limited to white dwarfs with T_{eff} > 12000 K. Several studies suggest an increase in the mean mass for lower temperatures, but this result is ambiguous and it is still an open question if this trend reflects physical reality or problems with the theoretical model spectra.

The mass of CV white dwarfs (Fig. 1.6 - left panel), shows a broader distribution without a sharp peak and a maximum of systems between 0.7 and 0.9 $M_\odot$. There are also studies which identify different mean masses for systems below and above the period gap (Smith & Dhillon 1998), but all of these studies have to be interpreted cautiously due to the low number of systems.

1.4 The secondary

The donor star in cataclysmic variables, often simply called secondary, is a main-sequence-like low-mass star of late spectral type. The term "main-sequence-like" reveals already the main problem concerning the secondary. A lot of effort was made to solve the question, if the secondary in CVs is comparable to single main-sequence stars. This is a crucial question since it decides if the theoretical and empirical knowledge about single main-sequence stars can be applied to the – comparatively – small sample of CV secondaries. While for the white dwarf at least the interior structure remains the same as for single white dwarfs, this

Figure 1.7: Spectral type-orbital period relation for CVs secondary stars (blue points) and main-sequence stars (red points). The dashed line is a theoretical relation for main-sequence stars from Baraffe et al. (1998). The large deviations for $P_{orb} > 6$h can be explained with nuclear-evolved donor stars. The figure is taken from Knigge (2006).
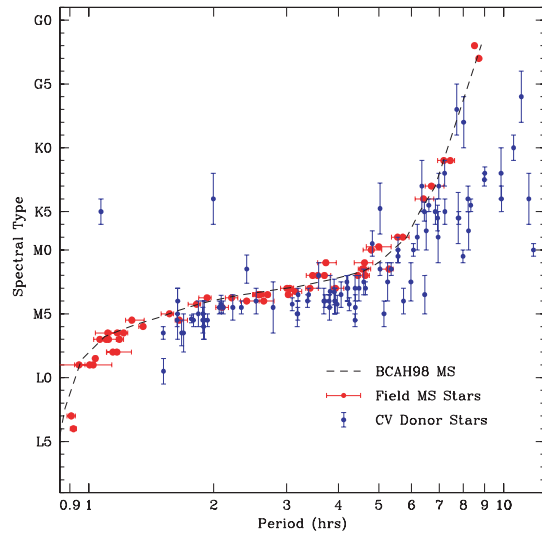
is not evident in advance for the secondary. Compared to single stars the donor stars in CVs are:

- deformed (Roche-shaped)

- fastly rotating

- irradiated from a hot source within $\sim 1R_\odot$

- donating mass

How do these processes influence the stellar structure of the star?

The fast rotation and the tidal forces lead to observable features, like ellipsoidal variations in light curves due to a different projected size of the secondary at different orbital phases, but can be neglected for the interior stellar structure (Kolb & Baraffe 1999). Likewise the irradiation from the hot accretion spot can be neglected for the interior stellar structure, while for the atmosphere it can not (Beuermann 2000 and references therein). The observable consequences of irradiation are a decrease of the TiO band and Na I absorption lines strength – feigning a later spectral type. For an unambiguous analysis of a spectrum one should know about the observed orbital period. The (K band) continuum – important for determining distances – is hardly affected by irradiation.

The remaining and most essential point is the mass loss. Applying relations valid for single stars to CV secondaries (e.g. a mass-radius relation) implicitly assumes that the mass donating star is in thermal equilibrium. This is true, if the thermal time-scale is much shorter than the mass-loss time scale. Otherwise the CV secondary is out of thermal balance and oversized compared to a single star of the same mass.

Comparing single stars and CV secondaries means comparing directly or indirectly observed quantities. While mass and radius of the secondary in CVs are mostly ill-determined,

a well-determined quantity is the spectral type. Therefore a spectral type - orbital period relation, with the orbital period constraining the mass-radius relation, has been established as the benchmark in the last decade (see Fig. 1.7). For the single stars the orbital period is obviously a virtual one. According to its mass and radius the orbital period of the corresponding semi-detached binary system with the star as the Roche-lobe filling component is assigned to the single star. This is possible with only small uncertainties since the orbital period is only weakly dependent on the mass ratio and thus the fictive companion. While former explorations found a congruence between single stars and CV secondaries for orbital periods $P_{orb} < 7$ h (Smith & Dhillon 1998) or $P_{orb} < 3$ h (Beuermann et al. 1998), newer investigations found a consistently later spectral type of the secondary at all orbital periods, with a deviation in spectral type in the right order to reflect the radius expansion due to the mass loss (Knigge 2006).

1.5 Spectral energy composition

The broad-band spectral energy distribution of AM Her systems is a composite of contributions from the donor star, the white dwarf, the accretion stream, the accretion column above and the hot spot on the white dwarf surface. Not all of these emission sources contribute at all wavelengths, but all components are modulated with the orbital phase of the systems and contribute varying with the accretion state. Disentangling the different components in the observational data is often the most challenging – but also most promising – approach when analyzing the data.

The secondary is often the faintest component. Due to the late spectral type, i.e. the low effective temperature, it contributes mainly in the infra-red. Since the shape of the secondary is Roche-deformed (by tidal forces), its contribution is modulated with the projected size of the star, although this modulation is often hard to detect. A possible contribution of the secondary in X-rays is also possible and discussed in detail in Chapter 2.

The white dwarf, including the heated pole cap, contributes to the optical und ultraviolet. While the contribution to the optical is often outshone by the much brighter accretion stream, it is an appreciable emission source in the far UV, even during high states. While the contribution of the white dwarf itself is independent from the actual orbital phase, the contribution of the heated pole cap – or both pole caps in the case of a two pole accretion scenario – is not. It is modulated with its geometrical visibility, where the highest contribution occurs when it is directly exposed towards the observer.

The accretion stream emits also in the optical and UV. Its contribution depends strongly on the accretion state. While it can be disregarded in a low state it cannot be neglected in a high state. Emission from the accretion stream is strongly modulated with the orbital phase, but can hardly be modeled since the actual shape of the stream is highly uncertain
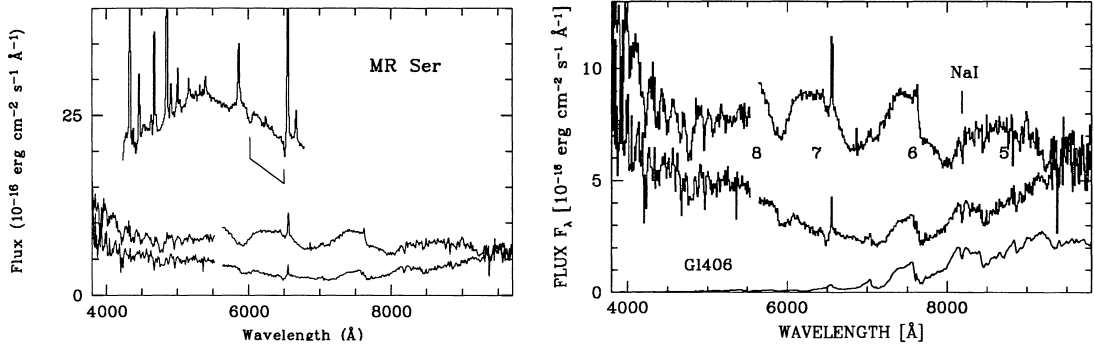
Figure 1.8:
Optical spectra of the AM Her MR Ser. *Left*: From top to bottom: high state at bright phase, low state at bright phase, low state - same orbit as before - at faint phase. *Right*: Zoomed version of the two low state spectra from the left figure. The numbers indicate the cyclotron harmonics. The lowest spectrum is a suitably scaled M6 spectrum. From Schwope (1995).

and the optical depth and thus the modulation with orbital phase vary for the different emission components and depend on the actual mass accretion rate.

The cyclotron component originating from the cooling plasma is the most prominent feature of AM Her systems in the optical regime and the reason why they are called polars. For the common magnetic field strength in polars the cyclotron fundamental is at infrared wavelength. The cyclotron harmonics extend the contribution into the optical and ultraviolet. The energy distribution over the individual harmonics depends on the plasma temperature and field strength. For higher temperature and higher kinetic energy the cyclotron radiation is shifted towards the higher harmonics. Cyclotron radiation is non-isotropic. It is strongest when the line of sight is perpendicular to the magnetic field lines (*"cyclotron beaming"*). This beaming property is amplified in the higher harmonics. Cyclotron radiation is also polarized, circularly along the field lines, linearly perpendicular to the field lines. Circularly polarized radiation is mostly emitted in lower harmonics while the linearly polarized radiation is emitted primarily in the higher ones.
In short, the observed cyclotron component depends strongly on the current angle between observer and field lines and the observed band pass, but its strong orbital phase dependent modulation is more a boon than a bane, since the position and width of the individual harmonics, the ratio between the harmonics, and the polarized components provide a wealth of information about the magnetic field, its strength and orientation. Obviously the cyclotron harmonics can only be observed for optically thin emission. Therefor they are more pronounced in low accretion states. For high mass accretion rates the cyclotron emission becomes optically thick.
Fig. 1.8 examplarily shows optical spectra of MR Ser of a high and low state for different
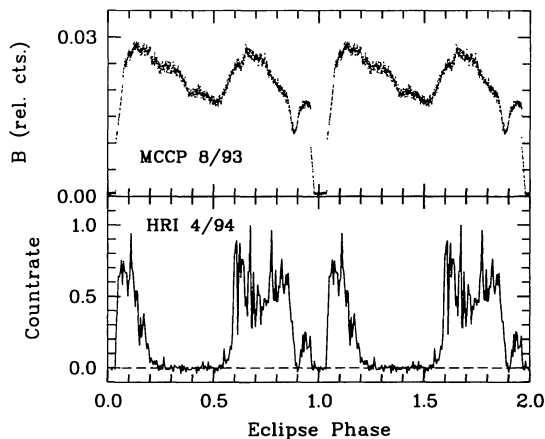
Figure 1.9:
Phase-folded light curves of the polar HU Aqr taken during high states of accretion. *Upper panel*: optical B band light (MCCP, Calar Alto). *Lower panel*: X-ray light curve (ROSAT HRI). From Schwope et al. (1995).

orbital phase intervals. For the description of phase intervals the terms *faint phase* and *bright phase* are commonly used. The use of both terms is self-explanatory but depends on the considered emission component. Usually but not necessarily the term faint phase denotes the orbital phase interval where the accretion region is self-eclipsed and the term bright phase the orbital phase where the accretion region is exposed to the observer. The beamed cyclotron component is brightest when the line of sight is perpendicular to the magnetic field lines. This roughly occurs when the accretion spot is on the limb of the white dwarf. The left panel shows from top to bottom a spectrum for high state - bright phase, low state - bright phase and low state - faint phase. The right panel shows a zoomed version of the two low state spectra together with a spectrum for a low-mass star of spectral-type M6. The low state spectrum at faint phase is mainly composed of the photospheres of both stellar components, i.e. the red dwarf and the white dwarf. At bright phase when the beamed cyclotron radiation is seen additional cyclotron harmonics are visible (numbers in the figure indicate harmonic numbers). When the system is much brighter in the high state, the white dwarf is outshone by the cyclotron component and additional contributions from the accretion stream.

The cooling plasma of the post-shock region and the re-processed soft component contribute to the X-ray regime. The post-shock region is thought to be optically thin for bremsstrahlung, thus the light curve of the hard X-ray component is top-hat shaped with the visibility of the post-shock region, but cosine profiles are also observed as in DP Leo (Pandel et al. 2002). Possible reasons include a special view of accretion geometry or Thomson scattering of the X-ray photons in an optically thick post-shock region (Cropper et al. 2000).
The emission from the accretion region irradiates the secondary and the accretion stream and excites additional line emission from both components, mainly He II, C IV, Si IV and N V in the UV and He I, He II, C III, N III and the Balmer lines in the optical and infra-red. Fig. 1.9 shows the X-ray light curve together with the B band light curve for the AM Her system HU Aqr. Both light curves are taken during high states but not contemporaneous. The dip at orbital phase 1.0 is the total eclipse of the white dwarf by the secondary
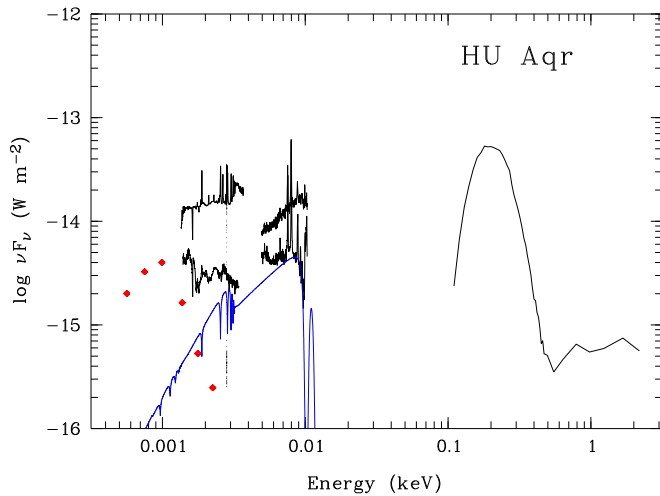
Figure 1.10:
Spectral energy distribution of the AM Her system HU Aquarii, showing optical, UV and X-ray observations (black). The ROSAT X-ray data from a high-state show the bremsstrahlung component together with the prominent soft X-ray component. The optical spectra are taken during high (upper spectrum) and low accretion state. The UV spectra are from the same observation during an intermediate accretion state for bright (upper spectrum) and faint phase (lower spectrum). From Schwope 2000.

at inferior conjunction due to the high inclination of the system. The dip preceding the eclipse dip is caused by the accretion stream or accretion curtain passing the line of sight towards the accretion region (compare with Fig. 1.4). Both dips are total in X-rays (unlike in the optical light curve), demonstrating that the X-ray emission originates solely at the accretion region on the white dwarf. Apart from the dips, the X-ray light curve shows a top-hat shape, with a bright phase when the accretion region is visible and faint phase, with the flux dropping to zero, when the accretion region is self-eclipsed by the white dwarf. The flickering during bright phase is commonly observed in polars and caused by inhomogeneous accretion. The optical light curve has different components. The depth of the pre-eclipse dip demonstrates the contribution of the accretion spot at the given phase interval. The accretion spot modulates the light curve with a cosine shape. Additional contribution and modulation comes from the accretion stream. Obvious is the much more extended optical bright phase due to the contributions from the accretion stream and the additional cyclotron component. The optical light curve nicely demonstrates the optical cyclotron component, when the accretion spot vanishes behind the limb of the white dwarf - compare optical and X-ray light curve at phase $\sim$0.2.

Finally, Fig. 1.10 shows the typical broad-band spectral energy distribution of a polar – again on the basis of HU Aqr. Red dots show the contribution of the late-type donor star, the blue model spectrum the contribution of the white dwarf. The observed optical and ultraviolet spectra (black) demonstrate the additional energy contribution of accretion stream and accretion region on the white dwarf for different states of accretion. The X-ray spectrum (above 0.1 keV) shows the prominent soft X-ray component of re-processed origin and the bremsstrahlung component from the cooling plasma.

1.6   Evolution of polars

Although during the last decades a "standard model" of CV evolution was established (Verbunt & Zwaan 1981, Rappaport et al. 1983), this *"disrupted magnetic braking model"* still suffers from sundry discrepancies between model and observations. This section provides an overview of the evolution of cataclysmic variables according to the standard model and shortly addresses the problems.

The progenitors of CVs are binaries with an orbital period of several years. The more massive component evolves faster and if it fills its Roche-lobe, matter is transfered onto the less massive component. Mass transfer from a more massive to a less massive component is unstable. The mass transfer rate increases until both components form a binary system with a common envelope. During the further evolution the binary distance decreases and the common envelope of the system is ejected. The binary now consists of the degenerated core of the more massive component – a white dwarf – and the remnant of the less massive component – a red dwarf with an orbital period of several days. The subsequent evolution is determined by the angular momentum loss (AML) of the system. The secondary star possesses a magnetic field powered by a shell dynamo mechanism. In combination with the stellar wind this leads to a loss of angular momentum, depending on the magnetic field strength and the wind loss rate of the secondary. Both define the Alfven radius where the ram pressure of the wind equals the magnetic pressure. Below the Alfven radius (called the magnetosphere of the star), the wind is frozen in the magnetic field, which increases the angular momentum of the outflowing wind. Above the Alfven radius the stellar wind can escape freely, removing mass and angular momentum from the secondary. Due to tidal forces the spin of the secondary is coupled to the orbit of the binary system, i.e. the angular momentum is removed from the binary orbit – leading to a decreasing binary distance (and at some point in the evolution to a spin-orbit synchronisation). This is called shortly *"magnetic braking"*.

Additional angular momentum loss happens due to gravitational radiation, but at this evolutionary stage the corresponding angular momentum loss rate is much smaller than the AML rate caused by the stellar wind.

If the orbital period is sufficiently short the secondary fills its Roche-lobe causing a continuous mass transfer onto the white dwarf. If the time-scale of the orbital period decrease gets shorter than the Kelvin-Helmholtz time-scale of the star, which increases with decreasing mass of the secondary, the secondary gets out of thermal equilibrium and thus overexpanded. Model calculations predict a mass transfer in the order of 10^{-9} $M_\odot$ yr^{-1} at periods between 3 and 8 hours, which is confirmed by observations.

At an orbital period of $\sim$3 hours – corresponding to a secondary mass between 0.2 and 0.3 $M_\odot$ – the secondary becomes fully convective. With the vanishing of the radiative core the stellar dynamo loses its anchor, the magnetic braking breaks down. The only remaining angular momentum loss mechanism is gravitational radiation. Since this AML happens on a time-scale much longer than the thermal time-scale of the star, the secondary can regain thermal equilibrium. It shrinks to its equilibrium radius, not filling its Roche-lobe
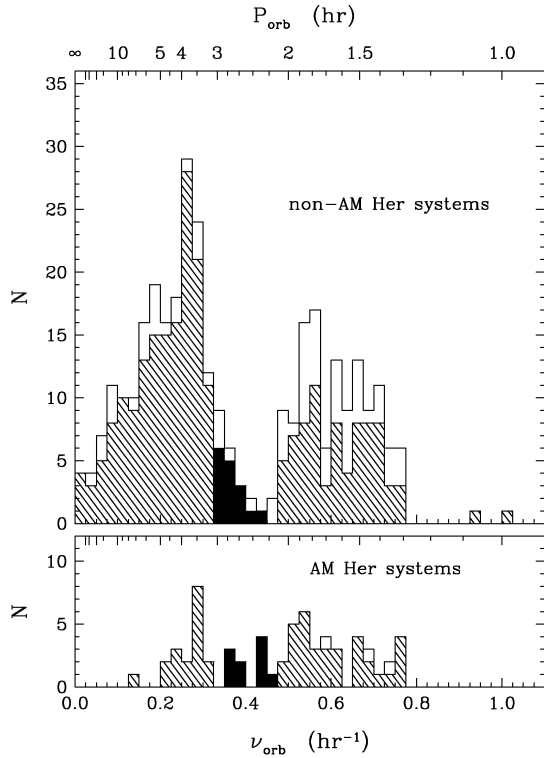
Figure 1.11:
Period distribution for AM Her and non-AM Her types of CVs. Shaded bins contain only systems with confirmed orbital period while unfilled bins include systems with uncertain orbital periods. Black bins highlight the systems within the period gap. From Webbink & Wickramasinghe (2002).

anymore. The mass transfer ceases, the brightness of the system drops dramatically – this is the reason of the above mentioned period gap. At an orbital period of $\sim$2 hours the secondary fills it – now smaller – Roche-lobe again, the mass transfer resumes – the system becomes bright enough to be observed. The only AML mechanism is still gravitational radiation, the secondary is in thermal equilibrium. The stable mass transfer rate is in the order of 10^{-10} $M_\odot$ yr^{-1}. With ongoing period decrease the mass transfer time-scale and the thermal time-scale of the secondary increase, the former with -M/$\dot{M}$, the latter with $1/M^2$. At an orbital period of 1.2 hours, the mass of the secondary is now below 0.1 $M_\odot$, the thermal time-scale exceeds the mass transfer time-scale again. The star expands adiabatically, the orbital period increases – up to 2 hours within the Hubble time. Mass transfer is still going on, the core of the secondary becomes gradually degenerated (Howell et al. 1997).

The standard model predicts the same evolution for magnetic and non-magnetic cataclysmic variables, a period gap between $\sim$2 and $\sim$3 hours for all types of CVs and an orbital period minimum of 1.2 hours. Despite being quite successful the comparison with observations reveals fundamental problems of the standard model. Fig. 1.11 shows the period distribution for magnetic and non-magnetic CVs. Four facts are obvious: the observed period minimum is at 1.3 h, much more non-magnetic systems above the period gap than below it are observed (contrary to the magnetic CVs), the period gap itself is populated from longer orbital periods for the non-magnetic systems while for the AM Her systems the period gap seems to be absent. Indeed there are statistical studies claiming that the period gap for nova-like CVs is non-significant (Verbunt 1997, Hellier & Naylor

1998), while others claim the contrary (Wheatley 1995).

The much less pronounced period gap for the AM Her systems can be explained with the magnetic field of the white dwarf (Wickramasinghe & Wu 1994) which interacts with the magnetic field of the secondary, reducing the number of open field lines on the secondary and thus reducing the magnetic braking (Li et al. 1994b, Li et al. 1994a, Li et al. 1995, Li & Wickramasinghe 1998). The resulting AML rate drops, the mass transfer rate decreases. The secondary is less overexpanded, the resulting decrease in radius at the onset of the period gap when the star regains thermal equilibrium is reduced. The period gap fills from the lower end and becomes less and less pronounced for increasing field strength of the white dwarf, i.e. decreased magnetic braking. This idea is supported by the measured white dwarf temperatures. While the mean temperature for the non-magnetic white dwarfs in CVs is $T_{eff} \sim 24100$ K, the mean temperature for the magnetic ones is with $T_{eff} \sim 16400$ K much lower (Sion 1999). This relation holds true for any given orbital period, but is significantly greater for white dwarfs above the period gap (Araujo-Betancor et al. 2005). Interpreted in terms of cooling time the reduced magnetic braking increases the evolutionary time-scale and decreases the long-term accretion rate, the white dwarf is less compressional heated and has more time to cool, hence it has a lower temperature than a non-magnetic white dwarf. Although this seems plausible, the lower temperature of the magnetic white dwarf can also be explained with a lower mass compared with the non-magnetic white dwarfs, but the number of magnetic systems with known white dwarf masses is still too low for any conclusion (see Fig. 1.6). At least for single white dwarfs the opposite is true.

The populated upper end of the period gap for the non-magnetic CVs can be explained with metal-deficient donor stars (Webbink & Wickramasinghe 2002), the lack of AM Her systems above the gap – compared to the non-magnetic CVs – with the white dwarf spin - orbit synchronisation which must be established before the system can be observed as an AM Her system. The most pestering problem concerns the period minimum. It should not only be observed at 1.1 h, but also – due to the long evolutionary time-scale – the majority of systems should cluster at the period minimum. Model calculations (Kolb & de Kool 1993, Howell et al. 1997, Kolb & Baraffe 1999) predict that nearly all CVs should be observed below the period gap, with two-thirds already having bounced at the period minimum. This is in considerable disagreement with the observations. The observed mismatch could be based on several facts. If the observed period minimum of 1.3 h reflects reality, a fourfolded angular momentum loss compared to the angular momentum loss due to gravitational radiation is required (Kolb & Baraffe 1999) to pull up the period minimum (this also implies a shorter evolutionary time-scale, attenuating the required peak of systems at the lowest orbital frequencies). This requires an additional braking mechanism. Although several observational studies (Jones et al. 1996, Andronov et al. 2003) and model calculations (Sills et al. 2000) of low-mass stars suggest that there is no cut-off of the stellar magnetic field when the star becomes fully convective (the shell dynamo mechanism for the stellar field is substituted by a distributed or turbulent dynamo mechanism (Durney et al. 1993, Durney & Latour 1978) for the fully convective star) and thus permit the possibility of magnetic braking even below the gap, this raises other problems. The cut-off of

magnetic braking is the common explanation for the period gap, without the disrupted magnetic braking another explanation for it is required. An intrinsic change of the mass-radius relation of the secondary (Clemens et al. 1998) could also explain the period gap, but would induce features in the orbital distribution that are not observed (Kolb et al. 1998). Also an ongoing magnetic braking would be effectively suppressed by the magnetic field of the white dwarf at the low orbital distances below the gap for the case of AM Her systems. Furthermore the white dwarf temperatures below the period gap are consistent with mass transfer rates corresponding to AML rates due to gravitational radiation alone (Araujo-Betancor et al. 2005).

Other explanations (Andronov et al. 2003) involve different populations below and above the period gap. The implied long evolutionary time-scale and hence low AML rates above the period gap are comparable with empirical AML rates obtained from open cluster stars, but lower than the observed ones in cataclysmic variables. Other authors claim that even the oldest CVs have not yet reached the minimum period – which could be enabled by a much more efficient common envelope phase delivering progenitors of CVs with a much wider orbit (King & Schenker 2002), insufficient model calculations or that the systems at the lowest orbital periods are – for whatever reasons – too faint to be observed (Kolb & Baraffe 1999).

1.7   Preview

The following chapters present a detailed analysis of three different magnetic cataclysmic variables covering the range from optical to X-ray wavelengths and disentangling the spectral energy distributions of the different emission components. Chapter 2 deals with WX LMi, a system belonging to a class termed *low accretion rate polars* in the past, according to their observed very low accretion rates. We could unearth new evidence, that this system (as well as the other low accretion rate polars) is more likely a progenitor of normal polars, with a cool white dwarf that has never undergone the usual compressional heating and is probably accreting at very low rates from the wind of the secondary. Our data analysis provided the first opportunity to distinguish between X-ray emission from the accretion plasma and the corona of the secondary. We could further find new evidence for the *"bombardment solution"* (see above) at low accretion rates. Chapter 3 presents the serendipitously discovered short-period eclipsing polar 2XMMpJ131223.4+173659, which was analysed in optical, UV and X-ray wavelength. This system belongs to only a few systems, which show no soft component in their X-ray spectra despite being in a high accretion state. We discuss the likely accretion scenario, the system parameters and the spectral energy distribution. Chapter 4 introduces a program to map the temperature distribution of a white dwarf surface, using optical and UV low state data with high time resolution. Chapter 5 shows the well-known polar HU Aquarii. Using optical high time resolution observations, we could redetermine the system parameters with high accuracy, which could be used to determine a significant orbital period decrease. The likely reasons

for this period decrease and the implications for the evolution of CVs are discussed.

Chapter 2

The pre-polar WX Leonis Minoris

2.1 Introduction

Another problem with the evolution of cataclysmic variables not mentioned in the intro-
duction is the striking lack of observable progenitors of CVs, before the onset of mass
transfer. Recently a few systems with very low accretion rates (a factor $100 - 1000$ below
the canonical values for Roche-lobe overflow) were uncovered in optical spectroscopic sur-
veys (HQS: Hagen et al. 1995; SDSS: York et al. 2000). They were identified on the basis
of highly peculiar optical spectra with broad cyclotron harmonics in emission mimicing
quasar emission lines. They could form an important part of the population of close inter-
acting binaries, whether as normal CVs in extended low states or pre-CVs on their track
towards Roche-lobe overflow. Recently, as pushed forward by the work by Schmidt et al.
(2005), evidence grows that these systems are pre-CVs. They are not only important ob-
jects concerning the evolution of polars, but also the best suited objects for studying the
accretion scenario in the case of very low specific accretion rates $\dot{m}$ and at a high magnetic
field as well as the possible X-ray activity of the donor star.

WX LMi (HS 1023+3900) is one of these low accretion rate polars and was discovered
by Reimers et al. (1999) from the Hamburg Quasar Survey. From optical and spectroscopic
follow-up observations, they determined a period of about 167 minutes and two accretion
spots with a field strength of 60 MG and 68 MG, respectively. The accretion rate was found
to be $\dot{M} < 3 \times 10^{-13}$ M$_\odot$/yr, i.e. orders of magnitudes below the normally observed accretion
rate in polars. A spectral type of dM4.5 gave a good spectral fit for the secondary and was
used to deduce a distance of 140 ± 50 pc. Schwarz et al. (2001) used optical photometry,
performed with the Potsdam 70 cm telescope in *UBVRI*, to determine a stable long-term
ephemeris based on the timings of optical maxima from the primary accretion spot. During
the whole monitoring campaign covering half a year, the system was in a similar low state
of accretion with the one exception of a flare that was located on the active secondary.
From the colours at the orbital phase when both accretion spots are invisible, the spectral

Figure 2.1: Finding chart for WX LMi (position RA, Dec (2000) = 10h26m27.40s,+38d45$'$05$\overset{s}{.}$0) and the used comparison for the optical photometry.
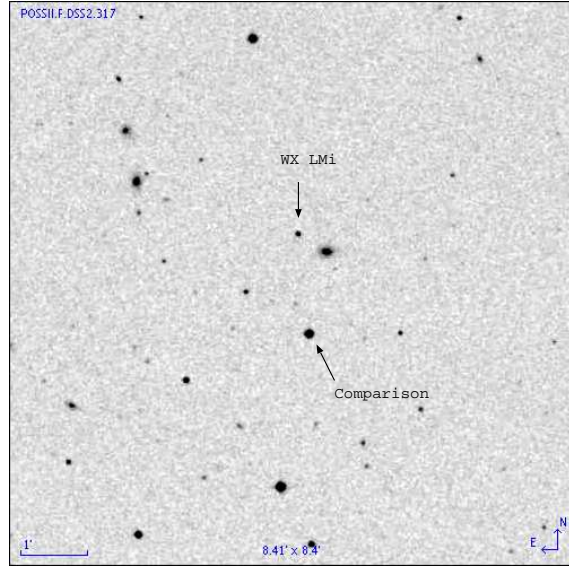
type of the secondary was likewise determined as M4.5. Using the relative magnitude in the I band at photometric minimum yields a distance of ~ 100 pc.

WX LMi as well as the similar objects termed LARPs (low accretion-rate polars, Schwope et al. 2002b), was not discovered in the ROSAT All Sky Survey[1] despite its relatively short distance. WX LMi was in the off-axis field of two X-ray ROSAT PSPC pointings (10 and 13 ksec) and discovered at a rate of 0.004 cts/sec. The very low number of photons did not allow extraction of a proper X-ray spectrum and determination of the origin of the X-rays, whether accretion-induced or from the active corona of the secondary. We thus performed new X-ray observations with XMM-Newton[2]. The X-ray observations of WX LMi were accompanied by near-ultraviolet observations with the OM onboard XMM-Newton. It was used as a bolometer in order to determine the white dwarf photospheric temperature. This should help to decide whether the LARPs are normal polars in an occasional state of very low accretion or pre-cataclysmic binaries that never have been accreting. Our newer X-ray and UV observations are analysed together with phase-resolved optical spectroscopic observations already performed back in 1999. Since the overall brightness of WX LMi does not change, the two data sets can be combined without difficulty and thus allowing a broader picture of the relevant spectral components.

Since the number of LARPS/pre-CVs is still very small the available data for all seven systems beside WX LMi were reassembled from the literature or analyzed for the first time for comparison. All eight systems known today are summarized in Table 2.5.

---

[1]see A.1

[2]see A.2

Date (Y/M/D)	Instrument	Wavelength range/Filter [Å]	Resolution [Å]	No. of spectra/images
1999/3/09	TWIN	3800-9900	6/4[a]	47[b]
1999/3/10	TWIN	3800-9900	6/4[a]	56[b]
1999/3/18	MOSCA	3380-8410	13	29[b]
2004/4/28	AIP	V		71[c]
2005/3/21	AIP	V		171[d]

[a] for the blue/red channel
[b] integration time 300 seconds each
[c] integration time 120 seconds each
[d] integration time 60 seconds each

Table 2.1: Log of spectroscopic observations with the Calar Alto 3.5m telescope and photometric observations with the Potsdam 70cm reflector.

2.2 New optical and X-ray observations

2.2.1 Optical photometry and spectroscopy

WX LMi was observed with the Calar Alto 3.5m telescope on two occasions in March 1999. The double-beam spectrograph TWIN was used for the first run in March 9–11, the multi-object spectrograph MOSCA for the second run on March 18/19. Low-resolution gratings with reciprocal dispersions of $144\,\text{Å/mm}$ and $108\,\text{Å/mm}$ were used for the TWIN observations resulting in a spectral coverage of 3800–$6900\,\text{Å}$ and 6700–$9900\,\text{Å}$ in the blue and red channels at a spectral resolution of about 6 and $4\,\text{Å}$, respectively. A series of 47 spectra with exposure time of 5 minutes each were obtained on the night March 9/10 (BJD 2451247.484406 – 2451247.671117), another series of 56 spectra with the same exposure time on the following night (BJD 2451248.375258 – 2451248.596263). All binary phases were thus covered by spectroscopic observations. Spectrophotometric standards were observed during the same nights and used for calibration of the spectral response. The He/Ar arc lamp spectra were taken for calibrating the dispersion.

Contemporary to the X-ray observations in 2004, WX LMi was observed in V band with an exposure time of 120 sec for nearly one orbit on April 28 with the Potsdam 70cm reflector (BJD 2453124.480741 – 2453124.480731). To improve the ephemeris we had to extend the baseline of observations, thus further observations were performed on March 21, 2005 (BJD 2453451.391887 – 2453451.526543), covering more than one orbit. A finding chart for WX LMi is provided in Fig. 2.1. All new optical observations are summarized in Table 2.1. Figure 2.2 shows the mean orbital spectrum of WX LMi obtained with the TWIN

Figure 2.2: Mean orbital spectrum of WX LMi obtained March/April, 1999, with the TWIN and MOSCA spectrographs at the Calar Alto 3.5m telescope. The Ca H+K, the Balmer emission lines, and Na absorption lines are indicated by vertical ticks.
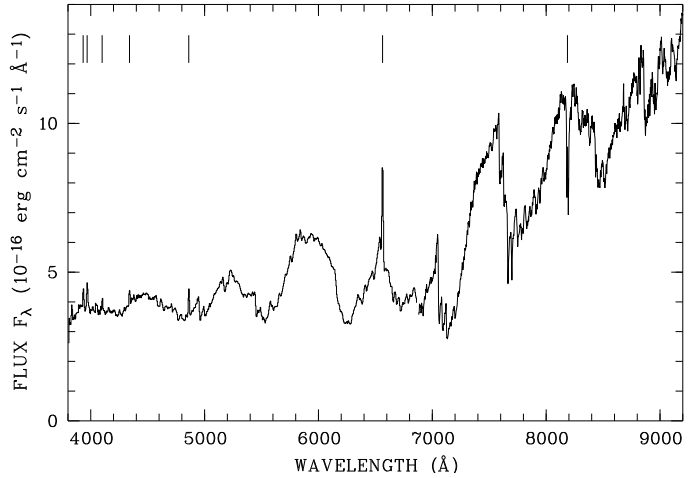
(longward 6800 Å) and MOSCA spectrographs. It shows the same features as described by Reimers et al. (1999); i.e. an M dwarf dominating the red spectral range, a white dwarf that is responsible for the spectral upturn in the blue range and several pronounced cyclotron lines, the most prominent one at 5950 Å. The higher spectral resolution and the partly better signal provided by the observations presented here allows individual spectral features to be resolved and studied. The most prominent ones are the H-Balmer emission lines and the NaI absorption lines at 8183/94 Å.

2.2.2 XMM-Newton X-ray and ultraviolet observations

We performed ultraviolet and X-ray observations of WX LMi with XMM-Newton in April 2004 for about 30 ksec, covering 3 orbital cycles. Calibrated photon event tables for all detectors were computed with SAS version 6.5[3]. Since the spectrum turned out to be very soft, the SAS task `epreject` was used to extend the usable energy range down to 0.12 keV. The barycentric correction was applied using `barycen`. The spectra were extracted from the event tables with SAS tasks `evselect` and `especget`. The light curve was obtained running the `edetect_chain` pipeline on time-selected event tables containing all events that occurred in a given orbital phase interval.

The EPIC PN was operated in full-frame imaging mode, yielding ~ 800 counts from the source. Both EPIC MOS cameras were operated in partial window mode, yielding both ~ 200 counts. The observing time with the OM was spent in nearly equal shares with the U and UVW1 filters centered on 3440 Å and 2910 Å, respectively. The detector was used in fast mode for the full observation. The mean countrates in the U and UVW1 filters were $2.12\,\mathrm{s}^{-1}$ and $0.75\,\mathrm{s}^{-1}$, respectively. All XMM observations are summarized in Table 2.2.

---

[3]http://xmm.vilspa.esa.es/external/xmm_sw_cal/sas.shtml

Date (Y/M/D)	Instrument	Filter/Mode	Total Duration [ksec]
2004/04/24	XMM-PN	Thin/Full	29.0
	XMM-MOS1	Thin/Partial	30.6
	XMM-MOS2	Thin/Partial	30.6
	XMM OM	U/Fast	12.2
	XMM OM	UVW1/Fast	16.3

Table 2.2: Log of XMM-Newton observations for WX LMi

2.3 Updated ephemeris

Schwarz et al. (2001) fixed the ephemeris of the system using photometric data covering a period of six months. The primary maxima of the V band data pinned down the epoch of zero phase, and the variability in the light curves in VRI was used to establish the period. We performed additional photometric observation with the Potsdam 70cm telescope in V band on April 28, 2004 and March 21, 2005. These observations revealed the system to be at the same brightness as during our monitoring observations in 1999 and also showed the same variability pattern. A linear regression to all observed primary V band maxima between 1999 and 2005 yielded a period of 0.11592364(43) days. Our spectroscopic observations from March 1999 determined the inferior conjunction of the secondary. The epoch of the blue-to-red zero crossing of the NaI-lines was used as the spectroscopic zero point. This yields the updated ephemeris

$$\text{BJD} = 2451247.50425(27) + E \times 0.11592364(43) \tag{2.1}$$

where the number in brackets represent the uncertainty. The difference between spectroscopic and photometric phase zero is 0.168 phase units. The phase used in the further sections refers to this spectroscopic ephemeris.

Figure 2.3 shows the phase-folded light curves for the XMM-PN observation and the XMM-OM observations in both filters as well as the cyclotron component (see Section 2.5).

2.4 The active secondary

In order to determine the spectral type of the secondary, we made use of the TWIN spectra obtained in the red channel. The spectral type was not determined straightforwardly due to the wavelength- and phase-dependent background component from the white dwarf (photospheric and beamed cyclotron radiation from two accretion spots). Firstly an average spectrum was created using only these – radial velocity corrected – spectra, that were not

Figure 2.3: Phase folded light curves obtained with EPIC-PN for the energy range 0.12 - 2.5 keV and the OM U and UVW1 filter. The top panel shows for comparison (see Fig. 2.7) the total cyclotron flux from the 3rd and 4th cyclotron harmonics from the primary and the 2nd and 3rd harmonics from the secondary accretion spot in units of 10^{-16} erg cm^{-2} s^{-1}.
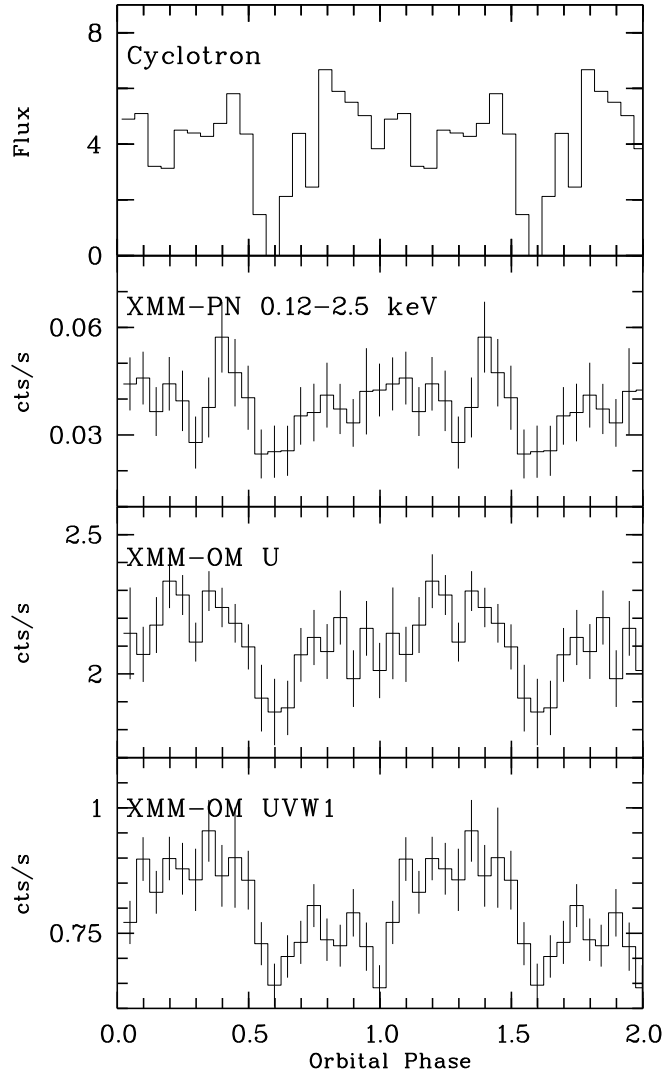
too heavily affected by the poor weather conditions during the observations. Secondly a non-magnetic white dwarf model atmosphere was scaled to the average spectrum using wavelength regions free of any cyclotron emission and subtracted from all selected spectra composing the average spectrum. This left us with phase-dependent spectra containing only the secondary and the cyclotron lines.

In order to constrain the spectral type of the secondary, we decided to use the narrow-band spectral indices TiO5 and VO-a (Cruz & Reid 2002, Kirkpatrick et al. 1999). These indices correlate best with the spectral type according to those papers and are shown for comparison in Fig. 2.4 (right panel). We also tried the pseudocontinuum spectral ratio between the wavelength ranges 8235 – 8265 Å and 7540 – 7580 Å, the so-called PC3 index (Martín et al. 1999)), although we did consider the results less reliable since the two continuum side bands have a relatively large separation, and the index is therefore much more
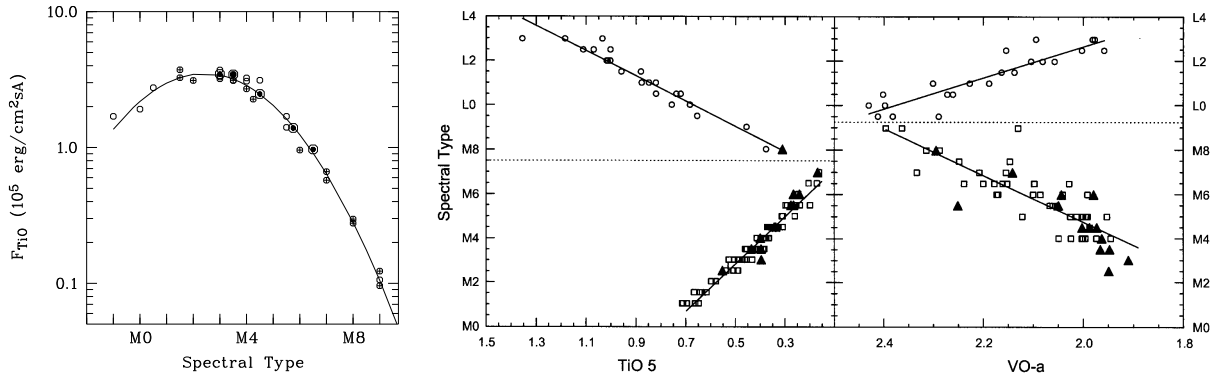
Figure 2.4: *Left*: Absolute TiO flux depression expressed as surface brightness (multiplied by (distance/radius)^2) as a function of spectral type. From Beuermann (2000). *Right*: Spectral type as a function of the spectral indices TiO5 and VO-a. Both indices are double-valued with TiO5 reversing in strength at M7 and VO-a at M9. From Cruz & Reid (2002).

sensitive to variations in the underlying cyclotron radiation. The indices were determined for all spectra, and finally averaged – without those indices where the spectral features were found to be superposed with a cyclotron line. The TiO5 index thus determined was 0.30±0.05, the VO-a index 1.99±0.03, and the PC3 index 1.21±0.05. The given errors reflect the statistical uncertainty and the uncertainty that results from the subtraction of the white-dwarf model spectrum. The measured indices resulted in spectral types of M5.0±0.5, M4.5±0.7, and M4.5±1. We finally adopted a spectral type of M4.5 with an uncertainty of half a subclass. This new determination of the spectral type based on spectral data with sufficient resolution is in good agreement with the estimates of Reimers et al. (1999) and Schwarz et al. (2001) based on spectroscopy with much lower resolution and broad-band optical photometry, respectively.

Beuermann et al. (1998) have shown that the colour $I - K$ can be used as tracer of the spectral type. A parameterization of the Sp-($I - K$) relation was given as a third-order polynomial. Due to the high field strength of > 60 MG in WX LMi the cyclotron fundamental is at < 1.8 μm, thus the K-Band (centered at 2.2 μm) is likely to be uncontaminated by cyclotron radiation, allowing a spectral type of M4 to be determined for $I = 14.83$ (Schwarz et al. 2001) and $K = 12.49$ (2MASS database) in accordance with the above value. As explained in Sect.1.4 the secondary in normal polars has a later spectral type than expected for Roche-lobe filling ZAMS stars. The usual justification for that fact is the lack of thermal equilibrium due to mass loss. We argue below that this explanation probably does not apply here, suggesting the presence of a Roche-lobe underfilling main-sequence secondary in WX LMi.

As already mentioned in Chapter 1, the composite nature of the emission from cataclysmic variables, particularly in the optical, makes it difficult to perform a straightforward distance measurement. We did not make use of Roche-lobe geometry, since the secondary is possibly somewhat underfilling. The simple use of the distance modulus also does not

Sp	$\log(R/R_\odot)^a$	$M/M_\odot^b$	M_K^c	S_K^d	F_{TiO}^e	$d(S_K)$	$d^f(\mathrm{TiO})$
4	-0.613	0.220	7.53	4.37	3.08	103	130
4.5	-0.676	0.179	7.95	4.46	2.62	85	104
5	-0.740	0.147	8.37	4.56	2.15	70	82

[a] according to Beuermann et al. (1999)
[b] according to Delfosse et al. (2000)
[c] according to Delfosse et al. (2000)
[d] according to Beuermann et al. (1999)
[e] according to Beuermann et al. (1999) in units of $10^5\,\mathrm{erg\,cm^{-1}\,s^{-1}\,\AA^{-1}}$
[f] using an observed flux deficit $F_{7165} = 5.5 \times 10^{-16}\,\mathrm{erg\,cm^{-1}\,s^{-1}\,\AA^{-1}}$ (uncertainty of 30%)

Table 2.3: Parameters for the secondary in WX LMi

seem to be appropriate, since the secondary is clearly deformed as shown by ellipsoidal modulations in the continuum of the TWIN spectra. We assumed that the secondary in WX LMi is a ZAMS star with solar metallicity, which is well justified (Beuermann et al. 1998), and then make use of the surface brightness - spectral type and F_{TiO} - spectral type relations compiled by Beuermann & Weichhold (1999). We used radii from the compilations of Beuermann et al. (1999). Absolute magnitudes and masses for the possible spectral types are derived from Delfosse et al. (2000). The results are summarized in Table 2.3. Fig.2.4 (left panel) shows the F_{TiO} - spectral type relation from Beuermann (2000). The measured flux deficit in the TiO feature was corrected for the contribution of the white dwarf at this wavelength. For the most likely spectral type, M4.5, our distance estimates give 85 and 100 pc, with a relatively large spread of about 20 pc. If the secondary behaved like most of the CV secondaries at the given P_{orb}, the radius would be larger than given in Table 2.3 and the distance would increase. We thus use a distance of 100 pc to WX LMi in the following.

Another aspect of the secondary concerns its magnetic activity. In sun-like stars, the magnetic field at the surface is powered by a "shell dynamo", anchored at the boundary between the convective outer shell and the inner radiative core. The magnetic field strength depends on the differential rotation and is correlated with the rotation rate of the star. For M dwarfs the picture is different. The shell dynamo mechanism does not work for dwarfs later than $\sim$M3, when the star becomes fully convective and must be replaced with a turbulent dynamo model. Also the strong rotation rate - magnetic field strength correlation does not hold for all M dwarfs - the magnetic activity is constant for a wide range of rotation rates (see below). The fraction of active M stars is correlated with the spectral type and increases with spectral type, with nearly all stars being magnetically active at spectral type M7 and decreases afterwards (Hawley et al. 2000). A feature commonly used as an activity indicator in M dwarfs is the Hα emission. Contrary to sun-like stars the surface coverage of the magnetic field is large (more than half of the surface) and the field at the surface is much stronger. The consequence is an extensive magnetic heating of the outer atmosphere, leading to strong Ca II, Mg II and Balmer line emission from

the chromosphere and soft X-ray emission from the corona. Despite the lack of sufficient spectral resolution, the Hα lines of WX LMi seem to consist of just one line. Contrary to polars in their high accretion states, which show further emission line components in Hα that could be attributed to an accretion stream or disk. Also the tight orbital phase relation between the Hα and the NaI lines suggests a common origin on the secondary star. The Hα emission line is thus assigned completely to the photospheric activity of the secondary star. To determine the flux of the Hα emission line, the spectra were corrected for radial velocity and the scaled spectrum of the single, non-active M4.5 star Gl 268 was subtracted. To determmie the equivalent width of the line, the line flux was related to the continuum of the scaled Gliese star at this wavelength.

Walkowicz et al. (2004) investigated the strength of activity via Hα measurements for a large number of SDSS stars. They parametrise the strength with an χ factor, $\chi \times EW_{H_\alpha} = L_{H_\alpha}/L_{bol}$. For spectral types M4 – M4.5, the factor is $\log \chi = -4.2 \ldots -4.4$, and $\log(L_{H_\alpha}/L_{bol})$ becomes $-3.7 \ldots -3.2$ for the TWIN observations.

Recently, West et al. (2004) and Silvestri et al. (2005) studied a large number of either single (West et al. 2004) or common proper motion WD/MS binaries (CPMBs, Silvestri et al. 2005) drawn from the SDSS. The large majority (90%) of the Silvestri et al. (2005) CPMBs has an EW close to 0 (their Fig. 2). The mean Hα luminosity of the West et al. sample at spectral type M4–M5 is $-3.57 \ldots -3.67$ (their Fig. 4 and Table 1). These figures clearly put the secondary in WX LMi among the more active stars in its category. The comparison between our MOSCA and TWIN observations showed that the Hα activity is remarkably variable on a timescale of a month or shorter.

The EPIC-PN light curve (see Fig.2.7) shows orbital phase-dependent modulation with a pronounced minimum at the time when both accretion spots are hidden from the observer's view. While the cyclotron flux drops to zero around $\phi \sim 0.6$, the X-ray flux remains at the constant minimum flux. We ascribe the residual flux around that phase to the corona of the secondary star.

The average count rate of WX LMi is too low to make a phase-dependent spectral analysis feasible. Figure 2.5 shows the orbital mean spectra obtained with EPIC-PN and EPIC-MOS. Essentially all the X-ray flux emerges below 2 keV. We fitted the combined PN and MOS spectra with XSPEC. Our results are summarised in Table 2.4. A first approach with a single MEKAL[4] model for a coronal and/or accretion plasma, molding emission from the secondary and from the accretion region with one temperature, led to no satisfying fit. Motivated by the presence of a soft blackbody-like and a hard thermal component in high accretion rate polars, our next attempt included a black-body component. The fit was improved, but the temperature of 117 ± 11 eV for the black body was higher than in any other polar observed until then and thus seemed implausible. A satisfactory fit was achieved using a two component MEKAL model. The temperatures of 0.26 ± 0.02 keV and 0.82 ± 0.05 keV are well within the regime that one expects for a coronal plasma. The tem-

---

[4]a model describing the emission of a hot optically thin plasma, named after its authors Mewe, Kaastra and Liedahl

Figure 2.5: Spectral fit of the combined PN and MOS spectra with a two-component MEKAL model (see Table 2.4 for spectral parameters)
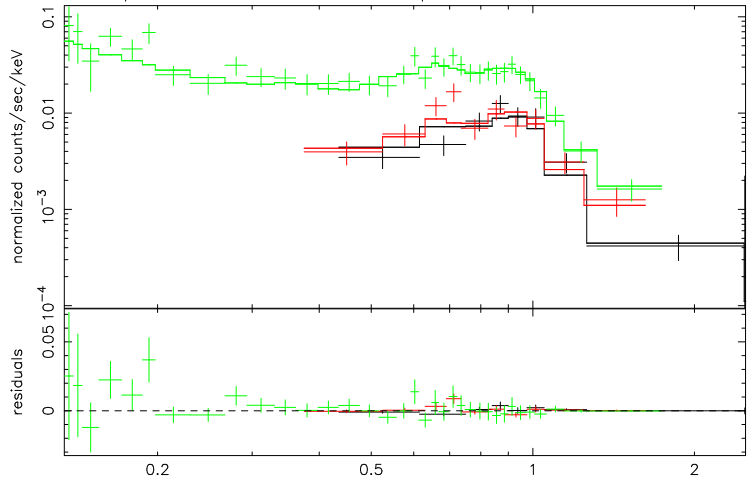
Model	χ^2_ν	NHP[a]	kT (MEKAL) [keV]	kT (BB) [eV]	n_H^b [cm^{-2}]	Flux[c] [ergs cm^{-2} s^{-1}]
wabs (MEKAL)	3.44	1.3e-15	0.62±0.02		5.6e-6	4.2E-14
wabs (BB+MEKAL)	1.42	2.6e-2	0.66±0.02	117 ± 11	1.0^d	4.6E-14
wabs (MEKAL+MEKAL)	0.98	0.51	0.26±0.02 0.82±0.05		1.2e-12	5.4E-14

[a] null hypothesis probability, [b] in units of 1e20, [c] integrated flux 0.1-5 keV, [d] frozen

Table 2.4: Spectral fits for the combined PN and MOS spectra

perature thus determined would be very low for the accretion plasma of a normal-accreting polar. It is, however, in the same range as the temperatures derived from the analysis of the cyclotron emitting plasma.

To make a possible distinction between the two components (accretion plasma and corona), we extracted spectra according to the time intervals when only one of the two spots was directed towards the observer. The spectral fits of those two separated spectra yielded no significant differences between them and compared to the overall mean spectrum. Also, we could not detect any significant variation in the X-ray hardness ratio as a function of orbital phase. Hence, we cannot discern between the coronal and the accretion plasma on the basis of possible spectral differences with the given number of photons.

The unabsorbed flux (0.1 - 5 keV) for the two-component MEKAL fit is 5.4×10^{-14} erg cm^{-2} s^{-1}. For a distance of 100 pc, this yields an X-ray luminosity of 6.4×10^{28} erg s^{-1}. Based on the variability in the X-ray light curves, we assume that the secondary and the accretion regions contribute roughly equal X-ray flux and luminosity to the observed X-ray spectrum; i.e. we get $L_{M_2,X} \sim (L_{1,X} + L_{2,X}) \sim 3.2 \times 10^{28}$ erg s^{-1}.

Our estimate of the X-ray luminosity of the secondary star makes a comparison with

the X-ray activity of normal late-type dwarfs possible. The latter is correlated with the stellar rotation (Pallavicini et al. 1981; Pizzolato et al. 2003). It increases with decreasing rotation rate but enters – depending from the current mass – a saturated regime for rotation rates below several days (Pizzolato et al. 2003). According to Leggett et al. (1996), the bolometric luminosity of our assumed M4.5 secondary is $L_{\mathrm{bol}} = 3.9 \times 10^{31}$ erg s^{-1}. The X-ray flux attributed to the secondary, $L_{\mathrm{M_2,X}} \sim 3.2 \times 10^{28}\,\mathrm{erg\,s^{-1}}$, results in $L_{\mathrm{X}}/L_{\mathrm{bol}} \simeq 0.8 \times 10^{-3}$. This result is only weakly dependent on the assumed spectral type; i.e. for an M3 secondary we get 0.3×10^{-3}.

For the latest spectral types the saturated regime in Pizzolato et al. (2003) rests on a rather small number of stars. The X-ray luminosity determined for the secondary of WX LMi falls well on the constant branch of their diagrams, suggesting saturation of the activity.

The same comparison can be made for the other low accretion-rate polars as well. Table 2.5 compiles the parameters from the literature. SDSS1031 and SDSS1059 are not (yet) observed in X-rays. An analysis of the XMM-Newton data for SDSS0837 was never published, but the data went public in August 2006. We reduced the XMM archive data according to the SAS manual. The SAS task *epreject* was used to extend the usable energy range down to 150 keV, but no source could be detected. To get an upper limit the source region at the appropriate coordinates was extracted and background subtracted. We were left with just 14 photons. To this crude "spectrum" we applied an absorbed single-temperature MEKAL model, using XSPEC. The hydrogen column was fixed to the galactic nH at the source coordinates, the plasma temperature was stepped from 0.1-1.0 keV, giving a best fit for a plasma temperature of 0.20(9)keV. This corresponds to an unabsorbed flux of 7.7×10^{-15} ergs cm^{-2} s^{-1} in the energy range 0.15-5 keV and a X-ray luminosity of $L_{\mathrm{X}} \leq 1.0 \times 10^{29}\,\mathrm{erg\,s^{-1}}$. Also for SDSS1324 only an upper limit was obtained from XMM observation (Szkody et al. 2004) and for HS0922 there is an upper limit from a ROSAT PSPC observation (Reimers & Hagen 2000). SDSS2048 could be identified with a RASS source, but there are other optical objects within the error circle (Schmidt et al. 2005), which makes the identification as an X-ray source ambiguous. If we take the upper limit at face value, it falls on the relation by Pizzolato. SDSS1031 and SDSS1059 (Schmidt et al. 2007) are not (yet) observed with XMM. Besides WX LMi only SDSS1553 has a clear X-ray detection, and the source was found clearly above the Pizzolato et al. relation. However, the luminosity variations for the late spectral types in the compilation of Leggett et al. (1996) are large. Taking the uncertainty for the spectral type of the secondary into account, SDSS1553 could satisfy the Pizzolato et al. relation as well. Otherwise this could indicate additional X-ray emission from the accretion plasma, although the PN light curve shows no variability, in contrast to the optical light curve (Szkody et al. 2004).

Hence, one (WX LMi) of the two objects with a proper X-ray detection seems to behave like a normal main-sequence star, as far as X-ray activity is concerned, and lends support to the picture of saturated activity, while the other leads to no definite conclusion, considering the uncertainty in L_{bol}.

WX LMi is the first polar which gave the opportunity to distinguish between emission

from the accretion plasma and the corona, which is normally outshone by the accretion process. But due to the – in this respect – disadvantageous accretion geometry (see next section), the distinction of both sources is not unimpeachable, since the two accretion spots rotate alternately into view and the section of orbital phase where both accretion spots are self-eclipsed is very short. The otherwise very similar system HS0922+1333 exhibits an auspicious accretion geometry with only one accretion pole and is due to its short distance – contrary to SDSS1031 and SDSS1059 – likely to provide significant X-ray emission. We therefore successfully proposed a XMM-Newton observation of HS0922+1333 in AO-7. This observation will hopefully provide more data to the extremely sparse information about the coronal activity of polar secondaries.

Object[d]	Period [h]	Spectral type	Comparison[b]	distance [pc]	L_{bol}	L_X [erg/s]	L_X/L_{bol} [10^{-3}]	T_{WD} [10^3 K]
WX LMi	2.78	M4.5	Gl268	100	3.86e31	3.2e28[a]	0.8	< 8
HS0922 [1,3]	4.07	M3.5	Gl494	190	1.97e32	< 7.5e29	< 3.8	< 10
SDSSJ0837 [3]	3.18	M5	LHS377	330	3.43e30	< 1.0e29	< 30	< 14
SDSSJ1031 [4]	1.37	≥ M6	-	270-430	-	-[c]	-	9.5±1.5
SDSSJ1059 [4]	>3	M3-M5	-	460-1300	-	-[c]	-	< 8.5
SDSSJ1324 [1,2,3]	2.6	M6	GJ1111	450	3.18e30	< 1.4e29	< 46	< 6
SDSSJ1553 [1,2,3]	4.39	M5	LHS377	130	3.43e30	1.4e29	41	∼ 5.5
SDSSJ2048 [3]	4.2	M3	Gl388	260	8.93e31	< 7.9e29	< 0.9	< 7.5

[a] taken one half of the unabsorbed MEKAL+MEKAL flux in the range 0.1 - 5 keV
[b] for the secondary star, see Leggett et al. (1996)
[c] not (yet) observed in X-rays
[d] for full identifier see references

References:
[1] Webbink & Wickramasinghe (2005)
[2] Szkody et al. (2004)
[3] Schmidt et al. (2005) and references therein
[4] Schmidt et al. (2007)

Table 2.5: Summary of system parameters for all known pre-polars as of 2007.
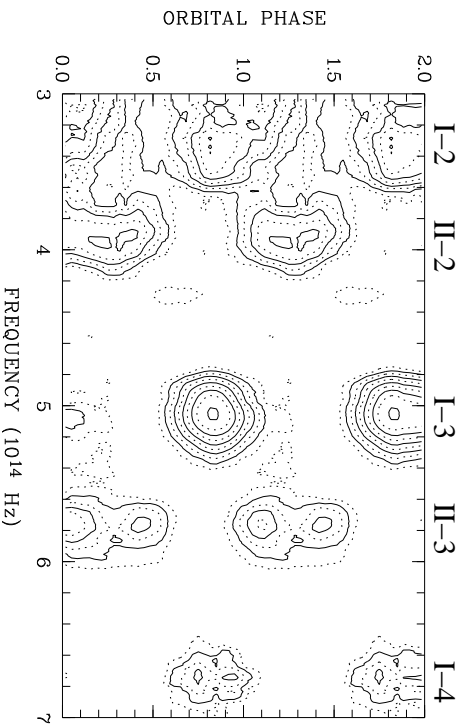
Figure 2.6: Contour plot of the phase-dependent cyclotron spectra from the two accretion regions on the white dwarf in WX LMi. Frequency is given in units of 10^{14} Hz. Numerals at the top indicate the frequencies for the different cyclotron harmonics. Roman numerals indicate the primary and the secondary spot. Arabic numerals indicate harmonic numbers.

2.5 The accretion scenario

The cyclotron spectra from the two accretion regions on the white dwarf in WX LMi were extracted from the original data in the same manner as is described by Reimers et al. (1999). We first corrected the spectra to radial velocity zero, arranged the spectra as a trailed spectrogram by phase-averaging the spectra into 30 phase bins of the same length and subtracted the suitably scaled spectra of our template Gl 268 (M4.5). This gave us spectra containing mainly photospheric radiation from the white dwarf and cyclotron radiation from the accretion spots (see Fig. 2.9 for a graph of the spectral decomposition). In the following we use the terms 'accretion region' and 'pole' synonymously for brevity.

Assuming a flat light curve from the rotating white dwarf, a mean white dwarf spectrum was composed from spectral regions free of cyclotron radiation and subtracted from all phase-binned spectra. Those difference spectra are regarded as having a pure cyclotron origin. They were arranged as a trailed spectrogram and are shown on a logarithmic intensity scale in Fig. 2.6. Roman numerals above the figure indicate cyclotron featurs from the primary and the secondary spot. Arabic numerals indicate the cyclotron harmonic. Actually, the described procedure was performed for the red and blue TWIN spectra and the MOSCA separately and the trailed spectrogram shown in Fig. 2.6 is a composite of those. The MOSCA data are used for the blue end of the spectra, $\nu > 6.3 \times 10^{14}$ Hz, since their signal-to-noise ratio was superior to the TWIN spectra in that wavelength region. The feature at $\nu = 4.3 \times 10^{14}$ Hz ($\phi \sim 0.65$) is a leftover of the M star subtraction. Light curves for individual harmonics were computed by averaging the trailed spectrogram over certain wavelength ranges. The light curves for the 3$^{\rm rd}$ and 4$^{\rm th}$ harmonics from the brighter primary and the 2$^{\rm nd}$ and 3$^{\rm rd}$ harmonics from the fainter secondary pole are shown in Fig. 2.7. Since the continuum subtraction for the lowest frequencies was not completely satisfying, the light curve for the 2$^{\rm nd}$ harmonic of the primary pole is ignored for the detailed analysis. The light curves from both poles are double-humped for the higher harmonics, an effect of cyclotron beaming in an optically thin plasma. The light curves of the lower harmonics are single-humped with maximum brightness centred between the two beamed humps from

Figure 2.7: Light curves of the 3$^{\text{rd}}$ and 4$^{\text{th}}$ (thick line) cyclotron harmonics from the primary (bottom panel) and the 2$^{\text{nd}}$ (thick line) and 3$^{\text{rd}}$ harmonics from the secondary (top panel) accretion spot in WX LMi. The light curve for the 2$^{\text{nd}}$ harmonic of the second spot is smoothed to reduce the noise level.
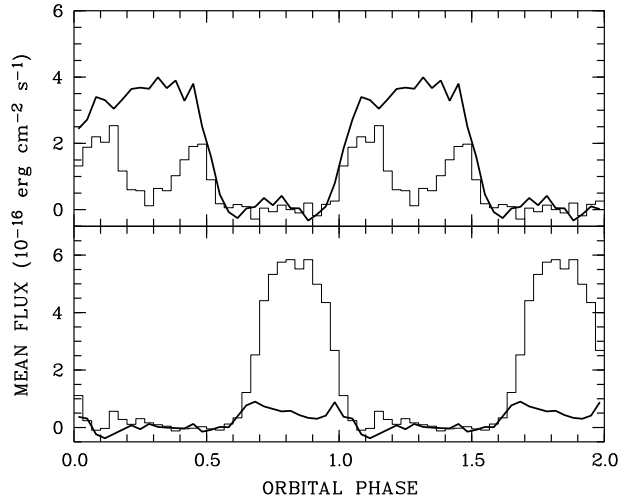
the higher harmonics, indicating considerable optical depth in those harmonics. From the centres of the bright phases, $\phi_{c1} \simeq 0.84$ and $\phi_{c2} \simeq 0.27$, the azimuth of both accretion spots were determined to $\psi_1 \simeq 55° \ldots 60°$ and $\psi_2 \simeq -90° \ldots -100°$. The phase-dependent spectra were modeled by Axel Schwope assuming homogeneous, isothermal conditions in the plasma (Chanmugam & Dulk 1981). A number of parameters determine the model spectra: the field strength B, the temperature kT, the plasma density coded with the density parameter $\log \Lambda$, the orbital inclination i, the co-latitude of the field in the accretion spot β_f, and the azimuth ψ_f of the field in the spot. The visibility of an emission region as a function of phase is further determined by the latitude β_s and azimuth ψ_s of the accretion spot and the vertical extent of the emission region. For simplicity, it was assumed that the field in the spot is normal to the surface of the star, i.e. $\beta_f = \beta_s$ and $\psi_f = \psi_s$. Furthermore any vertical extent of the emission region was neglected, but the point-like emission region was allowed to be raised to some height h above the star's surface. The orbital inclination was fixed at 70°. The difference in azimuth between the two regions was determined from the bright phase centres to $150° \ldots 160°$.

The main features of both cyclotron line systems as a function of phase could be reproduced fairly well with the following set of parameters: $B_{1,2} = 61.4/69.6\,\text{MG}$, $\log \Lambda_{1,2} = 2/2$, $kT_{1,2} < 3\,\text{keV}$, $h_{1,2} = 0.05/0.1\,\text{R}_{\text{wd}}$, $\beta_{1,2} = 145°/135°$ with typical uncertainties of $\Delta B = 0.5\,\text{MG}$, $\Delta \log \Lambda = 0.5$, $\Delta kT = 1\,\text{keV}$, $\Delta h = 0.05\,\text{R}_{\text{wd}}$, and $\Delta \beta = 15°$. The values given here are slightly different from those given in Schwope et al. (2002b) based on an analysis of the Reimers et al. data. The differences mainly reflect the modeling uncertainties and not a difference in the data. These were found to be consistent with each other. The new data provide the additional constraint of the beamed fourth harmonic from the primary pole, which was discovered in the MOSCA data. In our modeling, the co-latitude β was chosen according to the observed phase separation, $\Delta\phi_b$ of the two beamed humps in either the 4$^{\text{th}}$ (prime pole) or the 3$^{\text{rd}}$ harmonic (secondary pole). The value of β is related to the orbital inclination i and the length of the self-eclipse of an accretion spot, $\Delta\phi_s = 1 - \Delta\phi_b$, via

$\cos(\pi\Delta\phi_s) = -\cot(i)\cot(\beta)$. With the values of β and i fixed, we had to assume a certain height of the region in order to reflect the length of the bright phase, which lasts longer than the phase separation of the beams. The more extended visibility of the individual spots was used by Schwarz et al. (2001) for their estimate of the accretion geometry. They determined the colatitude β of both spots as $90° − 110°$ from light curve modeling for a point source on the surface on the WD. Using the beaming properties of the 3rd harmonic from the second pole, the range of possible values for the colatitude of the second pole was extended up to $130°$, which agrees with our results. Since we are using solely the beaming properties of the cyclotron radiation for both spots, our results seem to give more reliable constraints than the assumption of simple geometrical foreshortening.

These results are unusual as far as the spot locations and the plasma temperatures and densities are concerned. The two spots are both located in the 'southern' hemisphere of the white dwarf, a result already mentioned by Schwarz et al. (2001). The opening angle between the two spots is roughly $160°$; i.e. the two spots could be located at the two footpoints of the same dipolar fieldline. If so, the southern latitude of both spots hints at an off-centred field configuration. The slight difference between the field strengths in the two spots seems to underline this, although the strong radial dependence of the field strength does not allow firm conclusions about the field at the proper footpoints at zero height. One pole lies in the sector leading the secondary in phase. This is the sector where most poles in high-accretion rate polars are found (Cropper 1988). The other pole is $90°$ away from the line connecting both stars and away from the direction of a hypothetical accretion stream.

The plasma temperatures in the two accretion regions cannot be determined with very high accuracy. They are constrained by the width of the observed highest harmonic. At temperatures higher than about $3\,\mathrm{keV}$, the predicted line width becomes larger than observed even for point-like emission regions. Since in nature there will be a spread in kT and B, we regard $\sim 3\,\mathrm{keV}$ as a strict upper limit. Thus the temperatures found by us are among the lowest found in cyclotron spectra of polars (if WX LMi may be termed as such, see the discussion below). They are more than an order of magnitude below the shock-jump temperature for an assumed $0.6\,\mathrm{M_\odot}$ white dwarf. The low temperatures, together with the low density parameters Λ, imply that both cyclotron emission regions are dominated by cyclotron cooling. It seems unlikely that an accretion shock exists in WX LMi, because the accretion spots are more likely heated by particle bombardment. The bombardment models by Fischer & Beuermann (2001) relate the accretion rate per unit area, $\dot{m}$, to the field strength and the maximum electron temperature. According to Fischer & Beuermann (2001), one needs a specific mass accretion $\dot{m} \sim 0.1\,\mathrm{g\,cm^{-2}\,s^{-1}}$for a $0.6\,\mathrm{M_\odot}$ white dwarf with $T_{\max}/T_{\mathrm{shock}} \sim 0.1$ and $B = 65\,\mathrm{MG}$ in order to be deeply in the bombardment regime.

The mean integrated cyclotron flux calculated from the observable parts of the cyclotron spectra are $F_1 \simeq 1 \times 10^{-12}\,\mathrm{erg\,cm^{-2}\,s^{-1}}$ and $F_2 \simeq 0.4 \times 10^{-12}\,\mathrm{erg\,cm^{-2}\,s^{-1}}$. The correcting factors κ for the unobserved parts of the cyclotron spectrum and for the beaming pattern

are rather uncertain, so we assume $\kappa = 1 - 2$. We further assume that the cyclotron luminosity can be calculcated as $L_{\mathrm{cyc}} = \kappa \pi F d^2$ and get $L_{\mathrm{cyc}} \simeq (0.4 - 1) \times 10^{30} \, \mathrm{erg s^{-1}} (d/100 \mathrm{pc})^2$ for the sum of both poles. The implied mass accretion rate of $\dot{M} \simeq 1.5 \times 10^{-13} \, \mathrm{M_\odot \, yr^{-1}}$ is extremely low and is within the same order as the wind mass-loss rate of the secondary star. Given the total and the specific mass accretion rates, one may ask for the minimum area over which accretion may happen in order to be in the bombardment regime. Equating $\dot{m} = \dot{M}/f_{\mathrm{accr}} 4\pi R_{\mathrm{wd}}^2$ and using $\dot{m} = 0.1 \, \mathrm{g \, cm^{-2} \, s^{-1}}$, $\dot{M} \simeq 1.5 \times 10^{-13} \, \mathrm{M_\odot \, yr^{-1}}$, and $R_{\mathrm{wd}} = 8 \times 10^8 \, \mathrm{cm}$, we obtain a radius of just $40 \, \mathrm{km}$ or $f_{\mathrm{accr}} \sim 1.2 \times 10^{-5}$ for two equally sized circular accretion spots.

2.6 The white dwarf

The UV-observations with the OM were designed to estimate the temperature of the white dwarf and of the heated photosphere below the accretion spots. The basic assumption is that the UV light is completely dominated by photospheric radiation from the white dwarf's surface. Any variability is thus assigned to the temperature inhomogeneities of the atmosphere. We spent each half of the available observation time for the U ($3440 \, \text{Å}$) and UVW1 ($2910 \, \text{Å}$) filters. We detected a clear, phase-dependent variability in the OM count rate in both filters correlated with the visibility of the accretion spots (see Fig. 2.3). The ratio of the count rates between the two filters, however, was constant within the errors, indicating only marginal T-variations.

White-dwarf model spectra for pure H, $\log g = 8$, non-magnetic atmospheres in the temperature range $8000 \, \mathrm{K} - 100000 \, \mathrm{K}$ (Gänsicke et al. 1995) were folded through the response curves of the OM with the different filters thus predicting a count rate in the given filter. The count-rate ratio between the two filters as a function of temperature is shown in Fig. 2.8. The ratio is a sensitive function of T_{eff} below $30000 \, \mathrm{K}$. In order to test the reliability of our 'bolometer', we retrieved calibration observations of the well-studied white dwarfs BPM 16274 and GD 153 from the XMM-Newton Science Archive. Their count rate ratios are also shown in the figure. The resulting count rate ratio predicts a temperature of $39000^{+4700}_{-3500} \, \mathrm{K}$ for GD 153 in agreement with values found in references listed in the white-dwarf data base[5], $37900 - 40100 \, \mathrm{K}$. The derived temperature of $17340^{+150}_{-80} \, \mathrm{K}$ for BPM 16274 is somewhat lower than the values of $18400 - 18700 \, \mathrm{K}$ found in the literature. We thus estimate the accuracy of the filter ratio method at about 10%.

The observed count-rate ratio around phase $\phi = 0.6$, when both spots are hidden from the observer, is 2.88 ± 0.26. This high ratio cannot be reproduced by our model atmospheres. The observed ratio indicates a softer spectrum, i.e. cooler atmosphere than the lower limit of $8000 \, \mathrm{K}$ for our models. Synthetic magnetic white-dwarf model spectra with a dipolar field structure for a pole field strength of 60 MG – kindly provided by S. Jordan – reduced this discrepancy, but also led to no satisfying result. It needs to be

---

[5]http://procyon.lpl.arizona.edu/WD/
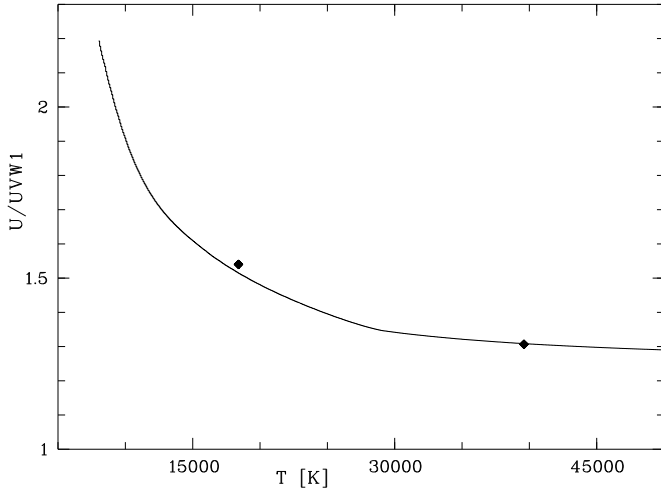
Figure 2.8: Theoretical count-rate ratio U/UVW1 using non-magnetic model spectra. Overplotted are measured count rate ratios for BPM 16274 with a temperature of 18700 K (Bragaglia et al. 1995) and GD153 with a temperature of 39600 K (Vennes et al. 1997). Error bars have sizes similar to the symbols.

said, however, that the model spectrum of a magnetised atmosphere uses the temperature structure of a non-magnetic atmosphere, so that we cannot quantify to what extent the magnetic model matches the observations better than the non-magnetic.

It is worth noting at this stage that we could not identify any depression (a line or a trough) in the optical continuum of the observed white dwarf spectrum, which could be even only tentatively identified as a Zeeman signal. We guess that the low T_{eff} and/or a complex field structure are responsible for this observation.

We conclude that T_{eff} of the white dwarf is almost certainly below 8000 K. Even without using the count-rate ratio as an indicator of the temperature, the measured count rate in the UVW1 filter around phase $\phi = 0.6$ gives an upper limit for the flux and thus the temperature of the white dwarf. One therefore has to assume that the whole white dwarf is seen, without contribution from the heated pole caps. If we fix the distance at 100 pc as derived in Sect. 2.4 and use a white-dwarf mass of 0.6 $M_{\odot}$, the lower limit of 8000 K of our nonmagnetic model atmospheres gives a flux that is about 12% higher than the measured flux in the UVW1 filter. We use the mass-radius-relation from Nauenberg (1972), which is sufficient for very cool white dwarfs (Panei et al. 2000). Any additional contribution from the accretion spots decreases the flux contributed by the white dwarf and thus its temperature. A significantly higher temperature would only be possible for a very massive white dwarf or if it were much farther away than the derived distance of 100 pc.

The different spectral components in the optical and near ultraviolet are illustrated in Fig. 2.9, which shows the mean optical spectrum, the scaled spectrum of the M4.5 template (Gl268), the blue TWIN spectrum after subtraction of the M dwarf (white dwarf plus cyclotron radiation), the two UV measurements and suitably-scaled magnetic and non-magnetic white-dwarf model spectra for $T_{\mathrm{eff}} = 8000$ K.

Reimers et al. (1999) determined the temperature of the white dwarf in WX LMi to be 13000 ± 1000 K, but our new determination differs significantly. Reimers et al. subtracted a

dM4.5e (G3-33) spectrum from a mean spectrum when both spots were self-eclipsed. The spectral energy distribution of the remaining spectrum was then compared with synthetic spectra for white dwarfs with a magnetic field of 60 MG. The temperature dependence of the continuum slope in the wavelength range between 4000 to 6000 Å used by them is not very pronounced. Due to the much smaller contribution of the secondary to the total flux in the UV, the use of the OM data seems more reliable to us for determining the white dwarf's temperature and we thus reject their temperature estimate. A white dwarf temperature of 13000 ± 1000 K would have been clearly detected in the OM, even at a distance of 140 pc.

The UV light curves in Fig. 2.3 show a clear variability correlated with the visibility of the accretion spots, a clear indication of heated pole caps. Surprisingly the secondary spot seems to be hotter than the primary pole, which is inconsistent with the picture obtained from the optical spectra and the X-ray light curve. The reason for this is rather unclear. We can exclude a cyclotron contamination because the OM U-filter is centred between harmonics 4 and 5 of the second pole.
The hardness ratio for the OM filters shows no significant variability, which is somewhat confusing since our interpretation of photometric variability of the UV also requires a hardness ratio variability. However, we cannot completely exclude that those expected count-rate ratio variations are below our sensitivity threshold and we cannot test this due to the lack of suitable model atmospheres.

2.7   Spectral energy distribution

Figure 2.9 shows the spectral decomposition of the optical and UV data into the photospheric radiation from the cool white dwarf, which dominates the UV completely, the strong cyclotron contribution in the optical and the secondary of spectral type M4.5 dominating the infrared. Figure 2.10 shows the spectral energy distribution for the complete observed wavelength range from the near infrared to the X-ray regime for the individual spectral components. The graph shows again λF_λ, i.e. the values plotted represent the contributions to the total energy output from the system. The cyclotron fundamentals are marked with arrows and are located in the H-band and between the H and K bands, respectively; i.e. the K-band is likely to be uncontaminated by cyclotron radiation. The X-ray spectrum is a mix of thermal plasma radiation from the accretion poles and the coronal plasma. Although the spectral energy distributions for the other low accretion rate systems, shown in Fig. 2.11, only provide a qualitative view, they exhibit the same tendency. Up to now WX LMi is the only low accretion rate polar with determined flux contributions of the cooling plasma for the cyclotron component and the bremsstrahlung component. The cyclotron luminosity exceeds the bremsstrahlung luminosity by far, thus the accretion-induced radiation is clearly dominated by the cyclotron component, which strongly supports the bombardement scenario for low accretion rates (Fischer & Beuermann 2001).

Figure 2.9: Observed and deconvolved optical spectrum and ultraviolet photometry of WX LMi. Shown are the observed mean spectrum (black top curve), the scaled spectrum of Gl268 (red), and the M-star subtracted spectrum (cyclotron radiation plus white dwarf, blue). The rhombs denote the OM photometry and the black lines at bottom denotes white-dwarf model spectra for a distance of 100 pc. The black dotted line is the non-magnetic white-dwarf model with $M_{wd} = 0.6 \, M_\odot$, and the black solid line denotes a magnetic white dwarf model with $M_{wd} = 0.47 \, M_\odot$, $B = 60 \, MG$, $d = 100 \, pc$.
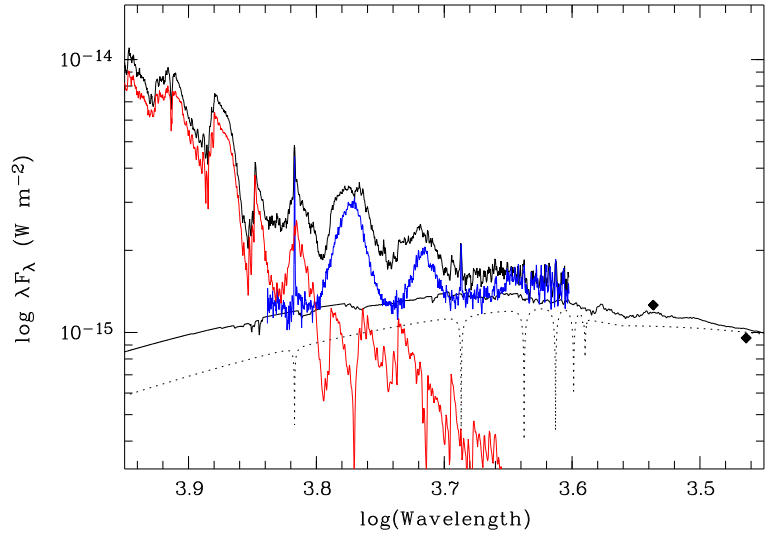
Figure 2.10: Spectral energy distribution for WX LMi combining photometry in JHK (2MASS, red squares) representing the secondary star, the OM onboard XMM-Newton (black rhombs), and the 8000 K non-magnetic white-dwarf model representing the white dwarf ($0.6 \, M_\odot$, d=100pc), the EPIC-PN spectrum as a mix of radiation from the accretion region and the coronal plasma, and the sum of the two cyclotron components (blue line). The arrows indicate the wavelengths of the cyclotron fundamentals for the two poles.
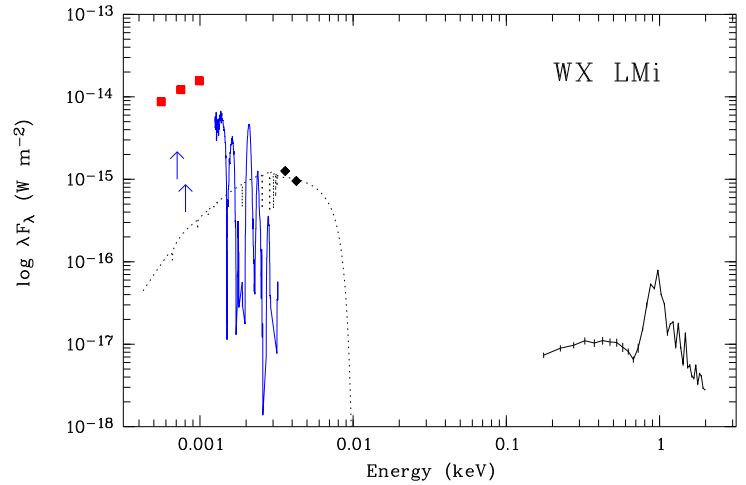
2.8 WX LMi as a pre-polar

The unusual low temperature of the white dwarfs in low accretion rate polars is evidence for the evolutionary state of these systems. During the post common envelope phase the degenerated core of the white dwarf cools down. Model calculations (Wood 1995, Chabrier et al. 2000) reveal a cooling time of 1×10^9 years for effective temperatures of 8000 K and 4×10^9 years for temperatures down to 4000 K. Schreiber & Gänsicke (2003) deduced a typical
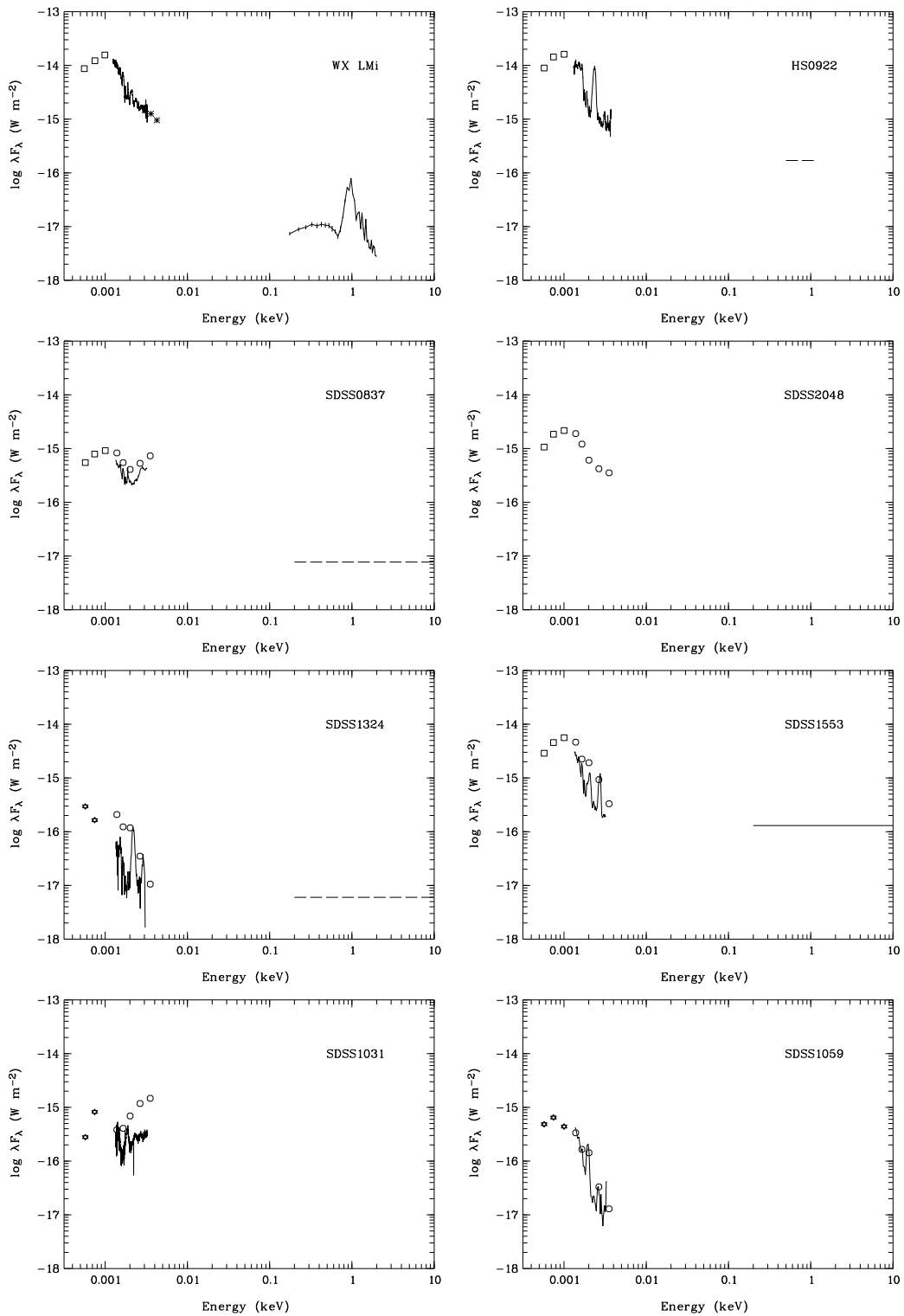
Figure 2.11: Spectral energy distribution for all known pre-polars with 2MASS data (square, upper limits: star), SDSS photometry (hexagon), XMM-OM data (asterisk) and X-ray data (dash, upper limits: long dash).

duration of about 2 Gyr for the post common envelope phase. Thus, CVs on the initiation of accretion due to Roche-lobe overflow should contain very cool white dwarfs. With the onset of Roche-lobe overflow the white dwarfs temperature increases due to the long-term compressional heating (see Section 1.3) and short-term heating by nova eruptions, leading to a white dwarf hotter than expected for its actual age. This counteracts the secular cooling and is the reason why no white dwarfs with temperatures below $11000\,$K are observed in normal CVs (Gänsicke 2000). Without any prior accretion, the temperature of the white dwarf in WX LMi implies a cooling age in the order of 10^9 years (Chabrier et al. 2000) as a lower limit. The low temperature also restricts the accretion rate in the past to less than $10^{-11}\,$M$_\odot\,$yr^{-1}, at least for periods shorter than the thermal timescale of the heated envelope, which can be shown by model calculations (Townsley & Bildsten 2003). The white dwarf temperatures of the other systems are summarized in Table 2.5. Apart from SDSS0837, all white dwarfs are cooler than $11000\,$K. Together with the low accretion rate this supports the assumption that WX LMi and the LARPs in general are pre-CVs before the onset of Roche-lobe overflow as already proposed by Webbink & Wickramasinghe (2005) and Schmidt et al. (2005).

This view is also supported by the spectral type of the secondary. At the given orbital period, $P_{\rm orb} = 2.78\,$h, one would expect a secondary of earlier spectral type than M4.5 (see Section 1.4 and Figure 1.7). In this respect the secondary seems to behave like those in normal accreting polars, but the standard explanation assuming the secondaries being driven out of thermal equilibrium does not seem to work here, since the low temperature of the white dwarf, $T_{\rm eff} < 8000\,$K, implies the absence of or a very low accretion rate in the past as shown above. If WX LMi and its relatives are just in an occasional low state of accretion, the expected temperature of the white dwarf should be above the lower limit of $11000\,$K. Also the observed accretion rate is too low for a long-term equilibrium mass transfer (Webbink & Wickramasinghe 2005) and the location of the second pole in WX LMi (see Section 2.5) makes accretion via Roche-lobe overflow rather unlikely.
As already suggested by Schwarz et al. (2001) for WX LMi and Schmidt et al. (2005) for similar systems found in the SDSS, the secondary is likely somewhat underfilling.

But if not by Roche-lobe overflow how does the accretion happens? The implied low mass transfer rate of $\dot{M} \simeq 10^{-13}\,M_\odot\,$yr^{-1}is likely to be compatible with the wind mass loss rate from the active secondary. Adopting a scenario by Li et al. (1995), Schmidt et al. (2005) proposed a 'magnetic siphon' channeling all material in the wind down to the pole caps with very little wind loss. The actual accretion geometry, determined by us from the orbital phases of the cyclotron features, does not seem to play an important role, once the magnetic field is sufficiently strong.

We applied successful for XMM time in AO-7 (2008/2009) to observe HS0922+1333. Due to its convenient one-pole accretion geometry, this observation will allow further investigations of the X-ray activity in (pre)polar secondaries and the accretion physics for very low mass accretion rates.

Chapter 3

The eclipsing polar
2XMMp J131223.4+173659

3.1 Introduction

As explained in the introduction polars generally show a strong soft X-ray component of
re-processed origin. This prominent feature led to the discovery of about 45 new objects in
EUVE/soft X-ray all-sky surveys (e.g. Beuermann & Burwitz 1995, Schwope et al. 2002a)
compared to about 20 known before ROSAT/EUVE. With the decommissioning of ROSAT
and EUVE new detections have become very infrequent. The public releases of the Sloan
Digital Sky Survey opened a new discovery channel. In a series of papers, Szkody et al.
2007 (and references therein) presented the serendipituous CV content of the SDSS-sky,
among the several 100 CVs a dozen magnetic objects were found. This small fraction is
likely being more representative of the underlying population. Most of the low accretion
rate polars - or better pre-CVs - introduced in the last chapter were discovered that way.
Since the launch of Chandra and XMM-Newton several large-scale optical identification
programs have been started (Champ, Champlane, AXIS, XBS, . . .). Not too surprisingly,
due to their small survey area compared with ROSAT and EUVE, none of these led to the
discovery of any further magnetic CVs. The XMM-Newton Survey Science Centre (SSC)
has processed and surveyed all public XMM-Newton observations performed so far. The
latest edition of the XMM catalogue, 2XMM, was made available in August 2007 (Watson
et al. 2007, in preparation), its less elaborated predecessor termed 2XMMp was published
already July 2006. Both catalogues have in common that for objects with more than 500
source photons X-ray spectra and light curves are prepared and published as standard
source products. Visual inspection of all light curves led to the serendipituous discovery of
2XMMp J131223.4+173659 (for brevity 2XMM1312 in the following). The source stuck
out as a bright and prominently variable object, showing periodic modulations of its X-ray
flux by 100% in the field of HD 114762, a high-proper motion star. Optical follow-up
observations secured the tentative identification as an magnetic cataclysmic variable. We

Date (Y/M/D)	Instrument	Total Duration [ksec]	Exp.time [sec]
2004/06/28	XMM-PN	29.4	
	XMM-MOS1	31.6	
	XMM-MOS2	31.6	
	XMM OM-UVW1	0.8	
	XMM OM-UVM2	1.3	
	XMM OM-UVW2	1.4	
2007/02/14	CAHA 2.2m CAFOS	8.7	300
2007/03/19	CAHA 2.2m (R)	14	30

Table 3.1: Log of X-ray and optical observations.

present an analysis of the initial X-ray observations, and the spectroscopic and photometric follow-up.

3.2   Observations

All X-ray and optical observations obtained so far are summarised in Table 3.1.

3.2.1   XMM-Newton X-ray and UV observations

XMM-Newton was targeting the field of HD 114762 (obs-ID 0200000101) on June 28, 2004, for almost 32 ksec. The observations were performed in full window imaging mode with all three cameras through the medium filter. Routine processing for the production of 2XMMp revealed the brightest X-ray source in the field at position RA, Dec (2000) = 13h12m23.46s,+17d36$'$59$.\!\!^{s}$5, with an error of 0.36 arcsec. The source was detected at an off-axis angle of ∼6.3 arcmin. More than 9500 photons from the source were collected by the three EPIC detectors corresponding to a mean count rate of 0.304 ± 0.003. The standard products (X-ray image, DSS finding chart, X-ray spectrum, X-ray light curve) were automatically generated and visually inspected.

The PN X-ray light curve showed a striking behaviour with a periodic on/off pattern on a time-scale of ∼90 min. The peak count rate during the bright phase reached $0.6\,\mathrm{s}^{-1}$. Five bright phases were covered by the observations. They were each disrupted by a short (∼ 300 s) eclipse or eclipse-like feature. The shape of the light curve in general, its periodic behaviour, the eclipse in the bright phase, were reminiscent of a synchronously rotating magnetic CV (e.g. Osborne et al. 1988, Schwope et al. 2001). Prior to eclipse the light curve shows a dip, a feature also found in AM Her stars and caused by absorption of X-rays when the emitting accretion region becomes eclipsed by the accretion stream (see

Table 3.2:
Count rates, fluxes and orbital phases for the observations with the optical monitor (OM) onboard XMM-Newton.

Filter	λ_{eff} [Å]	Countrate	Flux (10^{-16}) [erg cm^{-2}s^{-1}Å^{-1}]	Orbital phase
UVW1	2910	0.264 ± 0.045	1.26 ± 0.21	0.25 - 0.40
UVM2	2310	0.099 ± 0.022	2.2 ± 0.5	0.97 - 0.21
UVW2	2120	0.039 ± 0.019	2.2 ± 1.0	0.52 - 0.77

Chapter 1). This striking light curve triggered a more detailed analysis of the X-ray data and optical follow-up to secure the tentative identification.

We reanalysed the X-ray data obtained with XMM-Newton using SAS version 7.0. The usable energy range of the PN detector was extended down to 150 eV using *epreject*. Light curves and spectra were generated according to the SAS Manual. 2XMM1312 provided ∼6200 photons in the EPIC PN detector, ∼2000 photons in the EPIC MOS1 detector and ∼1700 photons in the EPIC MOS2 detector. The background-corrected, binned X-ray light curve of 2XMM1312 is reproduced in Fig. 3.1. The same data, folded and averaged over the orbital period of 91.85 min (see Sect. 3.3), are shown together with the optical light curve in Fig. 3.4. The mean X-ray spectrum is reproduced in Fig. 3.5 (we note that 2XMM1312 was not detected by ROSAT or by INTEGRAL).

The XMM optical monitor (OM) was operated in default imaging mode with the U, UVW1, UVM2 and UVW2 filters. 2XMM1312 was detected in UVW1, UVM2 and UVW2, the U filter did not cover the new CV. Since the OM imaging mode does not allow for timing information, we only get an average flux for the corresponding phase interval. This information is summarized in Table 3.2.

3.2.2   Optical observations from Calar Alto

The X-ray position of 2XMM1312 was found to be coincident with the blue object SDSS J131223.48+173659.1 having *ugriz* magnitudes of 19.66, 19.69, 19.76, 19.81, 19.83, respectively. A finding chart of the field around the new CV is reproduced in Fig. 3.2.

Time-resolved low-resolution spectroscopy

Optical low-resolution spectroscopy was performed on Feb. 16 2007 between UT 03:05 - 05:30 from Calar Alto with the 2.2m telescope. The telescope was equipped with the low-resolution spectrograph and camera CAFOS. The B-400 grism was used as disperser

Figure 3.1:
Combined PN and MOS light curve with a binning of 110s for the energy range 0.15-12.0 keV. Zeropoint is BJD = 2453185.0. For a phase folded light curve see Fig.3.4
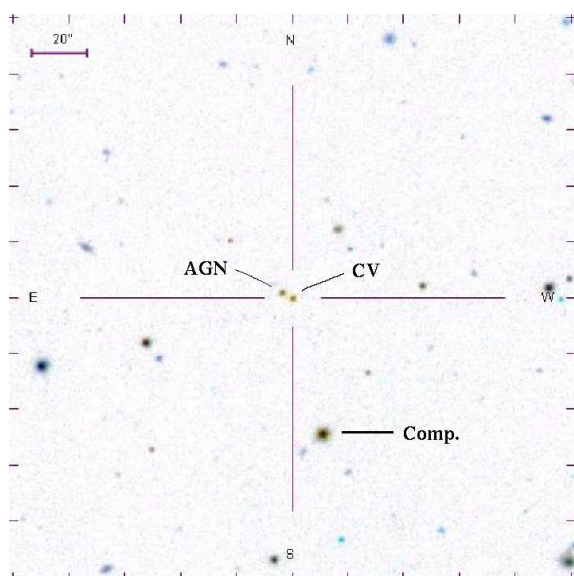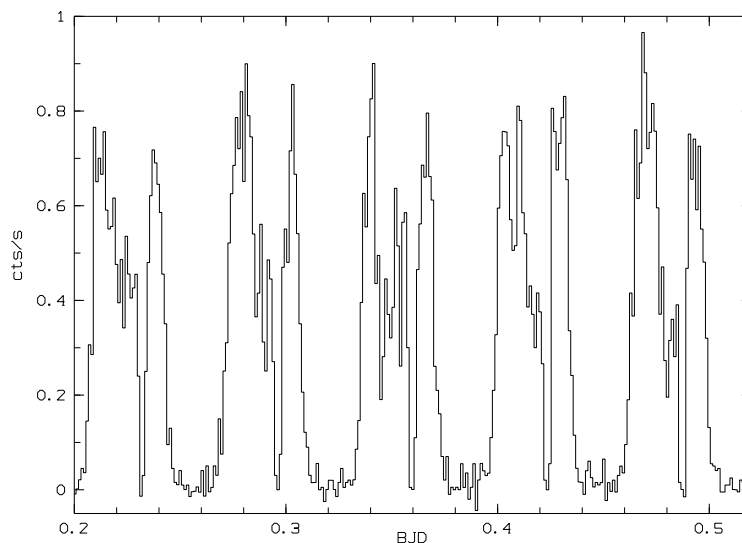
Figure 3.2:
Finding chart of 2XMM1312created with the SDSS finding chart tool. The new CV, the nearby AGN and the comparison star used for differential photometry are marked.

resulting in spectra with full coverage of the optical range from $3500 - 9500$Å with a resolution of ~ 28Å (FWHM). A sequence of 20 spectra was taken with individual exposure times of 5 min each. The weather conditions were stable, the object SDSS J131223.75+173701.2 located 4.4 arcsec NE to the candidate ($ugriz = 20.72$, 19.84, 19.67,19.59, 19.37) was put nevertheless on the spectrograph's slit to correct for slit losses and variable seeing. The observations were accompanied by exposures of HgHeRb arc lamp spectra for wavelength calibration and of the standard star BD +75 325 for calibration of the instrumental response.
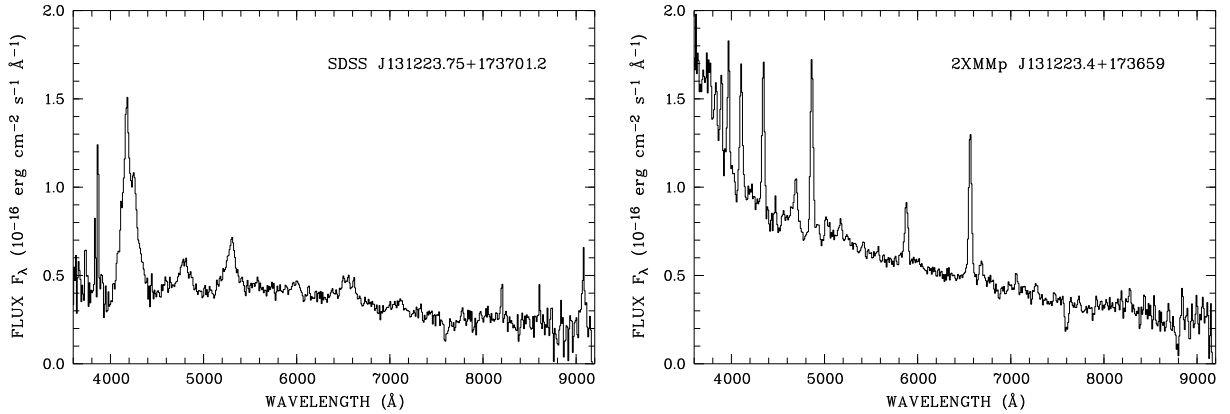
Figure 3.3:
Average spectrum of SDSS J131223.75+173701.2 (left) and 2XMM1312 (= SDSS J131223.48+173659.1) both obtained at Feb. 16, 2007 with the CA 2.2m telescope and CAFOS (total exposure 100min).

Data reduction was performed with ESO-MIDAS[1].

The mean spectrum of the CV candidate is reproduced in Fig. 3.3 (right panel) and – together with the X-ray light curve – identifies 2XMM1312 as a magnetic CV of AM Herculis type. Approximate BVR-band light curves of the CV were constructed by folding the final spectra through the response curves of Bessel filters and are reproduced in Fig. 3.7. Those light curves also show an eclipse, there is one spectrum with a non-detection of the target object resulting in an upper limit to the brightness of the object of $V \sim 21\overset{m}{.}5$.

The second object on the slit used by us as photometric calibration source turned out to be a quasar at redshift $z = 2.43$ with strong and broad emission lines of Lyα, SIIV, CIV 1550, and CIII 1900. The mean spectrum of the QSO is reproduced in Fig.3.3 (left panel).

Time-resolved differential R-band photometry

Optical R band photometry was performed one month after the spectroscopy on March 19 between UT 00:32 - 04:25 with an exposure time of 30 seconds at the Calar Alto 2.2m telescope. A total of 305 exposures were taken covering two and a half cycles of the binary and three eclipses. The comparison used for photometric calibration is marked in Fig. 3.2.

The already phase folded light curve of the CV is shown in Fig. 3.4 together with the X-ray light curve (see Sect. 3.3 for the ephemeris). A zoomed-in version of the same data

---

[1]http://www.eso.org/sci/data-processing/software/esomidas/

Figure 3.4:
The upper panel shows the phase folded X-ray light curve from 2004 composed of EPIC PN and MOS counts with a binning of 0.02 phase units. The lower panel shows the phase folded R band light curve from 2007.
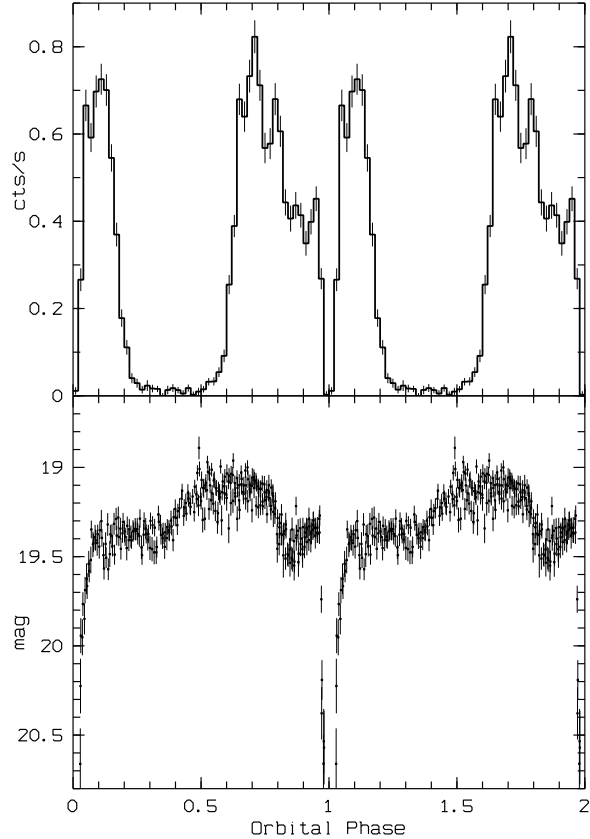
centred on the optical eclipse is shown in Fig. 3.11. Similar to the X-ray light curve, the overall light curve shows a bright hump followed by a dip prior to the eclipse.

Out of eclipse, the R-band brightness varied between $\sim 19.^{\mathrm{m}}1$ and $\sim 19.^{\mathrm{m}}4$. The CV was not detected in the individual exposures at the bottom of the eclipse. A stacked image using those 11 images was created. From the statistical analysis of that image we derived an upper limit of $22.^{\mathrm{m}}3$ for the brightness of the secondary.

The orbital period of $\sim$92 min (see next Section) implies a spectral type of M5.5$\pm$0.5 (Beuermann et al. 1998). Using the absolute magnitudes from Kirkpatrick & McCarthy (1994) this results in a minimum distance of ~ 900 pc for a M5 and ~ 350 pc for a M6 spectral type.

3.3   A combined X-ray/optical ephemeris

We found an eclipse in all three datasets obtained so far. This excludes anything else than an eclipse proper by the mass-donating secondary star. Here we make an attempt to

combine the eclipse epochs from the three sets into one binary ephemeris. For the analysis of the X-ray data a combined light curve of all three EPIC cameras with a binning of 5 seconds was used. The X-ray eclipse shows just the ingress and egress of the accretion spot and does not resolve any detail. The individual X-ray eclipse timings with an uncertainty equal to the used bin size were used to determine the times of mid-eclipse. The mean X-ray eclipse length resulting from the five individual eclipses is 329(6)s.

The exposure time of the optical spectra was 300 seconds, but the last spectrum in our sequence of 20 did not yield a significant detection. Since the length of the X-ray eclipse is slightly longer than the exposure time of 300 seconds, we assume that this spectrum is centred on the X-ray eclipse with rather small uncertainty (compared to the exposure time) of 60 seconds only.

The mean eclipse light curve from the R band photometry (see Fig. 3.11) shows clearly ingress and egress of white dwarf and/or spot and accretion stream. Since the individual eclipses do not resolve these details, we used the mean eclipse light curve – phase folded with the period derived from the X-ray data – to determine the flux level for mid-ingress and mid-egress of the white dwarf/spot. For the individual eclipses we interpolated between single exposures to get the timings for the chosen flux level and thus the times of spot ingress and egress.

The five consecutive X-ray eclipses were used to derive a preliminary period which could be used to connect the eclipse times obtained from spectroscopy and photometry at Calar Alto without cycle count alias and improve the accuracy of the value of the period. This turned out to be sufficiently accurate to connect the XMM-Newton X-ray data from 2004 with the optical data from 2007, again without cycle count alias. A linear regression using all nine eclipse epochs revealed the finally accepted eclipse ephemeris of:

$$\text{BJD(UT)} = 2453185.23204(4) + E \times 0.06378527(1) \tag{3.1}$$

which corresponds to an orbital period of $\text{P}_{orb} = 91.85079(1)$ minutes. Numbers in parentheses indicate the uncertainties in the last digit. All phases in this paper refer to the linear ephemeris of Eq. 3.1. The mid-eclipse times for all eclipses are given in Table 3.3.

3.4 Analysis of the X-ray spectrum

The X-ray spectrum was made from the PN and MOS event lists according to the SAS manual. Spectral fits were generated using Xspec[2]. A fit to all three EPIC mean spectra (see Fig. 3.5) with an absorbed MEKAL model gave a good fit with a reduced χ^2_ν of 1.01 and resulted in a plasma temperature of kT = 29(8) keV and a column density of $\text{N}_H = 2.0(6) \times 10^{20}$ cm^{-2}. The *nh* tool from the FTOOLS package[3] gives for the target

---

[2]http://heasarc.gsfc.nasa.gov/docs/xanadu/xspec/
[3]http://heasarc.gsfc.nasa.gov/docs/software/ftools

Observation	Time [BJD]	Cycle	O-C [sec]
XMM EPIC 2004	2453185.232033(82)	0	-0.6
XMM EPIC 2004	2453185.29854(82)	1	2.5
XMM EPIC 2004	2453185.359591(82)	2	-1.7
XMM EPIC 2004	2453185.423446(82)	3	4.3
XMM EPIC 2004	2453185.487154(82)	4	-2.3
CAHA Spec 2007	2454146.7313(7)	15074	8.6
CAHA Phot 2007	2454178.5600(4)	15573	-4.3
CAHA Phot 2007	2454178.6240(4)	15574	14.3
CAHA Phot 2007	2454178.6875(4)	15575	-10.4

Table 3.3: Mid-eclipse timings
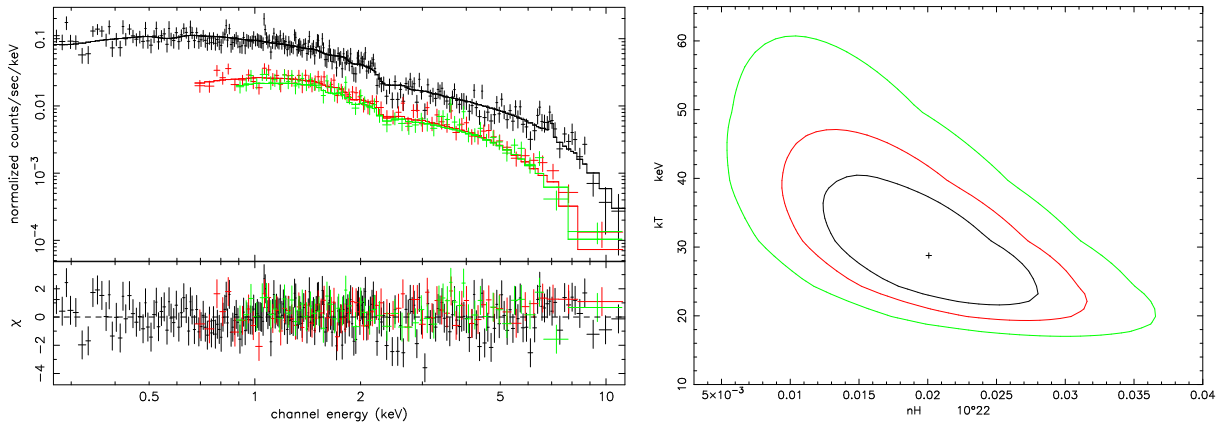
Figure 3.5:
Spectral fit of the combined PN and MOS mean spectra with an absorbed MEKAL model, together with the confidence range (0.68, 0.90 and 0.99) as a function of the MEKAL temperature and the column density of the interstellar absorption.

coordinates a Galactic column density of $N_H = 1.87 \times 10^{20}$ cm^{-2}. The target coordinates correspond to a galactic latitude of 79°, so this value seems still reasonable with respect to the estimated distance. The unabsorbed flux is 1.4×10^{-12} erg s^{-1} cm^{-2} in the energy range from 0.15 to 12.0 keV. We also tried to model the spectrum with a more complex absorption component using the pcfabs model in Xspec, but this led to no meaningful fit, since the parameters of the absorber were not constrained by the fit. The above model parameters results in a predicted ROSAT count rate of 0.03 cts/s, slightly below the RASS detection limit of 0.05 cts^{-1}, which explains the non-detection during the RASS if we assume a comparable accretion state for the XMM and the ROSAT observation and even if we assume that the RASS scans covered the bright phase.

We also created a combined spectrum for the bright phase intervals, excluding the
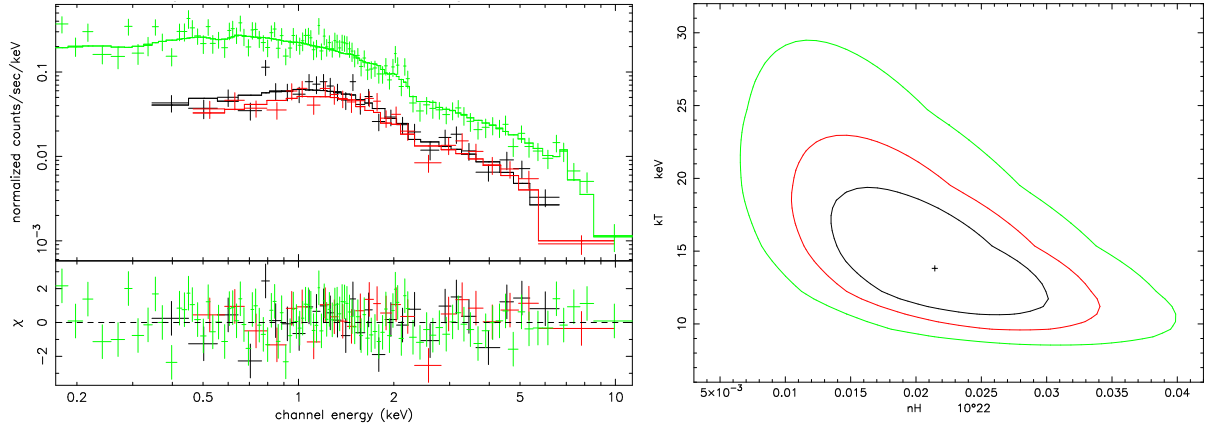
Figure 3.6:

Spectral fit of the combined PN and MOS spectra of the X-ray bright phase before the absorption dip with a absorbed MEKAL model, together with the confidence range (0.68, 0.90 and 0.99)as a function of the MEKAL temperature and the column density of the interstellar absorption. The bright phase interval was selected individually for each of the five orbits.

phase intervals where the absorption dip occurs. This corresponds to orbital phase ~ 0.6 - ~ 0.8. The phase intervals were visually selected for each individual orbit. A fit with an absorbed MEKAL model resulted in a plasma temperature of kT = 14(4) keV and a column density of $N_H = 2.1(7) \times 10^{20}$ cm^{-2} ($\chi^2_\nu = 1.01$). The spectral fit together with the confidence range is shown in Fig. 3.6. Since at the given phase interval the accretion region is directly exposed towards the observer, a fit to this spectrum reveals the most likely plasma temperature. The unabsorbed flux is 2.72×10^{-12} erg s^{-1} cm^{-2} in the energy range from 0.15 to 12.0 keV, the bolometric flux 3.8×10^{-12} erg s^{-1} cm^{-2}, which results in an accretion luminosity of $L_{accr} \geq 0.6 - 3.7 \times 10^{32}$ erg s^{-1}, depending on the assumed minimum distance. The luminosity can be compared to the expected accretion luminosity. According to the standard theory the mass transfer below the period gap is driven solely by the angular momentum loss due to gravitational radiation. The caused mass transfer rate for the derived orbital period is given by

$$\dot{M}_{\text{grav}} = 2.4 \times 10^{15} \; \frac{M_1^{2/3} (\text{M}_\odot) \; P_{\text{orb}}^{-1/6}(\text{h})}{(1 - \frac{15}{19} q)(1+q)^{1/3}} \; \text{g s}^{-1} \; (P_{\text{orb}} \lesssim 9 \, \text{h}) \tag{3.2}$$

(with $q = M_2/M_1$) and would be $\dot{M} = 2.8 \times 10^{-11}$ M$_\odot$ yr^{-1} (Warner 1995). The amount of energy released during the accretion process for the given mass transfer rate can be estimated by the kinetic energy gain of the matter starting at the first Lagrangian point and falling onto the white dwarf surface:

$$L_{acc} \approx \frac{GM_1\dot{M}}{R_{wd}}, \tag{3.3}$$

The resulting accretion luminosity is $L_{accr} = 1.6 \times 10^{32}\,\mathrm{erg\,s^{-1}}$. This is in good agreement with the actual luminosity. The used masses of white dwarf and secondary for Eq. 3.2 and 3.3 are derived in section 3.8.

Interestingly and contrary to the standard picture of magnetic accretion in AM Herculis stars which emerged from the analysis of the large body of e.g. ROSAT data, the X-ray spectrum of this object reveals no evidence for the presence of a distinct soft component. This soft component originates from the heated atmosphere of the white dwarf around the accretion spot. 2XMM1312 thus joins the group of now 9 out of ~ 90 polars without a soft component (Ramsay & Cropper 2007). A likely explanation for the non-detection of a soft component is its low temperature which shifts the emission towards lower energies not covered by the X-ray cameras of XMM-Newton. To derive upper limits for the soft component, we model this component with a black body spectrum based on the constraints that the Rayleigh-Jeans tail of the assumed black body must not exceed the observed spectral flux in the ultraviolet, and that the contribution of the soft component to the 0.15–0.30 keV band is less than 10%, to make it undetectable in our spectral analysis. With a 0.6 $M_\odot$ white dwarf and a distance of 900 pc the fraction of the white dwarf surface which is covered by the pole cap falls below 10^{-3} for a temperature above 15 eV, so we claim this as the upper temperature limit.

This temperature is at the lower end of the otherwise observed temperatures for the soft component, but is still too high to contribute in the UV. To test for the energy balance of the reprocessed component we assumed a black body with a temperature of 10 eV, providing 10% of the flux in the 0.15–0.30 keV band (see Fig. 3.8). The resulting contribution in the UVW2 filter is still less than one fourth, but the integrated flux exceeds the flux of the bremsstrahlung component by a factor of hundred. So the UV and X-ray observations give no constraints for the maximum flux contribution of the soft component that could lead to a conflict with the standard model. In summary, the missing soft component is not really puzzling. If the accretion occurs over a large fraction of the white dwarf surface, the temperature of the pole cap would be lower than oberserved in polars with soft component. The lower temperature simply shifts the observable soft component towards the EUV, out of the XMM band pass.

3.5 The X-ray eclipse emission

The EPIC light curve shows a residual X-ray flux of $F_X = 1.2 \times 10^{-14}\,\mathrm{erg\,cm^{-2}\,s^{-1}}$ when the white dwarf and the accretion region is eclipsed by the secondary. The origin of this emission is not obvious at first glance. 2XMM1312 is accompanied by SDSS

J131223.75+173701.2 at a distance of 4.4 arcsec. We found from our spectroscopic observation that this object is a quasar at redshift $z = 2.43$. The quasar is not resolved in our XMM EPIC data, but quasars are known to be X-ray emitters. We tried two methods to distinguish between the two sources to clarify if the residual X-ray emission emerge from the AGN or from the corona of the secondary star (if the secondary is X-ray active at all).

Our first attempt was to spatially resolve the polar and AGN by using phase selected event lists for bright, faint and eclipse phase on which the SAS source detection was run. All three source positions found were the same within the error circles, which is not surprising since the distance between both sources is at the limit of the spatial resolution.

The next attempt was to use the properties of the spectral energy distribution. We computed the flux from the dozen photons during eclipse, taking the interstellar absorption from the spectral fit above into account. The X-ray flux of $F_X = 1.2 \times 10^{-14}\,\mathrm{erg\,cm^{-2}\,s^{-1}}$ was then compared with the optical flux. From the SDSS magnitudes of the AGN we computed a optical flux of $F_{opt} = 2.76 \times 10^{-14}\,\mathrm{erg\,cm^{-2}\,s^{-1}}$ (Zombeck 1990). The ratio F_X/F_{opt} = 0.4 can be compared with the properties of other AGNs. For most AGNs F_X/F_{opt} is found to be between 1 and 10, but can also be one order of magnitude less, while for stars this ratio is mostly below 0.05 (Schwope et al. 2000). Ascribing the complete flux to the secondary, the X-ray flux transforms into a luminosity of $L_X = (1.8 - 11.6) \times 10^{29}\,\mathrm{erg\,s^{-1}}$. The assumed spectral type and the distances (see Sect.3.2.2) lead to a bolometric luminosity of $L_{bol} = (3.18 - 3.43) \times 10^{30}\,\mathrm{erg\,s^{-1}}$ (Leggett et al. 1996), and thus $L_X/L_{bol} \sim 0.3$ for a M5 and ~ 0.06 for a M6. This is orders of magnitudes above the value which could be expected for an active M dwarf (Pizzolato et al. 2003). As the assumed distance increases L_X and thus L_X/L_{bol} also increases, making the ratio even larger.

Therefore we suggest to ascribe the residual X-ray emission during eclipse to the AGN. Since the contribution from the AGN is rather small and the real flux contribution is uncertain, we neglect the contribution by the AGN for any further analysis of the X-ray data. Since we have more flux during faint phase than during the time of eclipse, there must be an additional contribution at this time. Either the self-eclipse is not complete or we see bremsstrahlung reflected at the accretion stream. Due to the low number of photons we could not made any viable conclusion from the hardness ratio.

3.6   The optical spectrum

The optical spectrum of our target object clearly reveals its nature as a CV through the presence of a blue continuum with strong superposed emission lines of H, HeI and HeII. Our initial spectroscopy revealed the presence of an optical eclipse. Apart from the eclipse proper the light curves in BVR bands are modulated by $\sim 50\%$ and show one bright hump with a colour-dependent phase of maximum emission. The shift between B and R band hump could be caused by beaming properties of the cyclotron radiation, which is more beamed at higher harmonics (shorter wavelengths), but the difference between
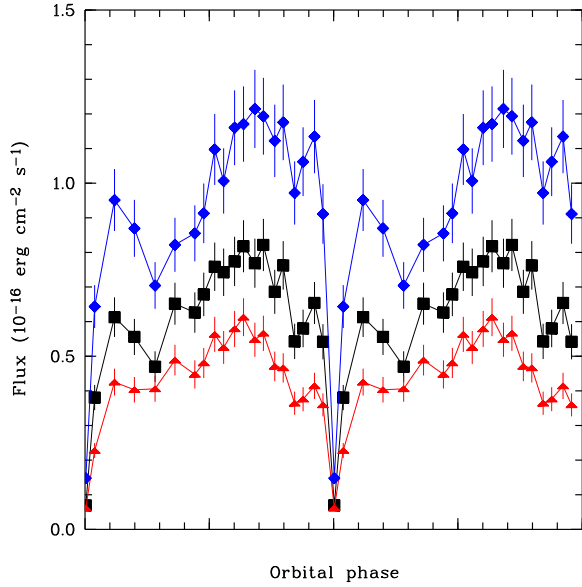
Figure 3.7:
Optical light curves in BVR (in descending order) bandpasses determined from flux-calibrated phase-resolved spectra of Feb. 16, 2007.

the average spectra in phase intervals 0.5–0.8 (brightest phase interval) and 0.2–0.4 (faint phase) displays just a smoothly varying blue continuum and does not show any feature which could be associated with a cyclotron harmonic hump. The more likely explanation is to assume a different cause of both humps. The center of the B band bright phase corresponds to the center of the X-ray bright phase at phase ~ 0.9, thus the B band hump is likely to originate from the heated pole cap, while the R band hump can be explained by cyclotron origin (see Sect. 3.8). This implies a cyclotron component which contributes in the red and infra-red and thus a probably low field strength. Unfortunately we found no indication of Zeeman split lines in the spectra, which could be used to determine the magnetic field strength directly.

As a rough guess for the contribution of the cyclotron component we computed the flux difference between faint phase and bright phase. This clearly is an upper limit for the cyclotron flux since it contains an undetermined fraction of atmospheric emission from the accretion-heated spot. If we nevertheless regard the contribution of $1.1 \times 10^{-13}\,\mathrm{erg\,cm^{-2}\,s}$ during bright phase as of pure cyclotron origin and apply a factor of 2 for correction of beaming properties and unobserved cyclotron features, one gets $F_{\mathrm{cyc}}/F_{\mathrm{X}} \leq 0.1$, which demonstrates the prevalence of plasma cooling via bremsstrahlung over cyclotron cooling and also indicates low field strength. A low field strength would be a natural explanation for the shifted soft component (Beuermann 2004 and references therein). Considering the other polars without observed soft component this view is not unambiguous. Indeed they include V2301 Oph with $B \sim 7$ MG (Ferrario et al. 1995), the polar with lowest observed field strength so far, but also systems with high field strengths as WW Hor (25 MG) and CE Gru (25-50 MG).
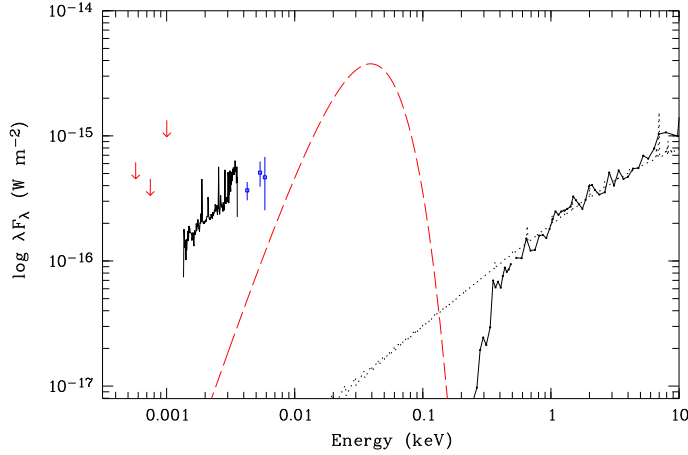
Figure 3.8:
Spectral energy distribution with all available data: 2MASS upper limits (red arrows), CAHA mean spectrum (black), XMM OM (blue) and XMM EPIC spectrum (black). Overplotted (long dash) is a 10 eV black body providing a negligible fraction of 10% of the observed soft X-ray flux and the MEKAL model spectrum (dotted line), demonstrating the effect of interstellar absorption.

3.7 Overall flux distribution

The spectral energy distribution with all available data is shown in Fig. 3.8. 2XMM1312 has no detection in 2MASS, so we could just derive an upper limit for the JHK bands. While optical and X-ray spectrum represent the mean over the orbital cycle, the UV data points belong to specific orbital phases (see Table 3.2). From the spectral energy distribution it becomes clear that we have a strong contribution from the accretion stream in the UV. The UVW1 filter covers just the faint phase, where the accretion spot is self-eclipsed and does not contribute. Assuming a low temperature white dwarf the optical flux gives an upper limit to the contribution of the white dwarf. For a high temperature white dwarf the flux in the UVW2 band gives an upper limit. Using white dwarf model spectra a 20000 K the white dwarf could provide ~ 70 percent of the flux in the UVW1 band, a 11000 K white dwarf just ~ 60 percent. The remaining flux has to be provided by the accretion stream. Also included in Fig. 3.8 is a black body spectrum for a temperature of 10 eV, providing 10% of the 0.15 – 0.3 keV X-ray flux, to visualise the possible contribution of the soft component.

3.8 Binary parameters and system geometry

The optical mean eclipse light curve (see Fig. 3.11) indicates obviously the ingress and egress of the white dwarf/accretion spot and the stream. The width of spot eclipse is 320(3) seconds compared to the X-ray eclipse length of 329(6) seconds. The stream ingress lasts until phase 0.995, the stream egress until phase $\sim$1.08. We used the steep decline during eclipse ingress as a consistency check for the binary distance as derived from the spectral type of the secondary. While the gradual decline is caused by the accretion stream,
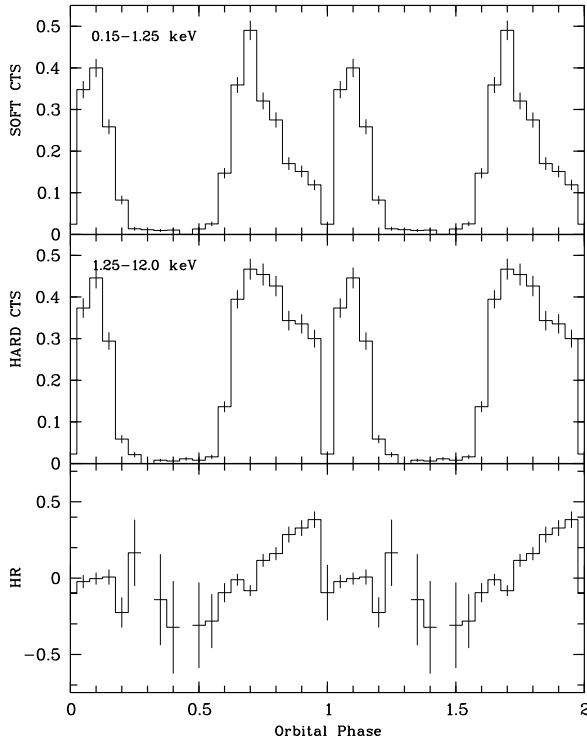
Figure 3.9:
PN light curve for soft (0.15-1.25 keV) and hard (1.25-12.0 keV) energy range together with the resulting hardness ratio. Soft and hard band contain approximately an equal number of photons ($\sim$ 3100).

the steep decline represents the eclipse of white dwarf and/or spot. Thus the flux provided by the white dwarf alone must not exceed the step height of $\sim 1.7 \times 10^{-17}\,\mathrm{erg\,s^{-1}\,cm^{-2}\,\AA^{-1}}$. With a mean white dwarf mass of $M_1 \sim 0.6\,M_\odot$ and a mean temperature of 16000 K (Sion 1999) the implied distance is d $\geq$ 550 pc, which is consistent with the distances derived in Sect. 3.2.2.

Assuming that the secondary fills its Roche-lobe and using the M-R relation from Knigge (2006) together with the orbital period we get a mass of the secondary of $M_2 \sim 0.09$ which is only weakly dependent on the mass ratio q. With an assumed white dwarf mass of $M_1 \sim 0.6$ this implies $q \sim 0.15$. The mass ratio, the orbital period and the eclipse width determine the orbital inlination. Since the white dwarf is not resolved in our data, we used the mean spot eclipse width of 325 s to compute a $q - i$ relation, which results in an inclination of $i \sim 83°$. Since the real white dwarf mass remains unknown, the derived inclination is just the approach of least prejudice, but hardly constrains the system geometry.

The X-ray bright phase is centered at phase 0.9 which gives the azimuth of the accretion spot of $\sim 36°$. The length of the X-ray bright phase is about 0.62 phase units locating the accretion spot on the hemisphere most oriented towards earth. Since the length of bright phase depends on inclination i and colatitude β of the accretion region we get a constraint on the colatitude. Neglecting any height of the accretion column the colatitude is $\beta \sim 20°$ for $i \sim 83°$ but correspondingly larger for a possible vertical or horizontal extent of the
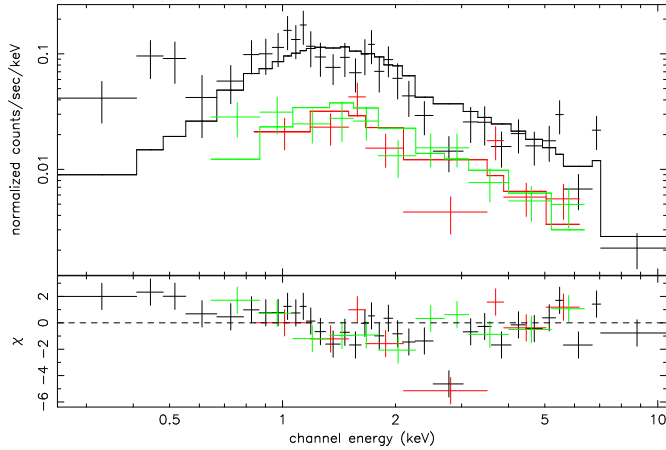
Figure 3.10: Spectral fit of the combined PN and MOS spectra for the phase intervals of the absorption dip (visually selected for each orbit) with an absorbed MEKAL model. Plasma temperature and normalization were fixed to the values of the fit to spectrum of the bright phase before the absorption dip.

emission region.

Both the optical and X-ray eclipse are preceded by a dip. This is also found in other polars and is caused by absorption of X-rays when the accretion stream passes the line of sight to the emitting accretion region (Watson et al. 1987, Schwope et al. 2001) as is required if $i > \beta$. In this case we expect to see a change in the hardness ratio since the photoelectric absorption cross-section is greater at lower energies. The hardness ratio together with the soft and hard X-ray light curve are displayed in Fig. 3.9. Interestingly the hardness ratio shows a monotonic increase from phase 0.75 until the beginning of eclipse. If this is just due to the photoelectric absorption the corresponding accretion stream has to be extended over a large range in azimuth and is more properly an accretion curtain than a well defined stream. This could also be an explanation for the non-detection of the soft component of re-processed origin. An extended accretion curtain leads to a bigger and thus lower temperature accretion region on account of the lower specific accretion rate. We searched for evidence of an extended accretion arc from the X-ray light curve at eclipse ingress and egress. Ingress and egress are shorter than 5 s and likely shorter than 3 s but the low number of counts does not allow to derive stringent limits. For comparison, in the otherwise similar system HU Aqr ROSAT-observed eclipse egress lasts 1.3 s (Schwope et al. 2001).

To test whether the dip is caused by absorption of cold material we tried to fit the X-ray spectrum of the phase intervals where the dip occurs, with plasma temperature and normalization fixed to the values of the fit to the spectrum of the bright phase before the absorption dip (see Sect. 3.4). Just the hydrogen column remains as a free parameter to ascertain whether the spectral change between bright phase and dip phase can be explained with additional absorption. We obtained a reasonable good fit with $\chi^2_\nu = 2.2$ and a $N_H = 0.41(4) \times 10^{22} \text{cm}^{-2}$ (see Fig. 3.10).

Assuming a high inclination as derived above, the center of the stream dip gives the azimuth of the threading region in the orbital plane. The X-ray dip is centered at phase ~ 0.9. This corresponds to an azimuth $\sim 54°$ of the threading region. The optical stream
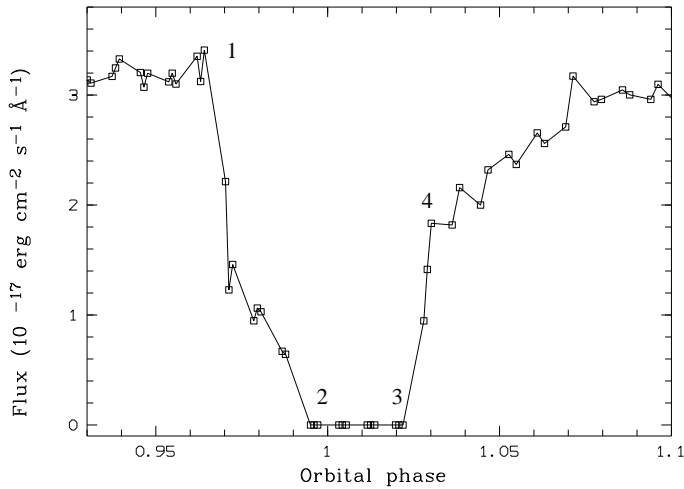
Figure 3.11:
Mean eclipse light curve from the optical R band observations on March 19 (errors are smaller than symbol size). Ingress and egress of accretion spot and accretion stream are clearly identifiable. The numbers indicate the begin of the white dwarf ingress (1), begin of complete eclipse (2), end of complete eclipse (3) and begin of the egress of the accretion stream (4). Figure 3.12 illustrates these phase intervals. Non-detections are set to zero.

dip is centered at phase $\sim$0.85, somewhat before the X-ray dip. The phase difference could either be due to a shifted spot location or a higher accretion rate compared to the X-ray observation and thus an accretion stream coupling later in the orbital plane to the magnetic field.

The center of the R band hump occurs at phase $\sim$0.62, 0.3 phase units before the center of X-ray bright phase. If we exclude a radical change in accretion geometry between the X-ray observation in 2004 and the optical observation in 2007, this can be explained by cyclotron beaming, meaning a cyclotron origin of the R band hump. With the spot location as derived above, the center of R band hump corresponds to the orbital phase where the spot just appears over the limb of the white dwarf. The optical hump starts at phase $\sim$0.35, in the X-ray faint phase, which lasts until phase $\sim$0.55. This suggests that the self-eclipse of the accretion column is complete only in X-rays but partial at optical wavelengths due to a high shock, so beamed cyclotron radiation is still seen, while the X-ray emitting region is hidden behind the white dwarf. The remaining puzzle is the missing second optical hump. With the explanation above, a second hump would be expected, when the spot disappears behind the limb of the white dwarf. The missing second hump implies a rather large angle between magnetic field vector and surface normal, which is hard to explain with a simple dipole geometry.

With the system parameters derived above, we modelled the extent of the accretion curtain for the given system and binary parameters and could reproduce the observed timings of the R band eclipse light curve (see Fig. 3.11) excellently. This is illustrated in Figure 3.12, which shows the corresponding phase intervals designated in Figure 3.11. The long ingress phase of the curtain is due to the extended ballistic accretion stream which has its largest extent at an azimuth of $\sim$60°.
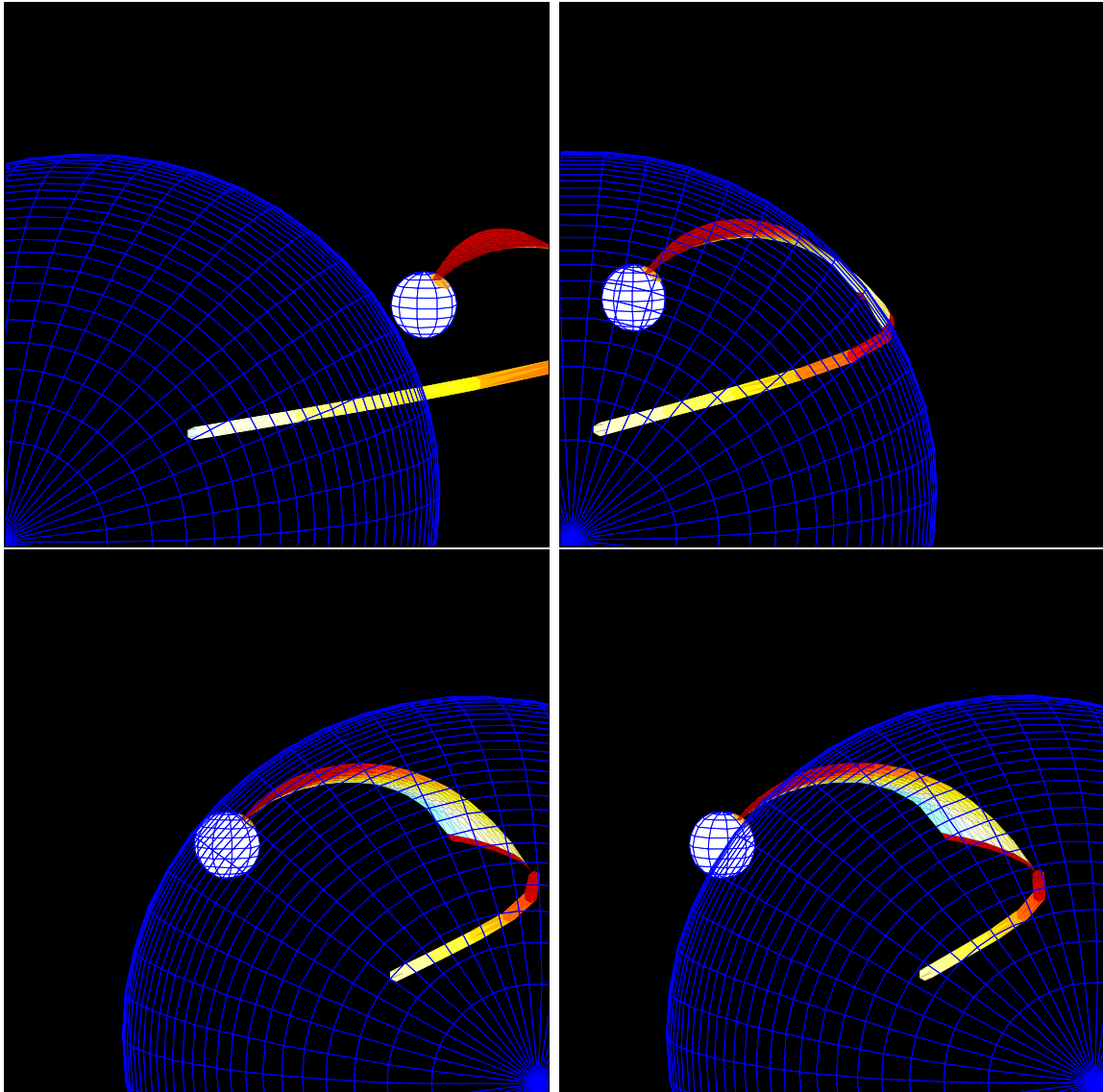
Figure 3.12:
Visualisation of 2XMM1312 with *curtain* (Vogel 2004) at eclipse phases (compare with Fig. 3.11) with the derived system parameters: mass of the white dwarf M_1=0.6, mass of the secondary M_2=0.09, inclination i = 83°, colatitude of dipole Θ_D = 20°, azimuth of dipole Ψ_D = 36°. *Upper left*: begin of white dwarf ingress at phase 0.965, corresponds to (1) in Figure 3.11. *Upper right*: begin of total eclipse at phase 0.995 (2). *Lower left*: end of total eclipse at phase 0.025 (3). *Lower right*: begin of accretion stream egress (4).
The extent of the accretion curtain was set to Ψ = 40° - 90°. Colours indicate projected velocities of the matter being accreted.

3.9 Summary

We have presented an analysis of the newly discovered eclipsing polar 2XMM1312. The polar shows a hard X-ray spectrum with a plasma temperature of ~ 14 keV, but no sign of a soft component. The soft component is probably shifted to the EUV due to an extended and thus cooler accretion region. The system has one active accretion spot on the hemisphere most oriented towards earth with an azimuth of $\sim 36°$ and a low colatitude. The period of the system could be determined with fairly high accuracy, the distance is likely to be ≥ 500 pc.

We could not directly determine the strength of the magnetic field but the large extent of the ballistic stream and the properties of the cyclotron radiation suggest a rather low field strength, $B \leq 10$ MG. We suggest that high-speed optical photometry with a large telescope be performed in order to test our prediction of a large extended accretion arc and to determine the brightness and colour of the secondary in eclipse.

We further suggest IR spectroscopy and polarimetry to directly determine the magnetic field strength. Finally, phase-resolved UV-photometry would help to determine the white dwarf's temperature and size of the accretion spot, allow to further disentangle radiation components and settle the question of the so far undetected component of reprocessed hard X-rays.

Chapter 4

The white dwarf modelling program DWARF

As already explained in Chapter 1 the photospheric temperature of the accreting white dwarf and the temperature of the accretion spot as well as the heated pole cap can aid substantially to understand the energy balance of the accretion process and the shape of the accretion column. I developed a mapping program, which allows – adequate observational data assumed – to derive a temperature distribution of the white dwarf surface from phasefolded light curves of polars. Therefore the white dwarf surface is subdivided into small surface elements, each element with a temperature assigned. Then the resulting flux from the whole white dwarf is computed for every orbital phase and compared with the observational data. Using an evolutionary algorithm the temperature of each element is changed until the computed model light curve fits the observational data. After a short introduction into indirect imaging methods the program will be introduced more detailed in the following sections.

4.1 Indirect imaging

The apparent size of cataclysmic variables is too small to be resolved by direct imaging. Thus all observable information from the six-dimensional phase space x, y, z, v_x, v_y, v_z of the system is projected onto fewer dimensions. To be more clearly consider a cataclysmic variable as an aggregation of point-like emission sources. These emission sources are located on the secondary, the white dwarf or in the accretion stream. Each of these emission sources has a certain velocity in the co-rotating reference frame and a certain intensity. In the case of photometry the measured flux is just the summed contribution of all emission sources at a given orbital phase. All information about the location inside the binary

system is lost[1]. In the case of spectroscopy the measured flux at a given wavelength is the summed contribution of all emission sources with the same projected velocity, regardless of the velocity inside the co-rotating reference frame. The information about the location and the information about the non-projected velocity is lost. To sum up, the projected information which can be obtained from the observations is deficient.

The question now is: *Is this projection reversible?*, i.e. is the lost information recoverable? As the Czech mathematician Johann Radon[2] showed already in 1917 (Radon 1917), such a projection can even be mathematically uniquely reversible under certain terms. This is called the Radon transform, where a function $f : \mathbb{R}^3 \longrightarrow \mathbb{R}$ can be reconstructed from the values in $\mathbb{R}$ if the integral along every straight line is known. This assumption is obviously violated for celestial objects, thus using the Radon transform – called backprojection in astrophysics – requires most of the times additional constraints. Another approach uses approximation methods, where the collapsed information is computed from theoretical non-collapsed models. The model is changed until it reproduces the collapsed information. Contrary to the Radon transform this approach never provides an unique solution, thus additional assumptions have to be made. A method frequently used in astrophysics is called Maximum-Entropy-Method (MEM). This can be nicely explained on the basis of DWARF. If two temperature maps of the white dwarf surface can reproduce the observed light curve equally well, then the map which is more smooth is also more likely, since sudden jumps in temperature (apart from the spot) on the white dwarf surface are physically implausible. The smoother map has a greater entropy and will be favoured by the fitting process – thus the term Maximum-Entropy-Method.

The most famous example for a tomographic method is certainly the Computer Tomography (CT) in medicine[3], where the human tissue is X-rayed. The attenuation of the X-rays corresponds to the integral over the mass density of the tissue in the direction of the beam and provides a two-dimensional projection of the three-dimensional tissue. X-raying the tissue from all directions, makes it possible to reconstruct its three-dimensional mass density.

Indirect imaging methods were introduced to astrophysics in the 80ies. Foremost the eclipse-mapping method, which allows to reconstruct the spatial information from time-resolved photometric observations (Horne 1985) and afterwards the Doppler-tomography (Marsh & Horne 1988) which uses time-resolved spectroscopy to reconstruct the velocity information. Today exist a wide variety of indirect imaging methods (see Boffin et al. 2001 for a comprehensive overview) for the mapping of accretion disks, the secondary and the accretion stream inside binaries as well as for the mapping of spots and magnetic topologies of single stars. It has to be clarified that for astrophysical tomographic methods, regardless of which inversion method is used, one has to provide a model of the binary system. For

---

[1]of course also all velocity information is lost, but this is inherent to photometry

[2]∗16.12.1887 Decin   † 25.5.1956 Wien

[3]G. N. Hounsfield and A. M. Cormack were awarded with the Nobel prize in 1979 for the development of the Computer Tomography

eclipse-mapping methods the surface onto which the observational data should be mapped has to be defined, which is not a serious drawback. In the case of Doppler-tomography a model which couples velocities to spatial positions has to be specified, which is – as in the case of the accretion stream – not always easy.

4.2 The problem

The accretion stream onto the white dwarf surface leads to a hot accretion spot and a larger but colder heated pole cap. The temperature and size of both components – if known – can help to understand and proof the energy budget. Another aspect concerns the shape of the spots, which allows to draw conclusion on the spatial orientation of the accretion column and thus the orientation of the local magnetic field.

Shape, size and temperature of the spot can – in principle – be derived from the shape of the phasefolded light curve, but since temperature and size scale against each other in the resulting flux it is not easy to derive both properties from the observational data. Simple geometric considerations make clear, that an eclipse of the white dwarf and the spot/pole cap by the secondary can give constraints on the size and thus the temperature. In sense of observational constraints, this is a short term event. The eclipse of the whole white dwarf is in the order of ~ 30 seconds (this value depends of course on the actual system parameters). The accretion spot covers a fraction in the order of 10^{-2} to 10^{-3} of the white dwarf surface, thus the eclipse of the spot is an event lasting less than a few seconds. This means that data with a high temporal resolution are needed for any unambiguous modelling of the white dwarf surface.

Another problem arises from the various emission sources inside the polar system. Most of the times the white dwarf and the pole cap are outshone by the much brighter accretion stream and cyclotron component. Thus just high-time resolution data are not sufficient, one also needs data from a low accretion epoch of the system and an optical band pass, where the observed light is dominated by the white dwarf, which is preferably the ultraviolet.

4.3 Modelling of the white dwarf surface

The surface of the white dwarf can be modelled in good approximation with a sphere. The common approach to divide the surface in unique elements is to use a graticule. This approach is widely used in mapping algorithms but has several disadvantages. First of all the single elements have either a similar size but a very different extent in longitude and latitude or they have a similar size in angular units but then the area will be very different. Therefore one has to find a compromise between differences in area and in angular extent,

which nevertheless does not eliminate a geometric preference. Secondly the elements at the pole caps are to be treated in a special way. Contrary to the other elements they have just three vertices. This is not only a problem when creating equally sized elements but also takes a lot of unnecessary effort while writing the numerical algorithms.

The solution for that problem is surprisingly old and goes back to Platons "Timaios". Besides their role for the harmony of nature, the therein mentioned five Platonic solids are convex regular polyhedrons with the characteristic that the faces, edges and angles are all congruent (there are in fact only these five geometric bodies with such properties). One of these solids is the Icosahedron (see Fig. 4.1). It consists of 20 triangles connected in such a way, that the polyhedron has 12 vertices, with every vertex having the same distance to its five neighbours. Putting an Icosahedron inside a globe the surface of the sphere can be approximated in the following way: Every edge connecting two vertices is subdivided at the centre. These points are now radially shifted onto the sphere and connected with the mid-points of the neighboring edges (see Fig. 4.2). Thus every triangle is subdivided into four new triangles. Beginning with an Ikosahedron with 20 elements the sphere is approximated in every step with a quadrupled number of elements. This creates a mesh of the white dwarf surface and is illustrated in Fig. 4.1. There is no geometric or angular preference, the elements are all nearly equally sized (the area of the smallest and the biggest element differ by a factor of ~ 1.2). The small disadvantage of this parametrisation is the non-continuous step size in the element size and number. The stepsize in number is always a factor of four. The number of elements is antipodal in resolution of the surface and fitting the data. A high number of elements gives a high spatial and thus temporal resolution, which is desired, but increases the number of free parameters, which is always a critical point for fitting data. This problem can be solved by a selective mesh refinement. Almost always the interesting regions of the white dwarf surface – meaning the rough location of the accretion spot and heated pole cap – are known in advance. Increasing the number of elements just in these regions, increases the resolution for the interesting surface regions, but keeps the number of free parameters as small as possible.

4.3.1 The radius of the white dwarf

To derive the system parameters of a polar, the stellar parameters are crucial. While the radius of both components can be identified relatively easy (the secondary is assumed to fill its Roche-lobe and the radius of the white dwarf can be determined from its eclipse length), the mass of the components is a lingering problem. Particularly the mass-radius relation of white dwarfs is a chronic problem. Although the stellar structure was already solved analytically seventy years ago (Chandrasekhar 1935a, Chandrasekhar 1935b, Chandrasekhar 1939), the used simplifications lead to imprecise parameter relations. Chandrasekhar used a zero-temperature star and the equation of state for a Fermi-Dirac gas of non-interacting electrons with a fixed value of the mean molecular weight μ. These assumptions are violated depending from the considered density regime. While at high densities in the inner
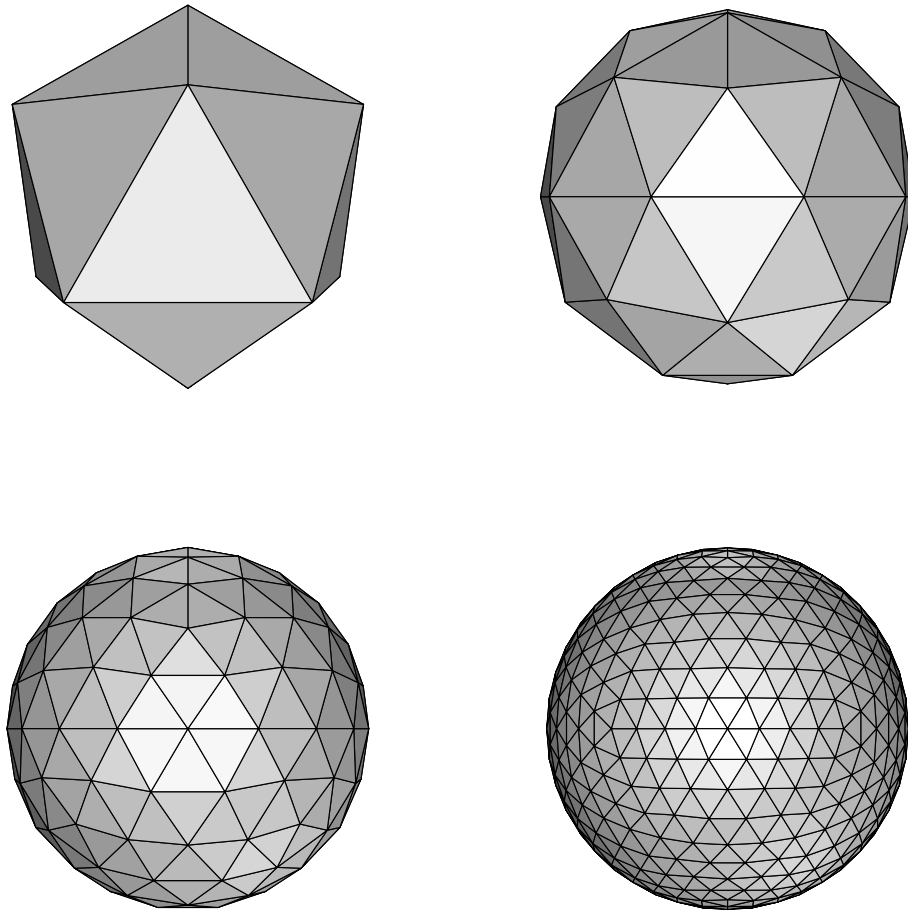
Figure 4.1:
The parametrisation of the white dwarf surface. Starting with a Icosahedron the number of surface elements is quadrupled with every step illustrated in Fig. 4.2.

core inverse beta decays change the value of μ, electrostatic interaction plays a role at low densities towards the outer shell. Both effects were included in the analytical solution by Hamada & Salpeter (1961). Later on more realistic conditions, including the influence of differential rotation were considered (Nauenberg 1972), but the remaining problem was still the assumption of a zero-temperature star. Since the influence of a non-zero temperature can be solved solely by numerical computation, it took another two decades to explore this influence (Koester & Schoenberner 1986, Wood 1995, Vennes et al. 1995, Panei et al. 2000). Figure 4.3 illustrates the different mass-radius relations for white dwarfs. As can be seen, the analytical solutions provide a sufficient approximation for low temperature white
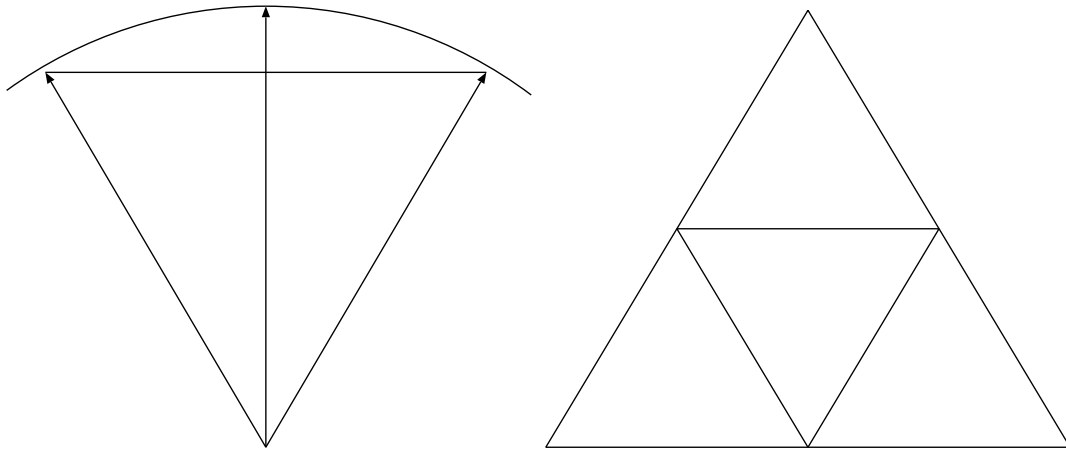
Figure 4.2:
Creating the white dwarf surface mesh. Each edge is intersected in the middle and the intersection point shifted radialy onto the white dwarf surface (left). Then each intersection point is connected with the intersection point of the neighboring edges (right), thus each triangle is divided into four new triangles (obviously the four new triangles do neither reside in the same plane as the original triangle nor do they share a common plane).

dwarfs but for higher temperatures the deviations of the radius from the zero-temperature model are appreciable. The mean temperature of the white dwarf in polars is ~ 16000 K (Sion 1999), thus the radius can be up to 10% larger than the appropriate radius of a zero-temperature white dwarf.

Another impact on the mass-radius relation, particularly important for white dwarfs in magnetic cataclysmic variables, results from the magnetic field of the star, leading – as the temperature – to an increase in radius for a given mass (Suh & Mathews 2000). In general the influence of the magnetic field is not well understood, already the conclusion from the surface field strength to the internal field strength of the core is not evident.

For the mapping program DWARF a pragmatic approach was chosen. The analytic solution by Nauenberg (1972) is provided with a correction factor for each individual system. This correction factor is derived from the comparison of Nauenberg with the more recent numerical calculation (see Fig. 4.3) for the given temperature. Obviously the approximate mean temperature of the white dwarf surface has to be determined in advance. How this can be done is described at the appropriate places in this work.
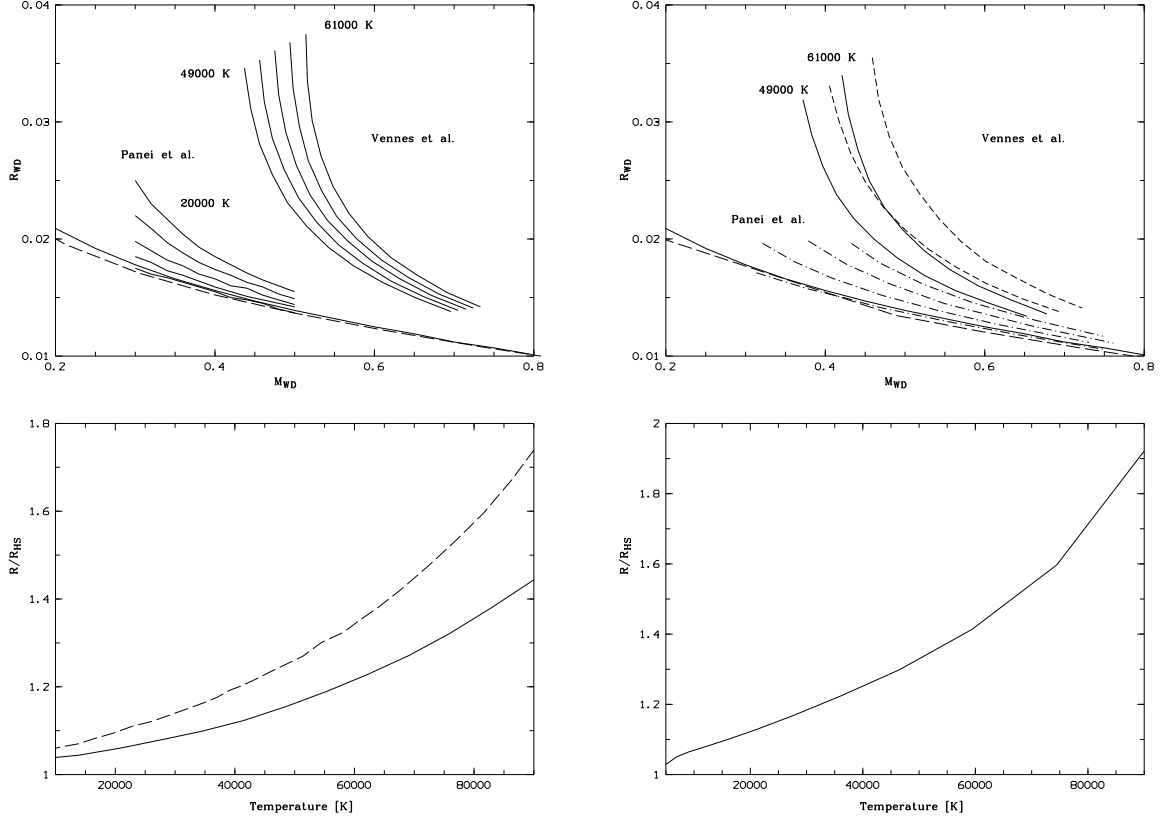
Figure 4.3:
Different analytical and numerical mass-radius relations for white dwarfs. *Upper left panel*:
Analytical solutions for helium white dwarfs from Nauenberg 1972 (lower solid line) and
Hamada & Salpeter 1961 (long dash) compared with numerical solutions from Panei et al.
2000 for temperatures from 4000 K to 20000 K in steps of 4000 K and from Vennes et al.
1995 for temperatures from 49000 K to 61000 K in steps of 3000 K. *Upper right panel*:
Analytical solutions for carbon white dwarfs from Nauenberg 1972 (lower solid line) and
Hamada & Salpeter 1961 (long dash) compared with numerical solutions from Panei et al.
2000 for temperatures from 5000 K to 35000 K in steps of 10000 K and from Vennes et al.
1995 for 49000 K and 61000 K. The short dashed lines indicate a carbon core white dwarf
model with a thick hydrogen envelope ($\log q = -4.0$). *Lower left panel*: Radius of a M_{WD}
= 0.598 $M_\odot$ white dwarf as a function of temperature (Koester & Schoenberner 1986) in
units of the radius according to Hamada & Salpeter 1961. The solid line indicates a pure
carbon core white dwarf with a helium envelope of $\sim$ 0.02 $M_\odot$, while the dashed line
indicate a white dwarf model with an additional amount of $10^{-4} M_\odot$ hydrogen in the outer
shell. *Lower right panel*: Same as in the lower left panel, but for the model of Wood 1995.

4.4 Modelling the binary system

Modelling only the white dwarf is not sufficient since it can be eclipsed by the secondary (in fact just these circumstance makes the mapping of the white dwarf surface meaningful). Thus the whole binary system has to be modelled. It is defined by the masses of both stars and the orbital period. Newton's law of gravitation together with Kepler's third law defines the distance of the center of masses:

$$a = \left[\frac{P_{orb}^2 G(M_1 + M_2)}{4\pi^2} \right]^{\frac{1}{3}} \tag{4.1}$$

The gravitational potential including the fictitious centrifugal force is defined by (Frank et al. 1985):

$$\Phi_R = -\frac{GM_1}{(x^2 + y^2 + z^2)^{\frac{1}{2}}} - \frac{GM_2}{([x-a]^2 + y^2 + z^2)^{\frac{1}{2}}} - \frac{1}{2}\Omega_{orb}^2([x - \mu a]^2 + y^2) \tag{4.2}$$

$$\text{whereas} \quad \mu = \frac{M_2}{(M_1 + M_2)} \quad \text{and} \quad \Omega_{orb} = \frac{2\pi}{P_{orb}} = \frac{G(M_1 + M_2)}{2\pi a^3}$$

In polars the secondary fills its Roche-lobe, thus the surface of the secondary is defined by the equipotential $\Phi_R = $ const. of the first Lagrangian point. There are two usual procedures to compute a possible eclipse of a point by the secondary. The first is to compute the gravitational potential along the line of sight from the point towards the observer. If the potential falls below the potential of the first Lagrangian point $\Phi(L1)$ after excessing it for the first time, the point is eclipsed, otherwise not. The second approach uses the projected shape (towards the observer) of the secondary. For DWARF the second approach was chosen, since it turned out to save computation time (see Sect. 4.7). The computation of the shape of the secondary is illustrated in Fig. 4.4. First the gravitational potential along the x-axis starting at the origin is computed. The maximum potential $\Phi(L1)$ is reached at the L1 point and defines the innermost point in x direction of the secondary. The outermost point of the secondary is obtained when the potential again reaches the value of the innermost point. The distance beetween both points is subdivided into points of distance x_m according to the desired resolution. Each of these points defines a {y,z} plane. Starting at the point {x,0,0} and chosing a direction in the {y,z} plane the potential is now computed until it reaches again the value $\Phi(L1)$ at the surface of the secondary. The angular resolution depends on the angular step size α. This gradually defines a grid on the secondary surface.

4.5 Computation of light curves

Once the surface of white dwarf and secondary are computed, the whole geometry of the system is defined. Now the resulting flux of the model has to be computed for every orbital
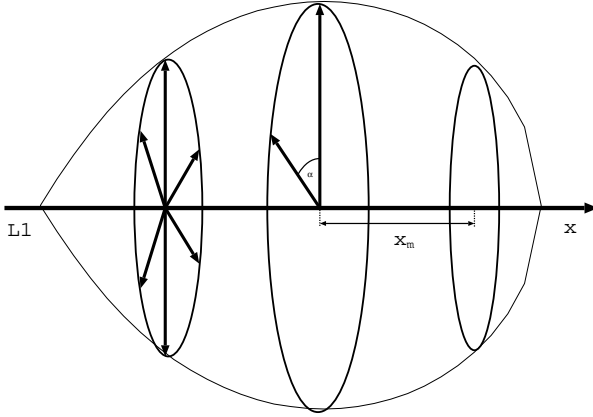
Figure 4.4:
The parametrisation of the secondary surface. The stepsize x_m along the x axis and the angular stepsize α determine the spatial resolution of the secondary surface.

phase. The phase resolution inside DWARF can be chosen individually for every phase interval, according to the significance of the interval. When the spot on the white dwarf is self-eclipsed the phase resolution of the model can be less than the observational time resolution, while for the eclipse ingress and egress of the spot the model phase resolution should be higher than the observational time resolution.

4.5.1   Coordinate transformation

To compute the projected area of each element and to check if the element is eclipsed by the secondary or self-eclipsed, i.e. located on the farther side of the white dwarf, the spatial coordinates of every point in the binary system have to be transformed for every phase step to the coordinates of the observers frame of reference. If T_{CV} defines the coordinates of the co-rotating frame of reference, T_O the cordinates of the observers fixed reference frame with the observer at the point $(\infty, 0, 0)$, Φ the orbital phase, and i the orbital inclination of the system, then both reference frames are correlated by

$$T_O = \underline{\underline{M}}^i \underline{\underline{M}}^\Phi T_{CV} \tag{4.3}$$

whereas the matrix $\underline{\underline{M}}^\Phi$ corresponds to the rotation around the z-axis, i.e. the phase angle

$$\underline{\underline{M}}^\Phi = \begin{pmatrix} \cos\left(\Phi\right) & \sin\left(\Phi\right) & 0 \\ -\sin\left(\Phi\right) & \cos\left(\Phi\right) & 0 \\ 0 & 0 & 1 \end{pmatrix} \tag{4.4}$$

and the matrix $\underline{\underline{M}}^i$ to the rotation around the y-axis, i.e. the inclination of the system

$$\underline{\underline{M}}^i = \begin{pmatrix} \sin(i) & 0 & -\cos(i) \\ 0 & 1 & 0 \\ \cos(i) & 0 & \sin(i) \end{pmatrix} \tag{4.5}$$

The normal vector $\vec{N}$ in the direction towards the observer in the T_{CV} reference frame is then defined by

$$\vec{N} = \begin{pmatrix} \cos(\Phi)\sin(i) \\ -\sin(\Phi)\sin(i) \\ \cos(i) \end{pmatrix} \tag{4.6}$$

The projected size of a element is then given by the element area multiplied with the cosine between $\vec{N}$ and the surface normal of the element, with the element being self-eclipsed when the projected size is negative.

4.5.2 Eclipse

For every surface element it has to be verified if it will be eclipsed by the secondary and in case it does, for which orbital phase interval. Since a white dwarf element can only be eclipsed when the secondary is in front of the white dwarf in the observers frame of reference the x_O coordinate can be collapsed and the problem is now simply a two dimensional intersection problem. The x-collapsed secondary can be described by a convex polygon, which can be easily computed from the secondary surface points by using the Graham scan algorithm[4], which finds the convex hull of a two dimensional point set. If a x-collapsed surface element of the white dwarf is inside this convex hull, it is eclipsed. As a simplification it is assumed that the whole surface element is eclipsed, if the focal point of the element is eclipsed. This requires a sufficient spatial resolution of the white dwarf surface to avoid mapping effects like aliasing.

4.5.3 White dwarf model spectra

Finally for every surface element with a given temperature a flux contribution has to be computed. It was and surprisingly is still not unusual to approximate the spectrum of a white dwarf with a simple black body of the same temperature. A simple comparison of black body and white dwarf model spectra is shown in Fig. 4.5 and demonstrates that this is not acceptable in general and an oversimplification. Depending on temperature

---

[4]named after Ronald Graham, who developed this algorithm in 1972

Filter	Wavelength [Å]	Conversion factor [erg cm^{-2} s^{-1}]
V	5430	2.50 $\times 10^{-16}$
B	4500	1.32 $\times 10^{-16}$
U	3440	1.96 $\times 10^{-16}$
UVW1	2910	4.70 $\times 10^{-16}$
UVM2	2310	21.2 $\times 10^{-16}$
UVW2	2120	56.7 $\times 10^{-16}$

Table 4.1: Overview of the available XMM OM filter. The conversion factor gives the corresponding flux for a count rate of 1 s^{-1}. Due to a time-dependent decrease in sensitivity, the actual value depends from the epoch of observation.

and wavelength the difference between the flux provided by the white dwarf and the flux provided by a black body can be quite large. While for cold white dwarfs with temperatures below ~ 6000 K and for wavelengths above 5000 Å a black body can be used as a good approximation for a white dwarf, the opposite is true for higher temperatures and wavelengths in the ultraviolet.

A nice example can be found in Szkody et al. 2006. The authors tried to model optical, near-UV and far-UV light curves obtained with the space telescope GALEX of the polar EF Eri with a white dwarf model with uniform temperature distribution and a hotter spot on the surface of the white dwarf. Both components were simulated with black bodies. They used different sizes and temperature gradients for the spot as well as different limb darkening coefficients, but were finally not able to reproduce the optical and far-UV variations in the light curves simultaneously. Thus they came to the conclusion that these variations cannot be explained by any spot model and that a "puzzling source of ultraviolet light" remains.

Using white dwarf model spectra (Koester et al. 2005 and references therein) instead of black bodies and a simple two-parameter model (size and temperature of the spot) we could model the variations in the three bands simultaneously with a white dwarf of temperature ~ 10000 K and a spot of 18500 K with a half opening angle of 24° (Schwope et al. 2007), eliminating the need for a "puzzling source".

4.5.4   Using the XMM optical monitor

Using just the final flux calibrated observed light curve for comparison with the model flux at a given wavelength neglects any spectral information within the observed band pass. Therefore wherever possible, wavelength-dependent detector- and filter-specific responses should be used to compute the resulting flux from the used model atmospheres. In the composite spectra of cataclysmic variables the white dwarf can be best seen in the blue or ultraviolet wavelength range. One of the used instruments in this work is the XMM optical monitor (see section A.2). Therefore the use of detector- and filter-specific responses is exemplarily described for the case of XMM-OM observations (see Table 4.1 for the filter specifications): For a given spectrum the resulting count rate cr of the XMM-OM detector
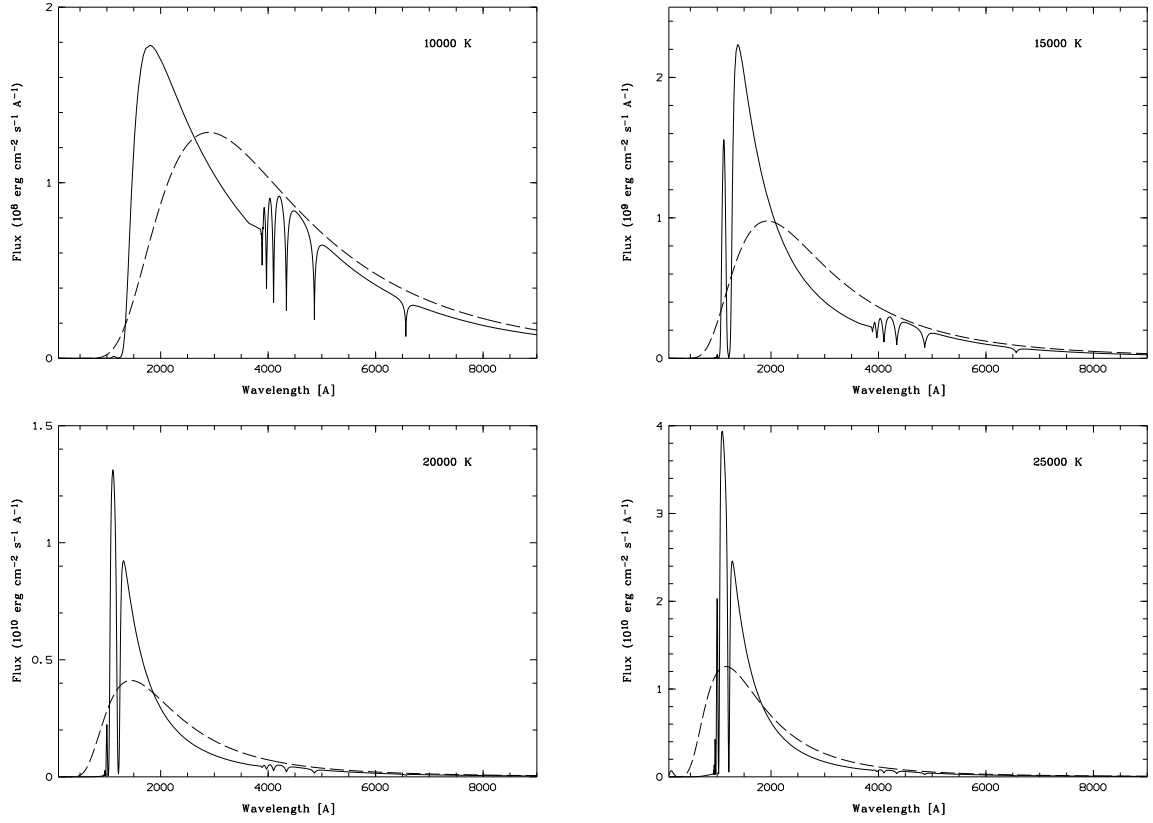
Figure 4.5:

Comparison of non-magnetic white dwarf model spectra (from Boris Gänsicke) with black body spectra for different temperatures

is computed in the following way:

$$cr = A \cdot S(t) \cdot \int_{\lambda_{min}}^{\lambda_{max}} F(\lambda)O(\lambda)R(\lambda)T(\lambda)C(\lambda)\eta(\lambda)\frac{\lambda}{hc}d\lambda \quad [s^{-1}] \tag{4.7}$$

where A is the entrance area of the telescope, $F(\lambda)$ denotes the flux of the model atmosphere, $R(\lambda)$ the reflectance of the detector system composed out of the reflectance of the primary and secondary mirror and the reflectance of the dichroic, $T(\lambda)$ the transmission of the filter and detector window, $O(\lambda)$ the open area ratio of the micro-channel plate, $\eta(\lambda)$ the quantum efficiency of the photocathode, and $C(\lambda)$ the ratio between the expected count rate and the experimentally measured pre-launch count rate.

After years in orbit, it turned out that the sensitivity of the OM detector decreased continuously with time. The actual decrease is determined with periodical observations of celestial sources used for in-orbit calibration. This time dependent sensitivity function is described by $S(t)$.
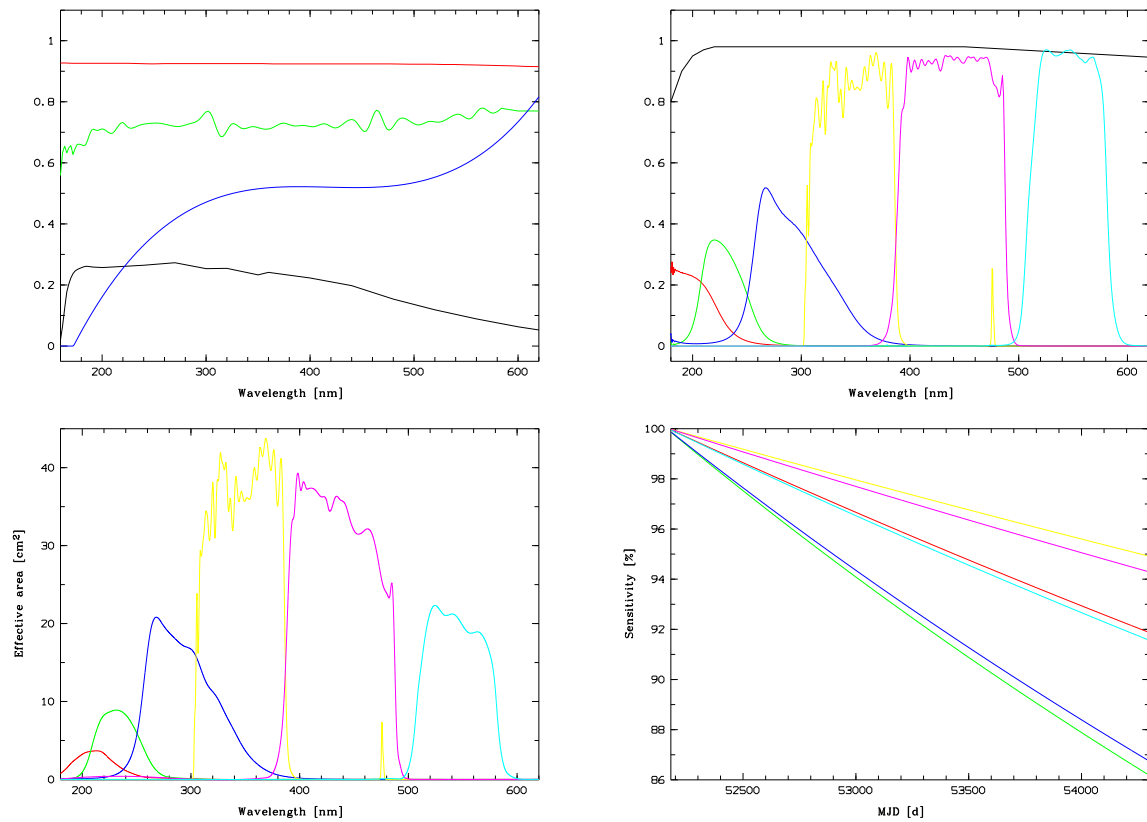
Figure 4.6:
Response curves for the XMM-OM detector. *Upper left:* The quantum efficiency of the photocathode (black), the reflectance of the aluminum-coated mirrors (red), the open area ratio of the micro-channel plate (green), the ratio between the expected count rate and the experimentally measured pre-launch count rate (blue). *Upper right:* Transmission of the detector window (black), the UVW2 filter (red), the UVM2 filter (green), the UVW1 filter (UVW1), the U filter (yellow), the B filter (magenta) and the V filter (cyan). *Lower left:* Combined responses taking into account the entrance area of the telescope (color coding as in the upper right plot). *Lower right:* Sensitivity degradation of the detector in the different filters from October 2001 until July 2007 (color coding as before).

Fig. 4.6 shows the individual response curves for the OM and the time-dependent sensitivity degradation. Thus the model spectra are first multiplied with the individual response curves and then the resulting spectrum is integrated, keeping the information of the spectral energy distribution, and compared with the observed count rate at a given moment.

4.5.5   Computing the light curves

The following explains the computation of the final light curve for the case of XMM OM observations. For other instruments the procedure is similar, but does not necessarily involve all of the steps.

After the parametrisation of the binary system it is known for every surface element of the white dwarf and for every phase step, if the element is visible at all, if it is eclipsed by the secondary and its projected size. If the spectral library gives the Eddington flux (per unit area) of the white dwarf for a given temperature, then the measured count rate can be computed as follows. First the model spectrum is folded through the response curve of the detector, converted to counts and integrated over the covered wavelength range of the instrument. This gives the effective count rate $C_{\text{eff}}(T)$ per unit area as a function of the temperature. Since the spectral library provides just a grid of white dwarf model atmospheres for different temperatures but it should be possible to assign each surface element an arbitrary temperature, $C_{\text{eff}}(T)$ is fitted by a polynomial interpolation leading to a continuous $C_{\text{eff}}(T)$ function. Then the measured count rate for a given temperature map of the white dwarf can be computed for every phase step by multiplying $C_{\text{eff}}(T)$ with the projected size of each visible element of the surface and the scaling factor for the distance of the white dwarf and adding up all elements.

4.6   Inversion method

Computing a light curve from a given temperature map of the white dwarf is straight forward but the reverse is not, as explained in the introduction about indirect imaging. Starting with an arbitrary temperature map this map has to be modified until the observed light curve is reproduced. This is a classical optimisation problem, where inside a given search-space the global optimum has to be found. There are several methods to find an optimum. For DWARF an evolutionary algorithm was chosen. Evolutionary algorithms are non-deterministic and offer a greater chance to find the global optimum and not to get stuck in a local optimum, which is a problem of most of the deterministic approaches. The only prerequisite for a evolutionary algorithm is an evaluation function, which judge the current solution. The following section introduces shortly evolutionary algorithms and describes the used evaluation function. For an in-depth introduction to evolutionary algorithms see Weicker (2007).

4.6.1   Evolution

Evolutionary algorithms imitate the biological evolution. The parameters which are to be fitted can be considered as genes, the entire set of parameters as genotype. In nature the genotype is changed either due to randomly arising mutations or due to recombination,

i.e. the mixing of different sets of genes. The therewith changed phenotype is exposed to the environment, leading to a selection and the "survival of the fittest". The surviving individuals constitute a population. After a certain number of generations, a population comprehending a phenotype ideally adapted to the environment is formed. This procedure can also be applied to technical optimization problems for finding the "fittest" solution.

For the DWARF program the temperature T_j of a single surface element j can be considered as a single gene, the whole temperature map M as the genotype. The environment for which the phenotype, i.e. the model light curve, has to be optimized is described by the observed light curve. Similar to nature a set of individual temperature maps $M^{(i)}$ forms a population $P = \{M^{(i)}\}_{1 \le i \le \lambda}$, where λ denotes the number of individuals that belong to a population. The individuals of the population can be subjected to mutation and recombination. From the new temperature maps (the children in biological context) the resulting light curve can be computed and compared to the observed light curve. Temperature maps which reproduce the observed light curve better than others will be selected and form a new parent generation. The cycle starts again, until an adequate solution is found.

Mutation   A small alteration of the genotype can cause a change in phenotype. If this change in phenotype leads to a higher fitness of an individual, the individual has a selection advantage compared to the other individuals. Thus the changed genotype will spread in subsequent generations. In evolutionary algorithms mutation is simulated by copying a full parameter set (in biological context the parent individual) and performing small changes on randomly selected parameters. This leads to a new parameter set (the child individual in biological context):

$$M_{\lambda,j}^{(i)} = M_{\mu,j}^{(i)} + \delta^{(i)} \tau_j \qquad\qquad j \in \{1...n\} \qquad\qquad (4.8)$$

where μ denotes the parent and λ the child. The random numbers τ_j will be multiplied with the step size $\delta^{(i)}$ and have a normal distribution with the density function:

$$\phi(x) = \frac{1}{\sigma\sqrt{2\pi}} e^{-\frac{1}{2\sigma^2}x^2} \quad \text{with} \ \ \sigma = \frac{1}{\sqrt{n}} \qquad\qquad (4.9)$$

The course of evolution depends on the inheritance of parental qualities, thus the mutations should be small. The expectation value of $\phi(x)$ is zero, meaning that small changes have a higher probability. As in nature the success of a mutation depends on the already reached degree of adaption to the environment. For a low conformity of the individuals to the environment, i.e. a bad fit, large mutations can have a high success rate, whereas for a high conformity small mutations will have a higher success rate. In algorithms this can be realized with a scaling factor for the stepsize:

$$\delta_{\lambda}^{(i)} = \delta_{\mu}\xi^{(i)} \qquad \text{with} \ \ \xi^{(i)} = \alpha_1 \ \ \text{or} \ \ \xi^{(i)} = \frac{1}{\alpha_2} \qquad\qquad (4.10)$$

The free parameters $\alpha_{1/2}$ should be slightly greater than one and have to be provided before starting the evolution. If $\xi^{(i)}(\alpha_1)$ or $\xi^{(i)}(\alpha_2)$ is used for scaling, is randomly chosen

during the fitting process. This guarantees that the stepsize is automatically adapted to the current "fitness" of a population. Low conformity will favour a large stepsize, while a high conformity will favour small stepsizes.

Recombination In nature recombination developed as an antagonist to perfection. While the copying of genes was getting better and better, the chance of creating new phenotypes due to mutations decreased in the same order. To compensate for the reduced probability of creating new phenotypes, the method of combining the genotypes of two parent individuals to obtain a new child genotype developed. In evolutionary algorithms different kinds of recombination exists. DWARF uses the so-called dominant recombination, where the genes, i.e the temperatures of a single surface element, of a new child individual are randomly selected from one of the parent individuals. Contrary to nature the number ρ of parents is not fixed to two, but can be arbitrary.

Selection In nature selection has different aspects. There is a selection due to the different adaption of the individuals to the environment. In the case of sexual reproduction there is an additional selection due to the choice of one out of many possible sexual partners (parent selection). In DWARF the parent individuals are selected randomly, so there is no parent selection. For choosing the parent individuals for the next generation, there exist two strategies. The so-called plus strategy: $(\mu/\rho + \lambda)$ selects the parents of the new generations out of the children and the parents (in this case the grandparents of the new generation) of the current generation, while the so-called comma strategy $(\mu/\rho, \lambda)$ uses just the children of the current generation. Both strategies are implemented in DWARF.

While mutation and recombination increases the diversity of the genotype inside a population, selection acts as a opponent, decreasing the diversity. The balance of all three mechanisms is essential for solving a given optimization problem. The best suited mutation, recombination and selection parameters are not known in advance and have to found for each problem separately.

4.6.2   Evaluation function and entropy

The main features of evolutionary fitting algorithms should be clear with the description of the previous subsection. Solutions of an optimisation problem correspond to individuals in biology. Analogous to nature the possible solutions have to undergo an evolution to find the best suited one. The remaining point is the referee of the evolution, who has to judge about the goodness of a certain solution.

The first step simply compares the resulting light curve of a given temperature map with the observed light curve via the χ^2 statistics:

$$\chi^2 = \sum_k \frac{(F_{data,k} - F_{comp,k})^2}{\sigma^2{}_k} \tag{4.11}$$

The challenge arises from the fact, that the problem is non-deterministic. As explained in the introduction a huge amount of equally suited solutions are possible. One has to find the most probable solution.

One usual approach in astrophysical tomography is the use of a so-called entropy map. Therefor the entropy of the parameter map is compared with a so-called default map. The idea behind is, that a smoother map (with a higher entropy) is physically more likely than a grainy map. The smoothness depends of course on the given physical context. E.g. for the mapping of an accretion disk it would be more natural to use a radially symmetric default map than to use a globally levelled one. To compute the entropy, i.e. the smoothness of a map, the current solution will be compared with a smooth map. Maps deviating less from the default entropy map will be favoured as possible solution.

For the mapping of spots, as done in DWARF, the adequate entropy map is not known in advance. A simple global entropy map can smear out the spot, hiding the interesting details. Also a radially symmetric entropy map is not the perfect solution, since the shape of the accretion spot is probably not ringlike but more arcuate, due to the structure of the magnetic field, which guides the infalling matter. Also the shape of the heated pole cap has not to be circular.

DWARF offers several approaches for the best-suited entropy map.

Sliding global default map The sliding global entropy map M_D uses the mean temperature of all surface elements of the current map. The default map is absolutely flat, each element having the temperature:

$$T_{D,m} = \sum_{j=1}^{n} \frac{T_j}{n} \qquad m \in \{1...n\} \tag{4.12}$$

where j iterates over the number of elements n of the map. This approach is the most unbiased entropy map, but as mentioned above has also the highest risk to hide details.

Fixed global default map The fixed global entropy map is similar to the sliding global default map, but uses a fixed temperature value for the entropy map. The reason for that is, that the white dwarf will have a uniform temperature distribution. Just the region of the accretion spot and pole cap will have a higher temperature. In many cases the mean temperature of the white dwarf is known in advance and can be used instead of sliding mean of the current temperatures.

Nearest neighbor entropy map The global default maps mentioned above have the disadvantage of possibly suppressing small scale structures. This can be attenuated by using small scale default maps. The small scale default map used for DWARF favours a

high entropy in local neighborhoods:

$$T_{D,m} = \frac{1}{p+1}\left(\left(\sum_{j=1}^{p} T_j\right) + T_m\right) \qquad m \in \{1...n\} \qquad (4.13)$$

where p is the number of neighbors.

Circular entropy map The circular default map favours a circular spot shape. For given coordinates the surface element nearest to these coordinates is found. Then all elements enclosing this central element are combined to a ring-like structure, called a "level". The elements encircling this level constitute the next level and so on. There can be set also an upper limit of levels, but does not have to. The default map is created from the mean temperature of all elements not belonging to one of the levels and from the mean temperature of each level.

$$T_{D,m_O}^{O} = \sum_{j=1}^{n_O} \frac{T_j}{n_O} \quad m_O \in \{1...n_O\} \qquad (4.14)$$

$$T_{D,m_L}^{L} = \sum_{j=1}^{n_L} \frac{T_j}{n_L} \quad m_L \in \{1...n_L\}, L \in \{1...\} \qquad (4.15)$$

$$(4.16)$$

where the subscript O denotes elements not belonging to a level and the subscript L the elements belonging to a certain level.

When comparing the current map with the default map the entropy has to be computed somehow. In literature different entropy definitions can be found. The finally used entropy calculation is from Dhillon & Watson (2001):

$$S = \sum_{j=1}^{n} T_j - T_{D,j} - T_j \; ln(\frac{T_j}{T_{D,j}}) \qquad j \in \{1...n\} \qquad (4.17)$$

where T_j denotes the actual temperature of a element and $T_{D,j}$ the temperature of the corresponding element in the default map.

Finally χ^2 statistics and entropy have to be combined to make up the evaluation function. The importance of the entropy will change during the fit. First of all a sufficient degree of correlation between the resulting light curve and the observed light curve has to be reached before the entropy comes into play. This can be reached with a weighted evaluation function Γ:

$$\Gamma = \frac{\chi^2}{n} - \frac{g}{(\chi_f^2 - \chi^2)} \; S \qquad (4.18)$$

where χ_f^2 denotes the achievable χ^2 without any provision for the entropy and n the number of surface elements. χ_f^2 has to be computed with an initial fitting run. The parameter g

is a weight for the importance of the entropy and has to be determined empirically for each problem. In sum, the second term of equation 4.18 gives the complete influence of the entropy on the fit. While g determines the overall importance of the entropy, the denominator assures that the influence of the entropy increases with decreasing χ^2.

A problem for mapping algorithms like DWARF is always the number of free parameters. Fortunately the interesting regions of the white dwarf can be predefined to a high degree. E.g. the orbital phase where the eclipse of the spot occurs together with the orbital phase of the maximum flux gives a good estimate of azimuth and colatitude of the spot. Thus it is often not necesseary to fit the whole white dwarf surface. This is taken into account in DWARF. It is possible – and often advised – to define arbitrary regions of the white dwarf surface which will be fitted. All elements outside this regions will be held on a constant temperature and disregarded for the fitting process.

4.7   Implementation

DWARF was implemented in C. For expandability and maintainability the complexity of the problem was put into the used data structures, to keep the algorithms as simpel as possible. Every surface element is represented by a data structure containing all ever needed properties of this specific element. The individual data structures are nodes of a doubly-circularly-linked list, thus all algorithms can iterate over just the needed properties of all elements. This design makes it also very easy to use selective or adaptive mesh refinement when necessary. The nodes of the sub-elements are merely latched into the list, thus the algorithms do not have to take care about the actually used refinement.

The evolutionary algorithms were implemented using an adapted version of the *evoC* library, developed by K. Trint and U. Utrecht at the Technische Universität Berlin. This library provides the necessary algorithms for mutation, recombination and selection. To match the requirements of DWARF the data structures used in this library had to be changed accordingly.

4.7.1   Activity cycle

All configuration of the program is done inside a simple ASCII file. When the program starts it reads this configuration file setting all necessary parameter for the fitting run. Then the observed light curve(s), the response files for the detector of the used instrument and the spectral library is read. After the polynomial interpolation of the final spectral libray (see Subsect. 4.5.5), the complete system geometry is computed and the white dwarf surface initialized. For every given phase step for any given surface element the projected size and a possible eclipse and self-eclipse is computed. The status of every element for all phase steps is saved inside the node of the element, since this status will

not change during the fitting process and therefore must be computed only once. The orbital phase resolution can be chosen freely for individual phase intervals. This makes it possible to save computation time in uninteresting phase intervals, i.e. when the spot is self-eclipsed, and to increase accuracy for the important phase intervals during eclipse ingress and egress. Finally the temperature map is initialized and the evolution is started. For every temperature map the resulting light curve and the corresponding default entropy map is calculated and compared to the observed light curve. The best solutions are kept and constitute a generation, used as the starting point for the next generations. This is repeated until a sufficient solution is found.

4.7.2 Visualisation

The final temperature map can be visualized by a twodimensional projection for any given orbital phase and inclination. Although it is not necessary to have a three dimensional visualisation of the white dwarf or the whole binary system, it is often very valuable, helping to understand the shape of light curves. The visualisation and manipulation of three dimensional geometric objects is a standard problem in computation. Therefore it was a matter of rationality to use one of the available tools. For DWARF the *geomview*[5] program was chosen, since it can be controlled online by external programs through a special command language and provide several OOGL[6] file formats, most of them being plain ASCII. *geomview* was developed at the Geometry Center of the University of Minnesota. Taking into account the special requirements of binary stars, *geomview* was extended by an interface which allows to control orbital phase and inclination and provides the possibility of animations. Thus, besides the two dimensional temperature maps of the white dwarf surface, DWARF creates OOGL files which can be used to visualise the binary system.

4.8   Testing the reliability

The best fitting routine is worthless if it does not do the job or does not harmonise with the data used as input. This section provides the inevitable test calculations to demonstrate the ability of the program and the confidence level to which the results can be trusted. First of all the correct computation of the observable flux has to be proven. This is shown in the following section for the case of the XMM optical monitor.

---

[5]http://www.geomview.org/
[6]OOGL stands for *Object Oriented Graphics Library*

White dwarf	Temperature[1] [10^3K]	M_{WD}^1 [$M_\odot$]	XMM obs ID	Used temperature [10^3 K]	Distance[2] [pc]
HZ4	14 - 15	0.6-0.75	0155560101	14	38.8
GD50	33 - 50	0.58-1.4	0155560201	40	76.6
GD153	37 - 43	0.5-1.0	0125911101	40	55.8

[1] for references see the white dwarf database at http://procyon.lpl.arizona.edu/WD/
[2] for an assumed white dwarf mass of $M_{WD} = 0.6$

Table 4.2: The XMM observations together with the system parameters for white dwarfs used to test the DWARF program.

4.8.1 Computation of OM count rates

To test if DWARF can reproduce observed count rates of the XMM optical monitor, several white dwarfs were selected, which are both observed by XMM, as well as spectroscopically by HST/STIS[7], and have more or less accurately known system parameters. The appropriate white dwarfs are summarized in Table 4.2. First the model spectra were calibrated to the flux level of the STIS spectra. Since the temperatures of these white dwarfs are not known precisely the temperatures of the model atmospheres were fixed to a reasonable value. Also the white dwarf mass was fixed to a reasonable value of $M_{WD} = 0.6 M_\odot$ for all three white dwarfs. This mass gives immediately a resultant white dwarf radius and a (not necessarily true) distance. These parameters were than used as an input for DWARF.
The XMM observations were re-reduced using the XMM data reduction software SAS 6.5[8]. Using the response curves for the XMM optical monitor the resulting count rates were computed using DWARF and compared to the observed count rates. This is summarized in Figure 4.7. The XMM OM count rates are reproduced sufficient well by DWARF, taking into account the not well known system parameters and the calibration uncertainties of two different instruments.

4.8.2 Testing the inversion process

The correct computation of the observable flux is just a prerequisite. Another and more important point is the reliability of the inversion process. Therefor it is crucial to test the ability of the program to reproduce artificial test maps. Especially in the case of evolutionary algorithms this is a proliferating work. This section will present only a few test cases.

The general approach is to create artificial temperature maps, compute the resulting light curves in different bands and use these light curves as input for DWARF. The pro-

---

[7]see A.3
[8]as of 2005, when this was done, the newest release
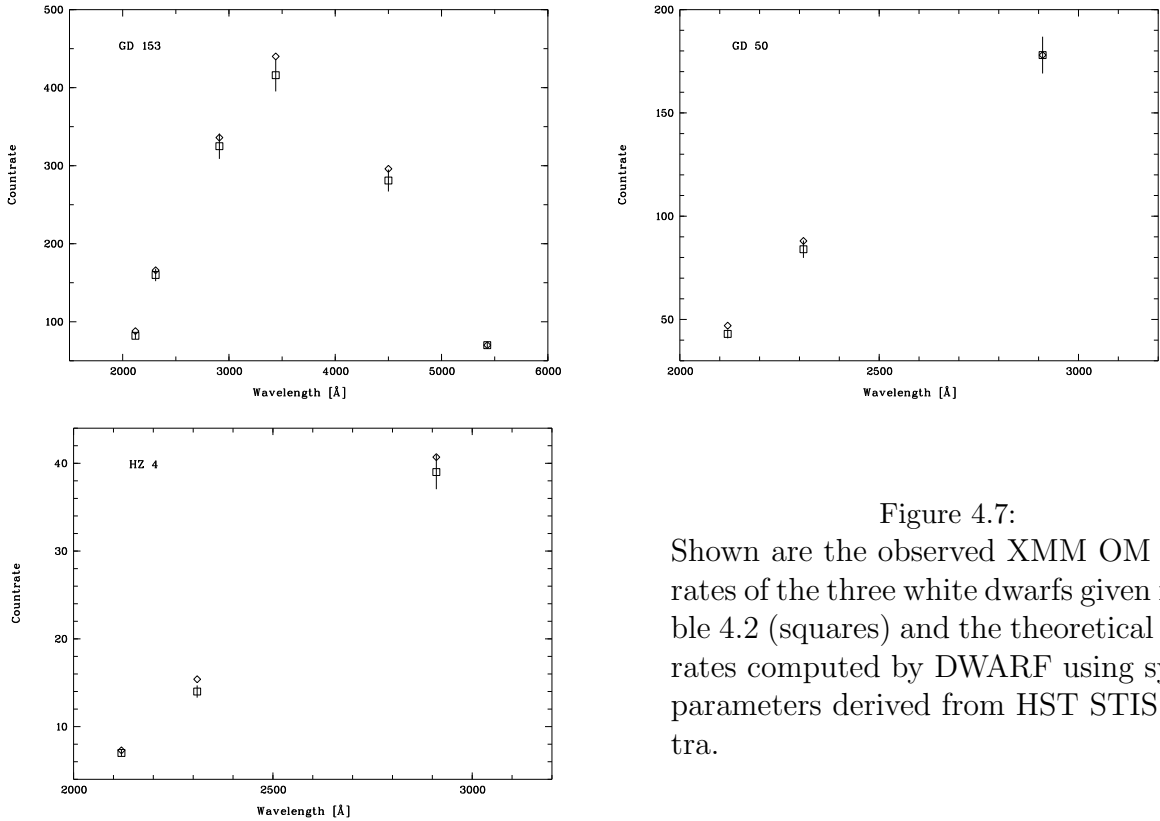
Figure 4.7:
Shown are the observed XMM OM count rates of the three white dwarfs given in Table 4.2 (squares) and the theoretical count rates computed by DWARF using system parameters derived from HST STIS spectra.

gram should then be able to reproduce the temperature maps.

Since the shape of the spots on the white dwarf surface is not known in advance, the program should be tested with a variety of spot shapes. But for high inclinations as in eclipsing systems, every spot can be decomposed into its longitudinal and latitudinal components. While the former are more perpendicular to the eclipsing limb of the secondary and are eclipsed gradually, the latter are more parallel to the eclipsing limb and are eclipsed in a shorter time interval. Or in other words, the latitudinal extended components leave a faster alteration in the eclipse light curve. Therefore two test maps were created. One with a longitudinal extended spot - or better stripe - and one with a latitudinally extended stripe. Each stripe is composed of two streaks with a temperature of 45000 K and 60000 K. The remaining surface of the white dwarf has a temperature of 15000 K. The test maps are shown in Fig. 4.8 and 4.9. The system parameters are chosen arbitrarily and can be found in Table 4.3. Two bands were defined, one covering the range 1500.0 - 2200.0 Å (for the following band 'A'), and a second covering the range 3500.0 - 5000.0 Å (for the following band 'B'). The time resolution of the synthetic light curves is 0.5 seconds for the approximate orbital phase intervals of eclipse ingress (0.960 - 0.972) and egress (0.028 - 0.04) and is reduced to 3 seconds for the out-of-eclipse phases. The region to be fitted onto the white dwarf surface was restricted to an azimuth of $0° \leq \Psi \leq 90°$ and a colatitude of $0° \leq \beta \leq 90°$ for all fitting runs. The restriction in azimuth is not a constraint and

Orbital period	[s]	5500
M_{WD}	[$M_\odot$]	0.6
M_2	[$M_\odot$]	0.2
Mass ratio		0.33
Inclination	[°]	80
Distance	[pc]	100
T_{WD}	[K]	15000
T_{Spot}	[K]	45000
		60000

Table 4.3: The used system parameters to create the synthetical DWARF light curves from the temperature maps shown in Fig. 4.8 and 4.9. The values are chosen arbitrarily.

i = 70.0   Φ = 0.875   i = 0.0   Φ = 0.0

10000   Temperature [K]   80000

Figure 4.8:
Test map for DWARF. The longitudinal extended stripe is composed of elements with a temperature of 45000 and 60000 K, the remaining temperature for the white dwarf surface is 15000 K. The longitudinal extent is $20° \leq \Psi \leq 55°$, the latitudinal extent $55° \leq \beta \leq 65°$. Step size of the graticule is 20°.

just saves computation time, the restriction in colatitude is necessary, since the symmetry of northern and southern hemisphere of the white dwarf leads to aliasing. This can be explained best for a system with an inclination of 90°, where this effect is strongest. Here every element of the white dwarf surface located on the northern hemisphere at (Ψ, β) has a counterpart on the southern hemisphere at $(\Psi, 180° - \beta)$, producing exactly the same orbital light curve. The visibility and the times of eclipse are the same for both elements. Hence, for a fitting algorithm these elements are indistinguishable. Nevertheless, the restriction in colatitude is not a serious constraint, since in general the hemisphere of the accretion spot can be determined fairly well from the observational data.

The first test is obviously the test of the evolutionary fitting procedure in general, without using any entropy. Therefor the synthetic noise- and error-free light curves created from the artificial temperature maps were used as input for DWARF. Due to the restriction in azimuth on the northern hemisphere - or to avoid anthropocentrism - the hemisphere most oriented towards earth, the evolutionary fitting procedure should reproduce the input

i = 70.0 Φ = 0.875   i = 0.0   Φ = 0.0
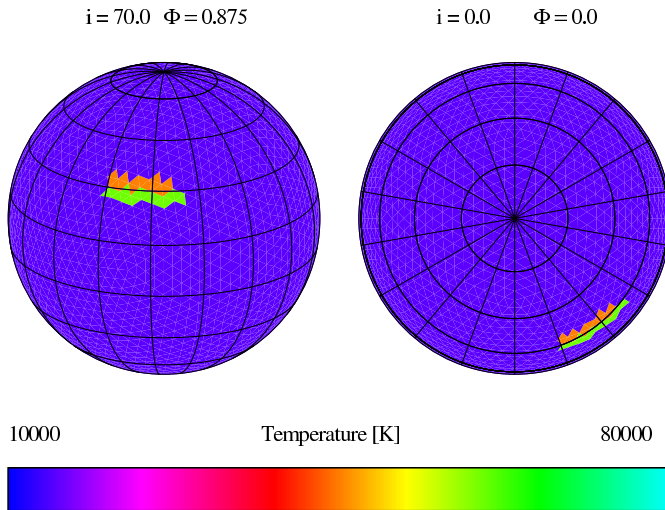
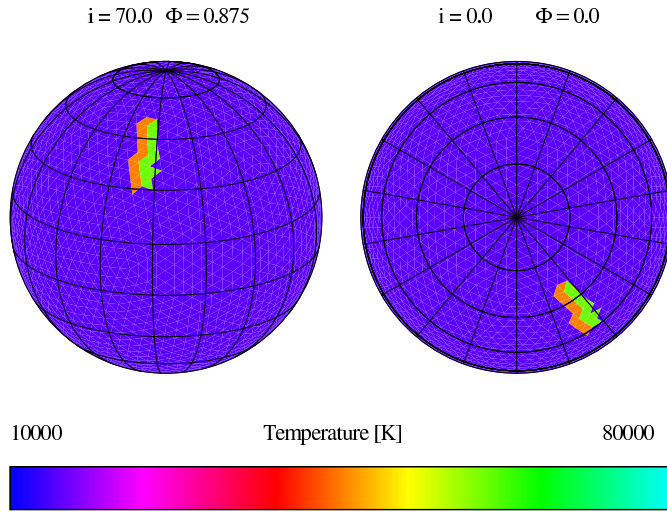10000   Temperature [K]   80000

Figure 4.9:
Test map for DWARF. The latitudinal extended stripe is composed of elements with a temperature of 45000 and 60000 K, the remaining temperature for the white dwarf surface is 15000 K. The longitudinal extent is $28° \leq \Psi \leq 40°$, the latitudinal extent $30° \leq \beta \leq 60°$. Step size of the graticule is $20°$.

temperature map sufficiently well. Note that - contrary to the explanation in Sect. 4.6.2 - a nearly unique solution in this case (with limited resolution of the white dwarf surface) is possible, since the data are artificial and thus noisefree and without errors. The results after one hundred thousand generations of a (5/2,50) strategy are shown examplarily for the case of the latitudinal extended stripe in Fig. 4.10. While the temperature distribution within the two streaks is not as uniform as in the input map - a clear consequence of the missing entropy - the mean temperature for each of the two streaks as well as for the remaining white dwarf surface is reliably reproduced with 44500 K, 60000 K and 15000 K. For the longitudinal extended stripe the results are just as well, but the evolution process was much slower, taking nearly the twice number of generations to reach the same quality. The possible reason is the higher number of elements, which are eclipsed during the duration of eclipse ingress for the longitudinal extended structure. The latitudinal extended structure leaves a shorter kink in the eclipse ingress light curve, compared to the longitudinal extended structure, and thus constrains the location of the structure to a smaller region on the white dwarf.

Since noise-free data are an ideal but not a matter of fact, now added gaussian noise to the synthetic light curves with a constant SNR = 20. The noisy light curves were then fitted using the same system parameters as for computing the light curves, a (5/2,50) evolutionary strategy and the 'nearest neighbor' entropy. The data points during eclipse ingress and egress were weighted higher than the data points outside eclipse. The entropy was weighted in a way, that the substructures were not smeared out to much. The results are shown in Fig. 4.11 for the longitudinal stripe and in Fig. 4.12 for the latitudinal stripe. Compared to the original temperature map, the recreated temperature map shows a more non-uniform temperature distribution for each of the two streaks. Also the sharp edges of the stripes are not conserved strictly. This is a direct consequence of the used 'neighbor' entropy, which forces a low temperature difference between adjacent elements. Using the region covered by the original streaks, the mean temperature is 44600 and 59600
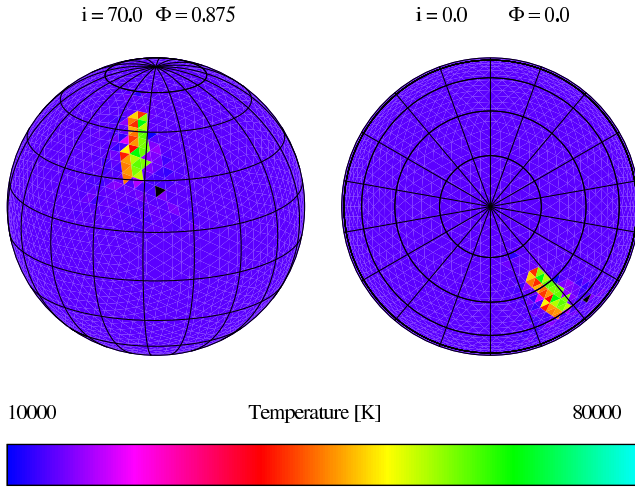
i = 70.0   Φ = 0.875   i = 0.0   Φ = 0.0

10000   Temperature [K]   80000

Figure 4.10:
Resulting temperature map for the latitudinal extended stripe, when using noisefree synthetic input light curves and an evolutionary fitting procedure without entropy map. The fitting region was restricted to an azimuth of $0° \leq \Psi \leq 90°$ and a colatitude of $0° \leq \beta \leq 90°$, the system parameters for the fit were the same as for computing the input light curve. Black elements denote temperatures below 10000 K.

for the latitudinal stripe and 43200 K and 60300 K for the longitudinal stripe. Taking adjacent elements with a significanter higher temperature than the white dwarf surface temperature (15000 K) into account, the mean temperatures are 41300 K and 49400 K for the latitudinal stripe and 37800 K and 60300 K for the longitudinal stripe. Thus the fitting process restores the correct temperature remarkably well, while the small-scale details of the shape of the spot are smeared out. A fitting run with a higher weighted 'neighbor' entropy resulted in an even more blurred stripe, while a fitting run with a less weighted entropy resulted in a more patchy temperature map.

Not only the observational data are limited in quality, also the accuracy of the system parameters is limited. Consequently the next step involves different system parameters for creating the light curves to be fitted and for the fitting process. Since the system parameters are correlated with the eclipse timings, they have to be changed consistently. For example an increase of the white dwarf mass, while the mass of the secondary, the orbital period and the inclination remain constant, would result in a shorter eclipse length (since the mass ratio decreases) as well as in a shorter ingress and egress (since the white dwarf radius decreases). A more detailed explanation about the relation between the system parameters and the eclipse timings is given in Sect. 5.3. As a consequence no meaningful temperature map will be obtained, but the improper system parameters can be recognized immediately on the basis of the mismatching orbital phases for the eclipse timings of 'observed' and fitted light curve. Therefore the eclipse width (383 seconds) and the duration of white dwarf egress and ingress (52 seconds) were determined from the synthetic light curves and the corresponding $q - i - M_{\mathrm{WD}}$ relation computed. For the fitting run the inclination was then changed from 80° to 83° and the mass of the components was adapted according to the derived relation. The resulting parameters are summarized in Table 4.4. Since the white dwarf is less massive for an increased inclination, it is getting bigger and thus the emitting area increases. To conserve the flux level during faint phase, i.e. the temperature of the white dwarf for the surface regions not being fitted, the distance

Figure 4.11:
Results for the longitudinal extended stripe. Gaussian noise (SNR = 20) was added to the synthetic input light curve, the system parameters for the fit were the same as for computing the input light curve. *Top*: input light curve (dots) and fitting result (line) for band 'A'. *Middle*: the same for band 'B'. *Bottom*: resulting temperature map (black elements denote temperatures below 10000 K).
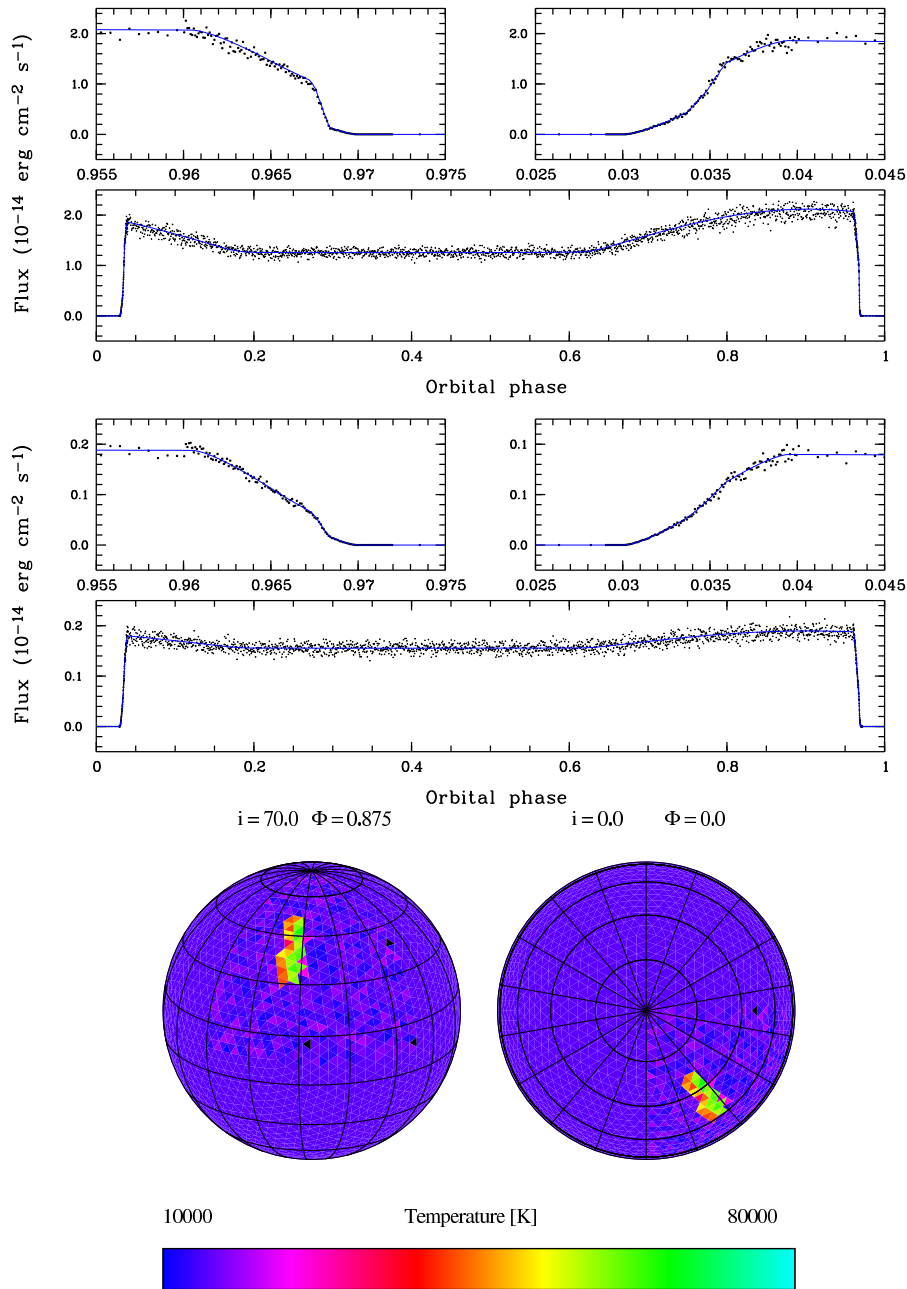
Figure 4.12:
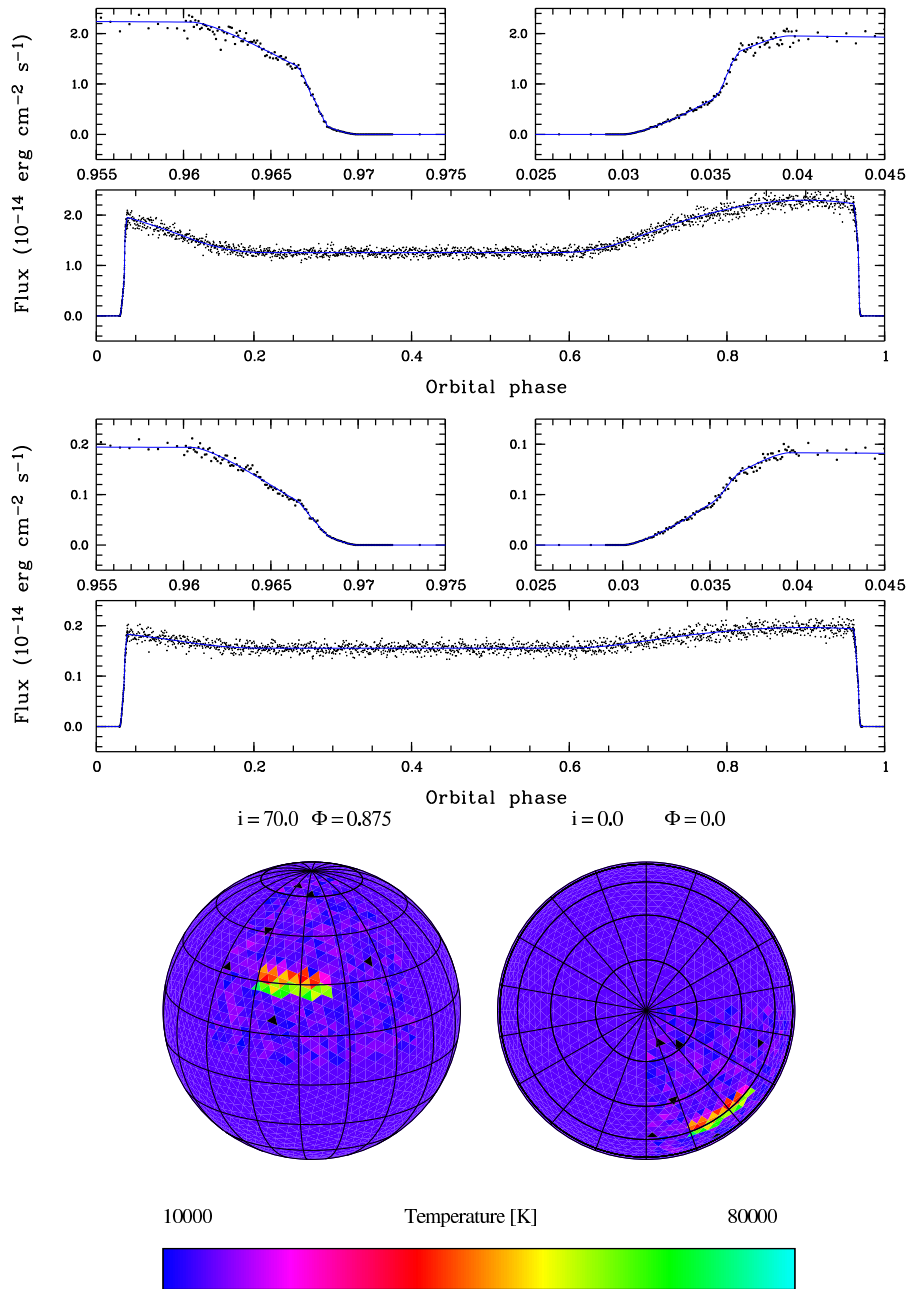Results for the latitudinal extended stripe. Gaussian noise (SNR = 20) was added to the synthetic input light curve, the system parameters for the fit were the same as for computing the input light curve. *Top*: input light curve (dots) and fitting result (line) for band 'A'. *Middle*: the same for band 'B'. *Bottom*: resulting temperature map (black elements denote temperatures below 10000 K).

Orbital period	[s]	5500
M_{WD}	$[M_\odot]$	0.535
M_2	$[M_\odot]$	0.119
Mass ratio		0.223
Inclination	[°]	83
Distance	[pc]	107.22

Table 4.4: The changed system parameters for the test system, which result from an inclination of 83° instead of 80° and constant eclipse timings of 383 seconds for the eclipse width and 52 seconds for the duration of white dwarf eclipse ingress and egress.

was also adapted accordingly.

The results are shown in Fig. 4.13 and 4.14. Again the data points for the eclipse ingress and egress were heigher weighted than the data points outside eclipse and the entropy was weighted in an adequate manner. For the longitudinal extended stripe the two distinct streaks are merged into one spot. Compared to the input map, the spot is compressed in longitude and stretched in latitude. The center of the spot is shifted by $\sim 5°$ towards a lower colatitude and lower azimuth. The mean temperature of 36000 K of the spot is considerably lower than in the original temperature map (53000 K), but the spot size is nearly doubled. A conspicuous feature of the temperature map is the cool region (marked in black in Fig. 4.14) at low colatitude and azimuth, with a temperature well below the mean surface temperature of 15000K.
For the latitudinal extended stripe the results are similar. The distinct temperature regions are not resolved anymore. Again the spot size is considerably greater than in the input map, resulting in a mean temperature of 36500 K. Contrary to the longitudinal extended stripe the spot is stretched in longitude, while the latitudinal extent remains constant compared with the input map. Just the center of spot is shifted by $\sim 5°$ towards a lower colatitude. Again the temperature map shows extensive regions with significantly lower temperatures than the mean surface temperature (marked in black 4.13).

The change in spot size as well as the cool regions can be explained with the changed system parameters. While the relative eclipse timings remain constant, the higher inclination leads to a changed orientation of the limb of the secondary in respect to the white dwarf. At lower inclinations the secondary causes a more grazing eclipse of the white dwarf, obscuring regions at high colatitude sooner than regions at low colatitudes. For higher inclinations the limb of the secondary is 'steeper', the colatitude on the white dwarf becomes less important. This fact explains the small shift of the spot locations as well as the change in extent of the spots. To become eclipsed at the same orbital phase as in the input light curve the location of the spot is shifted, to obtain the same length of ingress and egress of the spot, the extent in azimuth is reduced for the longitudinal stripe and the extent in colatitude is increased for the latitudinal stripe. The important boundary condition which prevents a large shift in azimuth for the whole spot, which would be the simplest solution, is the constant center of bright phase of the white dwarf light curve. It

depends only from the latitudinal location of the spot on the white dwarf, the changed system parameters do not account in this respect.

Besides the eclipse timings also the flux level has to be conserved. This is the reason for the cool spots on the white dwarf surface. Although, in the context of an accreting white dwarf, these cool regions are non-physically, they can be used as a tracer while adapting the system parameters.

The previously presented fitting runs are just a small selection from a plenty of possible verifications, but demonstrate already the general significance of the obtained temperature maps. DWARF can reliably reproduce the temperature maps used as input. For the case of improper system parameters the spot shape, size and temperature is naturally not strictly conserved. This is an intrinsic problem if the geometry of the system is used, but the presented test runs exhibit a clear feature of the program also found in other test runs. If unsuitable system parameters are used, the derived temperature maps show cool regions with temperatures significantly below the mean surface temperature of the white dwarf. With increasing entropy these regions vanish but mostly at the cost of non-fitting eclipse ingress and egress. In general cool regions on the white dwarf surface are a clear indicator for faulty system parameters.

The test runs - and the application of DWARF to data of the white dwarf in HU Aquarii, presented in the next chapter, also showed a clear limitation of the program. For large and relatively cool spots (compared to the mean surface temperature of the white dwarf), the eclipse ingress and egress show no clear signature of the spot. But the features of the eclipse light curve turned out to be crucial for the fitting process. They set hard constraints on the size and location of the spot. Without these constraints the properties of the spot depends mostly on the chosen entropy and are subjected to arbitrary settings of the fitting process. Nevertheless this is not a serious drawback, since these cases can be treated with simpler models (as in the case of HU Aquarii), which in turn are improper for light curves showing complex eclipse profiles.
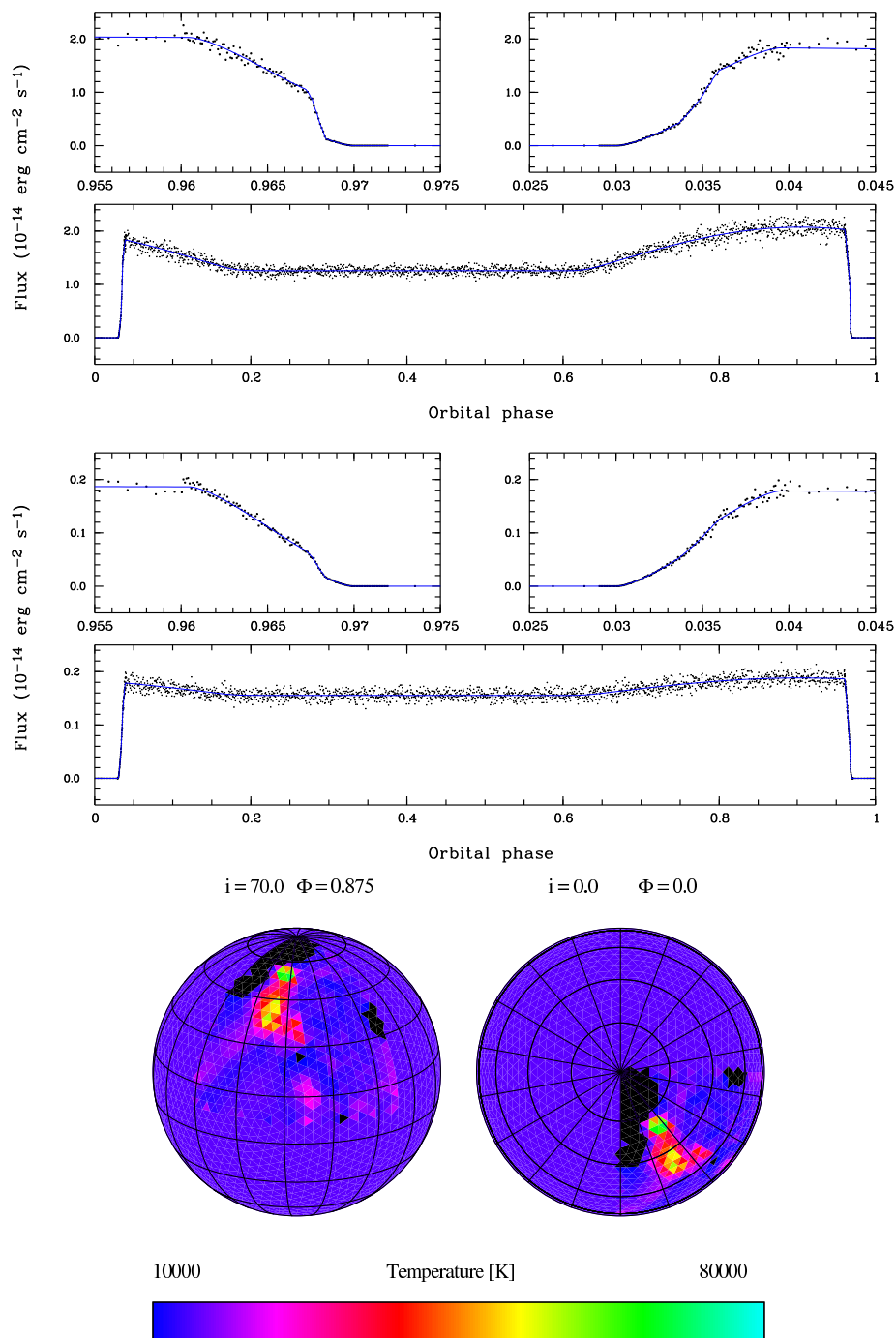
Figure 4.13:
Results for the latitudinal extended stripe. Gaussian noise (SNR = 20) was added to the synthetic input light curve, the system parameters for the fit were changed according to Table 4.4. *Top*: input light curve (dots) and fitting result (line) for band 'A'. *Middle*: the same for band 'B'. *Bottom*: resulting temperature map (black elements denote temperatures below 10000 K).
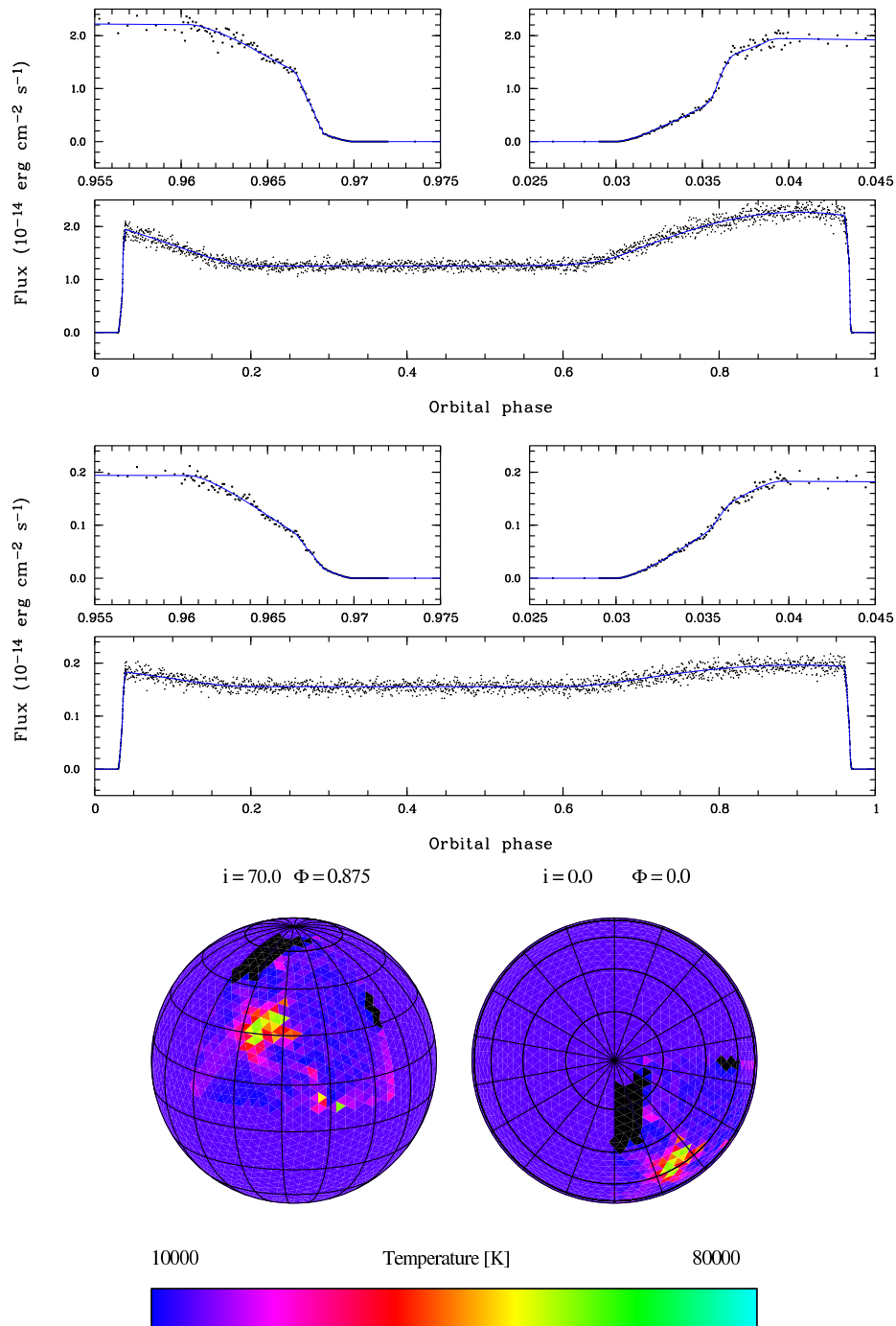
Figure 4.14:
Results for the longitudinal extended stripe. Gaussian noise (SNR = 20) was added to the synthetic input light curve, the system parameters for the fit were changed according to Table 4.4. *Top*: input light curve (dots) and fitting result (line) for band 'A'. *Middle*: the same for band 'B'. *Bottom*: resulting temperature map (black elements denote temperatures below 10000 K).

Chapter 5

The polar HU Aquarii

5.1 Introduction

HU Aquarii is a text-book example of a polar. Although several aspects are still obscured, it is one of the best understood polars among all known so far. It was detected independently as the source RXJ2107.9-0518 in ROSAT PSPC data (Schwope et al. 1993) and the WFC EUV data (Hakala et al. 1993). HU Aquarii was the first eclipsing polar discovered in the ROSAT All Sky Survey and attracted immediate interest. In the following years the system was intensively studied in all wavelength ranges (Glenn et al. 1994, Schwope et al. 1997, Schwope et al. 2001, Bridge et al. 2002, Howell et al. 2002). Since the discovery in 1992 HU Aquarii showed a different state of accretion in nearly all observations, which makes it an ideal target for many of the open questions about polars, but on the other

Figure 5.1:
Finding chart for HU Aquarii (position RA, Dec (2000) = $21\mathrm{h}07\mathrm{m}58.29\mathrm{s}, -05d17'39\overset{s}{.}4$) and the comparison used for the ULTRACAM observation in 2005.
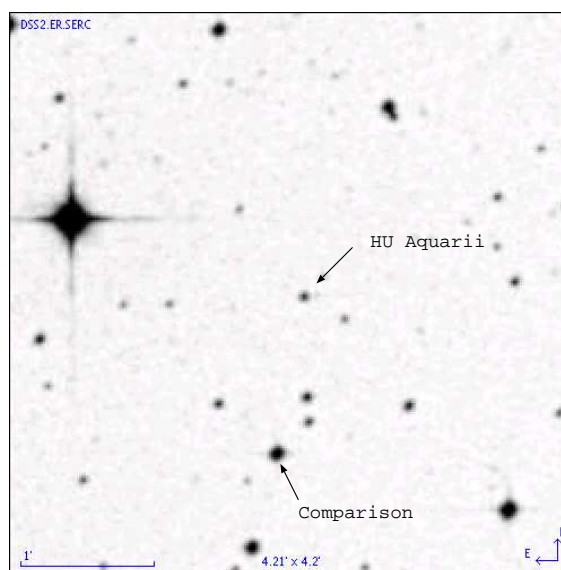
Parameter		Derived value	References
Mass ratio q		0.18-0.4	2,4
Mass of WD	[$M_\odot$]	0.61-0.95	1,2,8
Mass of secondary	[$M_\odot$]	0.15-0.3	1,2
Spectral type		M4-M6	1,2,5
Inclination	[°]	80-87	2,4,6,8
T_{WD}	[K]	<13000-20000	2,5
d	[pc]	111-245	1,2,3,5
B	[MG]	34-37	1,2,7

References:
[1]Schwope et al. (1993), [2]Glenn et al. (1994), [3]Sproats et al. (1996), [4]Schwope et al. (1997),[5]Ciardi et al. (1998),[6]Schwope et al. (2001), [7]Schwope et al. (2003),[8]Watson et al. (2003),

Table 5.1:
Overview of the derived system parameters for HU Aqr. This compilation lists all derived parameters available from the literature, regardless of the confidence of the values. For a more accurate overview see text. Only system parameters which do not depend on the accretion state are mentioned.

hand makes it even harder to snatch all the details from the system, since the current state of accretion for a new observation is unpredictable, making it hard to replicate an observation for a comparable accretion state. Several attempts were made to map the accretion stream (Hakala 1995, Schwope et al. 1997, Heerlein et al. 1999, Harrop-Allin et al. 1999, Vrielmann & Schwope 2001, Harrop-Allin et al. 2001, Schwope et al. 2003, Vogel 2004) or the secondary in HU Aquarii (Watson et al. 2003). The current knowledge about HU Aquarii can be summarized as follows.
HU Aquarii consists of a secondary of spectral type M4 to M4.5 (Schwope et al. 1993, Glenn et al. 1994), which agrees with the orbital period - spectral type relation from Knigge (2006). The mass of the white dwarf is very uncertain and covers a range from $M_{\mathrm{WD}} = 0.61\ M_\odot$ (Watson et al. 2003) to $M_{\mathrm{WD}} = 0.9\ M_\odot$ (Glenn et al. 1994). HU Aquarii exhibits a one-pole accretion szenario with a field strength of 34 MG (Schwope et al. 2003). The location of the threading region and the accretion spot on the white dwarf are correlated with the mass accretion rate (Harrop-Allin et al. 1999, Schwope et al. 2001). For high states the spot reaches it's largest azimuthal location at $\Psi \sim 46°$ (Vrielmann & Schwope 2001, Schwope et al. 2001, Bridge et al. 2002) and the systems shows an extended accretion curtain (Schwope et al. 1995). The mass ratio is likely to be ~ 0.25 and the inclination 85-86 °. Table 5.1 summarizes several system parameters derived during the last 15 years.
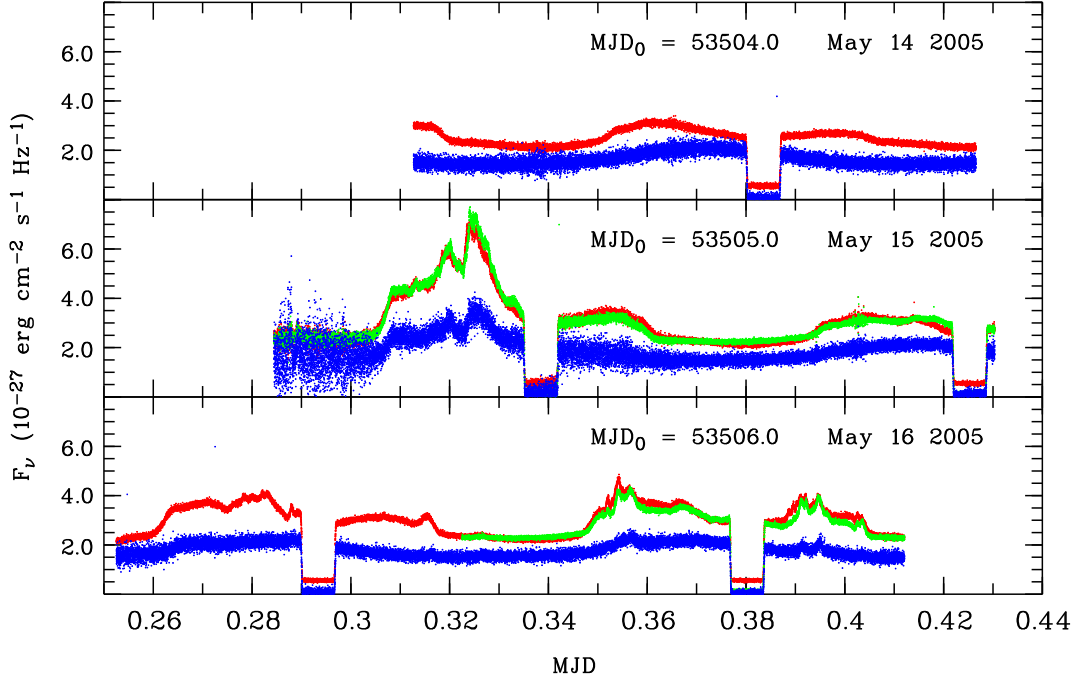
Figure 5.2:
ULTRACAM light curves of HU Aquarii in u(blue), g (green) and r (red) in original time sequence obtained in May 14 - 17, 2005. The data from May 17 are not shown here, since just the eclipse was observed.

5.2 ULTRACAM observations

HU Aquarii was observed with the high-speed photometer ULTRACAM[1] mounted to the Very Large Telescope at the Paranal Observatory, Chile in May 14 - 17, 2005. The observations were performed in Sloan u,g,r filters simultaneously with a time resolution of 0.5 seconds. The data were reduced in the usual manner for differential photometry. The comparison star is marked in Fig. 5.1, the resulting light curves are shown in Fig. 5.2 (for a zoomed-in eclipse light curve see Fig. 5.3). The observed light curves nicely demonstrate a low state of accretion. The u band light curve shows just a smooth sinusoidal variation, caused by the heated pole cap of white dwarf, while the r band light curve from the first night shows a smooth double-humped modulation caused by the beamed cyclotron emission from the residual accretion. The following nights show some additional flickering

---

[1]see A.4

in the r and g band, revealing accretion activity, while the u band is nearly unaffected. The eclipse (see Fig. 5.3) shows no sign of an accretion stream (compare with the stream ingress in Fig. 5.4 marked with 'B') and just discloses the eclipse of the pure white dwarf in u, superimposed by the cyclotron component in r.

Particularly for magnetic cataclysmic variables each observation shows a different composition of the individual emission components and is appropriate to analyze the properties of the dominant emission source. While observations taken during a high state of accretion are especially suited for studying e.g. the accretion process, high-time resolution observations during a low state of accretion make it feasible to study the white dwarf and obtain precise timings to determine the system parameters.

The ULTRACAM data – together with HST, OPTIMA and contemporary XMM OM observations on May 16, 2005 – were analyzed with respect to the white dwarf.

5.3 A re-determination of the system parameters

Depending on the inclination of a binary system, the eclipse width uniquely determines the mass ratio q of the system (the eclipse width is the time between eclipse ingress and egress of the center of mass of the white dwarf). The times of start and end of the eclipse ingress and egress of the white dwarf uniquely determine the radius of the white dwarf. In both cases the radius of the eclipsing component has to be known. Since the eclipsing secondary star in CVs is assumed to be Roche-lobe filling, no mass-radius relation is required. Instead the radius of the secondary is replaced by the projected shape of the Roche-lobe for a given mass ratio q. Eclipse ingress and egress of the white dwarf are events lasting less than a minute and in the case of cataclysmic variables the white dwarf is most of the times outshone by the accretion stream, making it difficult to identify these specific times in the observational data.

Both problems, insufficient time resolution and contamination of the light curve by the accretion stream are non-existent in the ULTRACAM data. The observed low accretion state and the high time resolution offered the great chance to (re)determine the system parameters with high accuracy.

We tested different methods to determine the times of white dwarf ingress and egress (*contact points* for brevity) from the five eclipses in u, g and r to get the most precise timings. A commonly used approach for non-magnetic CVs is described in Wood et al. (1985). In short, this method uses the derivative of the eclipse light curve to determine the mid-eclipse and contact points. While this method can not be applied directly to magnetic CVs, where the eclipse ingress and egress of the white dwarf is superimposed by the eclipse of the accretion spot, we tried a similar approach. First the eclipse light curve was smoothed with a median filter. Then the times when the derivative of the light curve became non-zero were determined. We also applied a box car filter to the derivative to aid in the detection of the contact points. The filter width for the median and the box car filter were varied between 2 and 7 seconds. Finally we determined the contact points visually
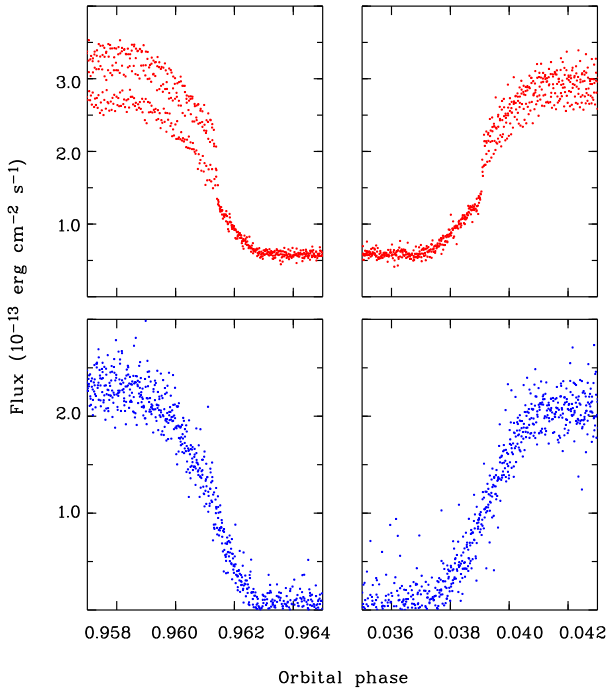
Figure 5.3:
Phase folded eclipse light curve of all observations from May 14-17 2007 in u (lower panel) and r (upper panel). While the u band light curve shows just the ingress and egress of the white dwarf together with the spot, the r band light curves also shows a variable cyclotron component (which causes the different flux level outside the eclipse for the individual eclipses).

using the original data and eclipse light curves smoothed with a median filter of 5 seconds. Surprisingly the contact points determined visually from the smoothed data showed the smallest scatter between the individual eclipses and filters as well as the smallest errors. We therefore used these timings for the further analysis. From the timings of the contact points for all available eclipses in all three filters we determined the eclipse width, the length of the white dwarf eclipse ingress, the length of the white dwarf eclipse egress and the orbital period. The mean values are summarized in Table 5.2 (top).

With the measured eclipse width and the orbital period the mass ratio q can be calculated as a function of the inclination i, which is in the case of HU Aquarii fairly well determined (Schwope et al. 2001). For the further analysis we fixed the inclination at an angle of 85.5°. With the assumption that the secondary fills its Roche-lobe, the length of eclipse ingress/egress of the white dwarf now determines the radius of the white dwarf in units of the binary distance a.

Assuming a white dwarf mass together with the orbital period one obtains for a given mass ratio q immediately the binary distance in absolut units, leading to a radius of the white dwarf also in absolute units. Using a mass-radius relation for white dwarfs (see Section 4.3) one finds the real white dwarf mass. This is when assumed mass and resulting radius fulfill the mass-radius relation. Since q is already known, the white dwarf mass gives immediately the mass of the secondary. The azimuth of the accretion spot was determined from the orbital maximum of the u band light curve. With the known system parameters and the determined azimuth of the spot, the phase of spot egress gives the colatitude of

Timing parameters (determined from observations)

Eclipse width	586.3(3) sec
White dwarf width	30.6(3) sec
Period	7501.4(2) sec

System parameters (determined from the timings above)

Inclination		84.5	85.5	86.3
Mass ratio q		0.261(1)	0.241(1)	0.228(1)
Mass of WD	[M$_\odot$]	0.895(9)	0.879(9)	0.869(9)
Mass of secondary	[M$_\odot$]	0.234(3)	0.212(3)	0.198(3)
Azimuth spot	[°]	46(1)	46(1)	46(1)
Colatitude spot	[°]	25(2)	23(2)	20(2)
RV (K1) WD	[km/s]	103.4(6)	95.8(6)	91.1(6)
RV (K2) Secondary	[km/s]	395(1)	398(1)	399(1)
RV L1	[km/s]	185(1)	198(1)	205(1)

Table 5.2:
Measured timings from the ULTRACAM run in 2005 and the resulting system parameters for three different inclinations. The radial velocities (RV) are given for the center of mass and for the L1 point.

the spot. The spot ingress and egress is only observed in g and r band but not in the u band and is therefore caused by the cyclotron radiation not by the heated pole cap. The locations of pole cap and cyclotron spot have not to be coincide, thus the derived colatitude refers to the cyclotron spot, but the accretion geometry in HU Aqr exhibits an accretion stream fairly parallel to the limb of the secondary at the orbital phase of spot egress, making a large deviation of the true colatitude of the pole cap unlikely. The derived system parameters as well as the resulting radial velocities are summarized in Table 5.2 (bottom). For comparison the resulting system parameters for the two differing inclinations are also given.

The mass obtained for the secondary can be compared with the semi-empirical donor star sequence of Knigge (2006). The orbital period of HU Aquarii results in a secondary mass of $M_2 = 0.19\ M_\odot$, i.e. our value gives a somewhat higher mass than expected and thus implies a higher inclination. The white dwarf mass of $M_{\rm WD} = 0.88\ M_\odot$ falls well within the broad range for mean white dwarf masses in CVs (compare with Fig. 1.6) and is in agreement with the value derived by Glenn et al. (1994) from eclipse timings and measured radial velocities. Table 5.2 also gives our predicted radial velocities (RV) $K1$ and $K2$, which can be compared to measured RVs. Schwope et al. (1997) obtained a value

of 294(1) km s^{-1} for the center of light of the illuminated hemisphere of the secondary by fitting the He II emission lines arising from the donor star. The problem here is, that the center of light has to be corrected to the center of mass of the secondary. This depends not only on the mass ratio q, but also on the actual location of the center of light, which is in the case of illumination located between the L1 point and the center of mass. However, using Doppler-Tomography to fit the observed Balmer and He II lines, they derived values between 350 and 387 km s^{-1} for $K2$ and thus somewhat lower values than predicted by our model.

The derived azimuth of $\Psi = 46°$ for the location of the heated pole cap does not depend on our system parameters and is in good agreement with the given values elsewhere (Vrielmann & Schwope 2001, Schwope et al. 2001, Bridge et al. 2002). Schwope et al. (2001) found that the center of X-ray bright phase is correlated with the mass accretion rate and reaches $46°$ as a maximum during high state. In this respect our result of $46°$ for a low state is noteworthy. But as already mentioned by the authors, this correlation is not unambiguous and breaks down already for the EUVE[2] observations, where the center of bright phase remains at large azimuthal angles. The large azimuthal angle could also imply, that the heated pole cap is a residual from the preceding high state, instead of being caused by the current accretion.

5.4 The white dwarf in HU Aquarii

5.4.1 The white dwarf temperature

The white dwarf temperature in CVs can be determined best from the spectral energy distribution. As mentioned in Chapter 1 this is not trivial, since the pure white dwarf emission is contaminated by emission from the accretion region and the accretion stream. HU Aquarii possesses only one accretion spot, thus the contribution from the accretion region can be excluded at orbital phase intervals when the spot is self-eclipsed. The ULTRACAM and XMM OM observations in May 2005 took place during a low state, which inherently has no or just a minor contribution from the accretion stream. We can therefore claim, that both ULTRACAM and XMM OM observations shows the pure white dwarf during faint phase. To extend the spectral range we also used spectra obtained with the *Faint Object Spectrograph* FOS onboard the Hubble Space Telescope in September 1996 during an intermediate accretion state. The mean spectrum can be seen in Fig. 5.5 and the resulting and already phase folded light curve when integrating the individual spectra is shown in Fig. 5.4. The light curve shows nicely two characteristics of mCV light curves explained in Chapter 1: the stream dip prior to eclipse (marked with 'A' in Fig. 5.4) and the eclipse ingress of the accretion stream (marked with 'B' in Fig. 5.4) after the

---

[2]Extreme Ultraviolet Explorer (EUVE), a NASA satellite for the wavelength range 70-760 Å, active from 1992 to 2001.
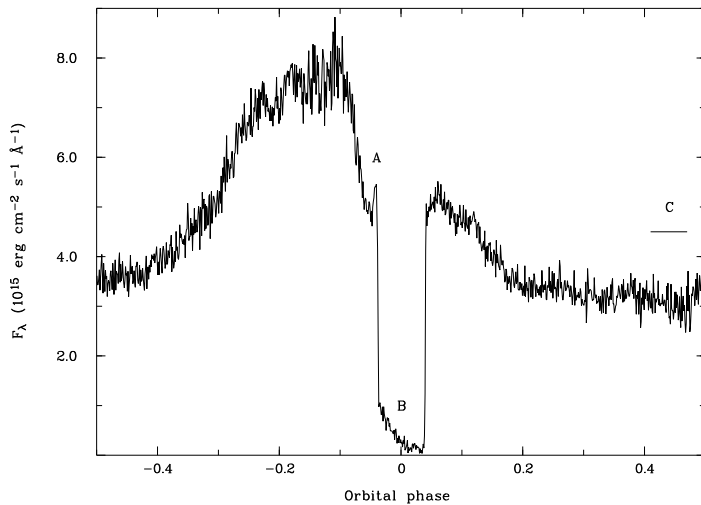
Figure 5.4:
Resulting phase folded and integrated light curve (1200 – 2500 Å) from all HST FOS spectra obtained in September 1996. Stream dip and stream ingress are marked with 'A' and 'B', respectively, the used phase interval for the faint phase spectrum with 'C'.

white dwarf is already eclipsed. From this light curve it becomes immediately clear, that the accretion stream provides a substantial fraction of the overall flux. To subtract the contribution from the accretion stream a mean spectrum from the faintest phase interval (besides the eclipse phase) between orbital phase 0.41 and 0.47 was created first. This spectrum has the lowest contribution from the accretion stream. Then a spectrum of the pure accretion stream was created, using a phase interval, where the white dwarf is already eclipsed (both spectra were rather noisy). Secondly, a continuum-subtracted light curve of the CIV emission line, originating in the accretion stream was generated from all FOS spectra. The flux ratio of the CIV line between faint phase and time of stream ingress was then used to scale the stream spectrum to the likely flux level of faint phase. The thus scaled stream spectrum was then subtracted from the mean spectrum of the faint phase. The remaining residual (the blue spectrum in Fig. 5.5) can be claimed as the white dwarf contribution.

Obviously several problems arise due to this approach. On one hand the implicit assumption is that the continuum emission from the stream behaves like the optically thick emission of the CIV line, on the other hand it is assumed that the spectrum at faint phase is comparable to the spectrum at stream ingress, which implies optically thin emission. Furthermore the Doppler shift of the lines between faint phase and phase of stream ingress is not taken into account. This leads, as can evidently be seen in Fig. 5.5, to a bad subtraction of the emission lines (which are not arising from the white dwarf) from the faint phase spectrum.

While these residual lines in the remaining spectrum are simply data reduction artefacts, the continuum should fairly well reflect the white dwarf contribution to the faint phase spectrum. Finally white dwarf model spectra for different temperatures where suitable scaled and superimposed to the spectral energy distribution of HST FOS, XMM OM and ULTRACAM data. The best fitting temperature was found to be 13500 ± 200 K. The spectral energy distribution of the used data together with a white dwarf model spectrum
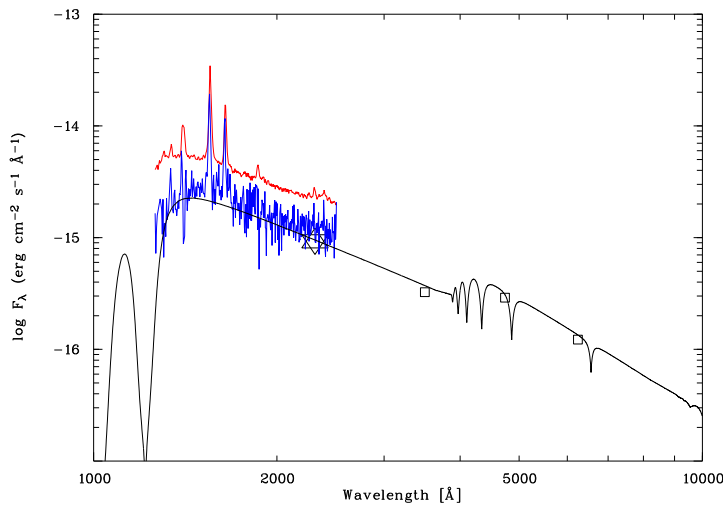
Figure 5.5:
The temperature of the white dwarf in HU Aquarii. Best fit model with 13500 K to the low state ULTRACAM data from May 2005 (squares) and the contemporary XMM OM data (star), both for the faint phase between orbital phase 0.41 – 0.47, together with the intermediate state HST FOS spectrum from 1996. The white dwarf spectrum (blue) was obtained from the mean spectrum (red) by substracting the stream component (see text for details).

for 13500 K is shown in Fig. 5.5.

5.4.2 Mapping the white dwarf

With the known system parameters and white dwarf mean temperature we tried to model the heated pole cap and accretion spot of the white dwarf. Therefore the ULTRACAM light curves had to be prepared. Firstly a phase folded light curve of all ULTRACAM observations from 2005 was created for each filter. Since out of eclipse the light curves were affected by accretion flickering, the final light curves were composed from the phase folded mean light curve for the phase intervals of the eclipse ingress and egress, where a high time resolution is crucial, and from the light curve of the first night for the orbital phase interval outside eclipse, since they are least contaminated by additional accretion flickering and cyclotron radiation (see Fig. 5.2 upper panel). During eclipse the white dwarf itself provides no flux contribution. Therefore the mean flux level during eclipse was determined and substracted from the light curve as a constant value, to account for the contribution of the secondary. The remaining components contributing to the light curve are the ellipsoidal variations of the secondary and the variable cyclotron emission. Both components can be neglected for the u band light curve. For the g and r band light curve these contributions are non-negligible. While the elipsoidal variation of the secondary can be simulated, the much larger contribution of the cyclotron component raises problems. The cyclotron emission is strongly non-isotropic. From the eclipse egress of the spot at orbital phase 0.039 the contribution can be determined with high accuracy but this gives no further hint on the contribution at other orbital phases. A subtraction of the cyclotron

component for the full orbit would lead to a light curve with a high uncertainty. Therefore the g and r band light curves were only considered for phase intervals where the spot is eclipsed by the secondary. i.e. for the phase interval -0.0385 - 0.039.

The composed phase folded light curves (see Fig. 5.5), together with the determined system parameters were then used as input parameters for DWARF. A pretty good fit to the observed light was reached in terms of χ^2, but immediately a problem arose. The size of the spot can mainly be constrained from it's eclipse profile. Neither the u band nor g or r bands (after subtraction of the flux contribution of the cyclotron spot, assumed as constant for the phase interval of eclipse ingress and egress of the white dwarf) show a clear or unambiguous feature which can be ascribed to the spot (see Fig. 5.6). Instead the contribution of the spot is smoothly blended with the contribution of the unheated white dwarf photosphere.

The out-of-eclipse light curve was not sufficient to obtain a physically meaningful temperature map. We therefore used a simple two-parameter model. Assuming a circular isothermal spot on the surface of the white dwarf only temperature and size of the spot remain as free parameters. Since the shape of the spot is fixed by this approach it does not focus on the eclipse profile. The resulting fit is shown in Fig. 5.6, the derived parameter in Table 5.3.

As can be seen in Fig. 5.6 the u band flux is somewhat overpredicted by the model. Since the r band flux is reproduced very accurately, incorrect system parameters are unlikely to be the reason. To verify this, we repeated the fits with the eclipse timings from Table 5.2 (top) modified by up to 3 seconds. Apart from non-fitting contact points the problem remains the same. Either the u band flux was overpredicted by the model (while the r band flux fitted) or the r band flux was underpredicted (while the u band flux fitted). The likely reason for the slight discrepancy between u and r band is most likely the not included limb darkening or the constant temperature profile of the spot in our model.

T_{WD} [K]	13500	± 200
T_{Spot} [K]	25500	± 1000
A_{Spot}/A_{WD}	0.046	± 0.01
d [pc]	183	± 3

Table 5.3:
The temperature of the white dwarf and temperature and size of the pole cap resulting from a two-parameter fit to the composed ULTRACAM light curves of Fig. 5.6 using the system paramters from Table 5.2.

Fig. 5.7 shows the XMM OM observation from May 16, 2005 in the UVM2 filter. While the observed count rate was too low to achieve a sufficient time resolution for eclipse ingress and egress, the overall shape of the OM light curve can be used for a consistency check of the derived white dwarf parameters. Therefor our white dwarf model was folded through the response curve of the OM (see Fig. 4.6). The observed count rate during
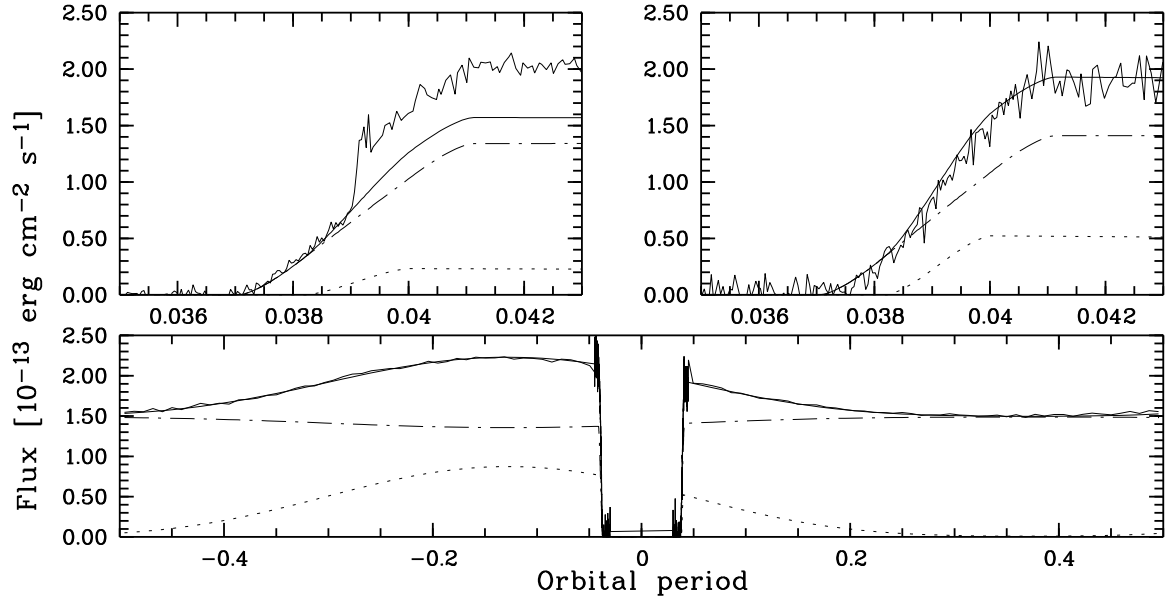
Figure 5.6:
The plot shows the ULTRACAM data obtained in May 14 - 17, 2005 for a complete orbit (bottom) in u and for the eclipse egress in u (upper right) and r (upper left). Overplotted is the white dwarf model resulting from a fit to the u band data. The solid line shows the summed contribution from the white dwarf (dashed line) and the spot (dotted line). The plot in the upper left illustrates the additional cyclotron component. The ULTRACAM light curve was composed of all ULTRACAM eclipses from 2005 and the light curve from May, 14 for out of eclipse times.

faint phase is reproduced very accurately, but there is an obvious discrepancy between the observed count rate and the predicted count rate during bright phase. If the OM light curve were composed solely by the contribution from the white dwarf and the heated pole cap, the observed light curve would imply a somewhat higher temperature of the pole cap or a somewhat bigger pole cap. With $T_{Spot} \sim 27000$ K and $A_{Spot}/A_{WD} \sim 0.065$ the OM light curve can be reproduced sufficiently well, but with the same parameters the u band flux of the bright phase is overpredicted by one-third.

On the other hand the simultaneous XMM X-ray observation reveals emission at a level to high to originate exclusively from the secondary (Schwarz et al. in preparation). Also the ULTRACAM observation reveals residual accretion in all three filters (see Fig. 5.2 bottom panel). Thus an additional contribution from an accretion stream cannot be excluded. Also our assumption of a white dwarf spectrum for the heated pole cap could be an oversimplification.

Figure 5.7:
The XMM OM observation from May 16, 2005 (UVM2 filter) together with the theoretical contribution from our white dwarf model with the parameters from Table 5.2 and 5.3. Line types are the same as in Fig. 5.6.
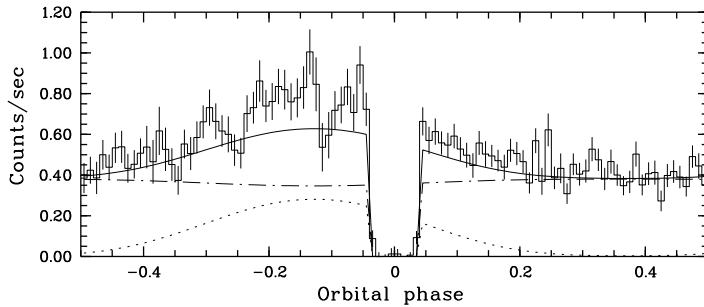
5.5 The orbital period decrease

Since it's discovery in 1992 HU Aquarii was observed many times. The dense coverage over the last 15 years made it possible to determine the ephemeris with a high precision.

One challenge when establishing an ephemeris is to find a fixed (in terms of the orbital period) short term event within the light curve. The special problem with magnetic cataclysmic variables is that prominent features are (almost) always variable in orbital phase. A clear feature found in many observations is the eclipse of the accretion spot (see the r band eclipse light curve in the upper panel of Fig. 5.3). The spot eclipse can be seen in optical observations as well as in X-ray observations and provide a clear marker to establish an ephemeris. A problem with this feature is the non-steadiness of the spatial position of the accretion spot. For a given magnetic field the locus of the accretion spot depends from the location of the threading region, which depends from the accretion rate and velocity of the matter coming from the secondary. As could be shown for HU Aquarii the locus of the accretion spot can shift towards lower azimuthal angles for lower accretion rates (Schwope et al. 2001). Finally it can not be decided definitely if a discrepancy between predicted and observed spot eclipse is inherent to the system, or simply reflects a shifted spot location.

A second, and on first glance obvious approach would use only observable features that occurs always at the same orbital period. The eclipse of the white dwarf provides such a reliable feature, but leads to the opposite problem as in the case of the accretion spot. The white dwarf eclipse happens always at the same orbital phase but is most of the times hard to detect in the observations. In an eclipsing system the white dwarf provides four time markers: start and end of eclipse ingress and start and end of eclipse egress of the white dwarf. The eclipse ingress and the end of the egress can, and most of the times will, be affected by the emission from accretion stream and spot. The remaining feature is the beginning of the white dwarf egress. Since this is a very weak feature it can be determined only with a high uncertainty of several seconds – if it can be determined at all.

While the former method (egress of the accretion spot) can be applied to nearly all available observations, the latter method leads to more accurate timings. An ephemeris

Date	Instrument	Filter	Time resolution	No. of eclipses
1993	MCCP	B	0.5 s	8
1996	HST	[1]	2.5 s	3
1999	OPTIMA	white	1.0 s	2
2000	OPTIMA	white	1.0 s	2
2001	OPTIMA	white	1.0 s	2
2002	ULTRACAM	r	0.5 s	2
2003	ULTRACAM	r	0.5 s	1
2005	ULTRACAM	r	0.5 s	5

[1] used wavelength range 1920-2240 Å

Table 5.4:
Overview of the data used for measuring the beginning of the white dwarf egress.

derived from all available observational data using the times of the egress of the accretion spot already revealed a significant quadratic term of the ephemeris (Schwarz et al. in preparation). A shift of the accretion spot was not taken into account, but the deviation from a linear ephemeris amounts to ~ 40 seconds for the baseline of ~ 12 years, which rules out a shift of the spot location as a reason for the deviation (the duration of the complete ingress or egress of the whole white dwarf is just 30.6 seconds). We used the analysis of the ULTRACAM data to improve the determination using the white dwarf eclipse timings and to establish a precise non-linear ephemeris, which does not suffer from an unsteady spot location. With the system parameters determined above we computed a light curve of the naked white dwarf. This in turn was used as a template to determine the times of the white dwarf eclipse in light curves obtained between 1993 and 2005. We selected all data, where the beginning of the white dwarf egress was identifiable. The ingress of the white dwarf was outshone by the accretion stream in all light curves aside from the ULTRACAM run in 2005, so we used here just the white dwarf egress to adjust our template. To increase the signal-to-noise ratio several observations covering more than one eclipse per night or in nights only a few days apart were phase-folded with the ephemeris determined from the spot timings. In these cases we obtained just one date, but with a higher accuracy. All used observations are summarized in Table 5.4.

Then our white dwarf template was superimposed on the data and visually aligned to the eclipse egress of the white dwarf to obtain the beginning of the egress. At first glance a minimisation technique would provide more objective results, but one has to define the beginning of the spot egress, since only data points belonging solely to the white dwarf have to be considered. The determination of the beginning of the spot egress is often not uniquely possible (see the observational data in Fig. 5.8) and thus a minimisation technique suffers from the same amount of subjectivity. The OPTIMA data - taken in white light - revealed another problem. Since they can not be flux calibrated, the relative contribution of the white dwarf can not be determined. For these observations we scaled

Instrument	No. of eclipses	Date	Start of egress [BJED]	Cycle
Ultracam	1	15/05/2005	2453506.884970(12)	49418
Ultracam	1	15/05/2005	2453506.798160(12)	49417
Ultracam	1	14/05/2005	2453505.929950(12)	49407
Ultracam	1	14/05/2005	2453505.843150(35)	49406
Ultracam	1	13/05/2005	2453504.888111(23)	49395
Ultracam	1	24/05/2003	2452783.671190(23)	41088
Ultracam	2	19+20/05/2002	2452413.642656(23)	36826
Optima	2	21/09/2001	2452174.278919(35)	34069
Optima	2	05/07/2000	2451731.494872(35)	28969
Optima	2	21+25/06/1999	2451350.874166(35)	24585
HST	3	30/08/1996	2450325.959008(35)	12780
MCCP	2	18/08/1993	2449218.390983(35)	23
MCCP	3	17/08/1993	2449217.435945(23)	12
MCCP	3	16/08/1993	2449216.394090(23)	0

Table 5.5:
Times of the beginning of the white dwarf egress for all used data. Numbers in parentheses indicate the uncertainties in the last two digits. For the eclipse light curves composed from multiple observations, time and cycle number refer to the first observed eclipse egress. The used white dwarf template and eclipse light curve can be found in Fig. 5.8.

the white dwarf contribution in the following way: At the time of spot egress roughly half of the white dwarf is still eclipsed. We therefore determined the count rate at the time of spot egress and scaled the white dwarf contribution outside eclipse to a count rate two times the count rate at the time of spot egress.

Figure 5.8 shows all used data with the superimposed white dwarf model. Vertical lines indicate the beginning of the white dwarf egress, horizontal lines the errors. Dashed lines indicate the flux level at faint phase, composed from contributions of the white dwarf and the accretion stream (since the figures show only the phase interval of the white dwarf egress and not the phase interval of the subsequent accretion stream egress, they lead - in the case of the MCCP data - to the (wrong) impression, that the flux level at faint phase lies above the flux level at bright phase). The obtained timings are summarized in Table 5.5. In cases where we used eclipse light curves composed from multiple observations, time and cycle number refer to the first observed eclipse egress.

First we tried a linear regression to all the timings of Table 5.5, which yields as in the case for the spot timings a rather poor fit (red. $\chi^2 = 31.4$) and showed residuals up to 30 seconds. After including a quadratic term the χ^2 of the fit decreased significantly (red. $\chi^2 = 2.1$) and resulted in the quadratic ephemeris

$$BJED = 2449216.394086(14) + E \times 0.0868204358(15) - E^2 \times 5.75(28) \times 10^{-13} \quad (5.1)$$
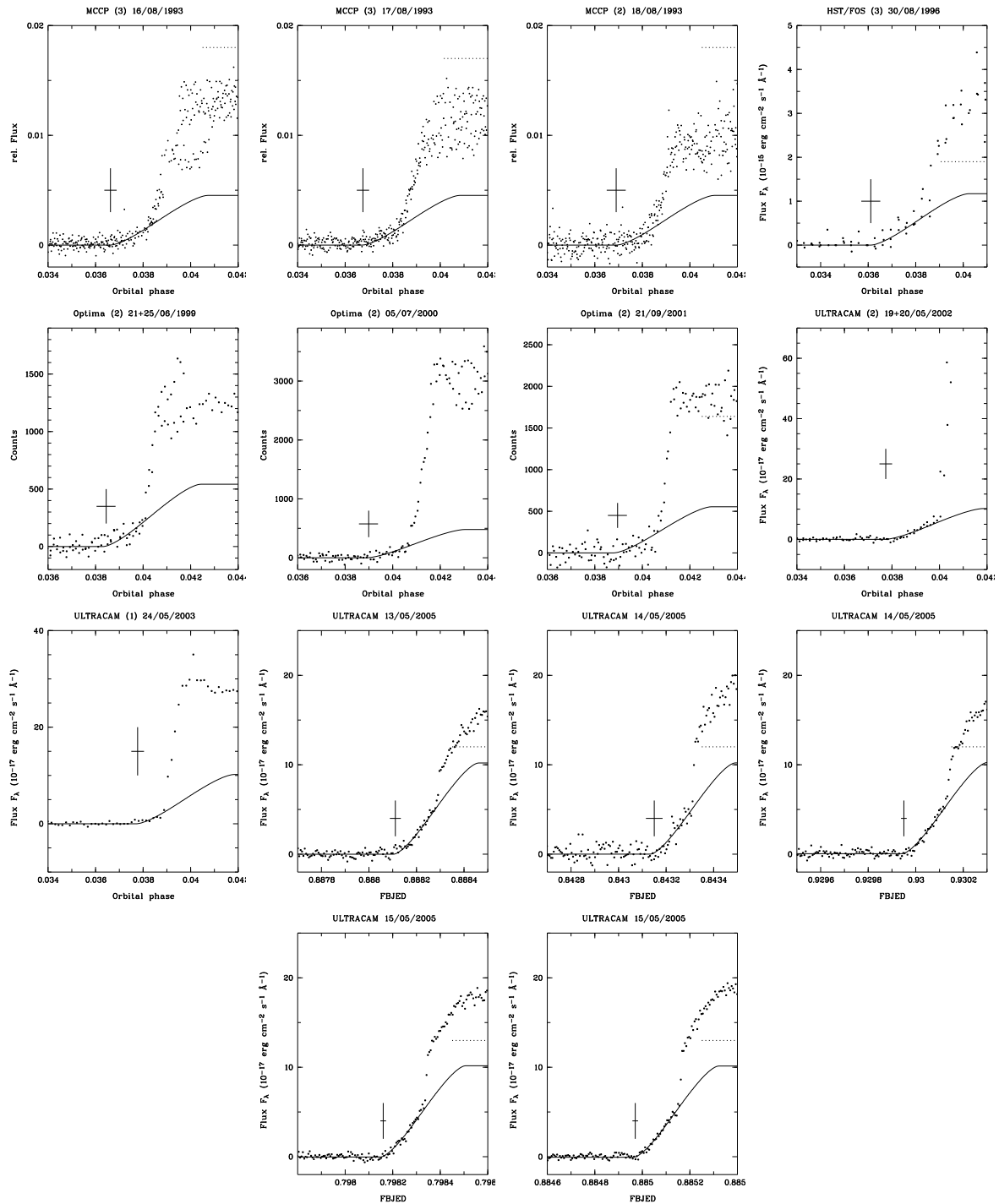
Figure 5.8:
All data used to determine the beginning of the white dwarf egress with superimposed white dwarf model. Vertical lines indicate the beginning of the white dwarf egress, horizontal lines the errors. Dashed lines indicate the flux level at faint phase, composed from contributions of the white dwarf and the accretion stream. See also Table 5.4 and 5.5.

Figure 5.9:
O-C plot after subtraction of the linear fit. Notation: MCCP data (hexagon), HST-FOS data (square), OPTIMA data (triangle), Ultracam data (star).
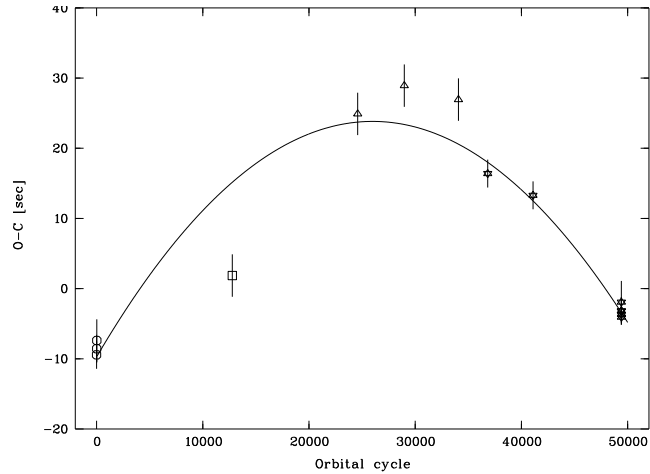
where E denotes the orbital cycle number and the numbers in parentheses indicate the uncertainties in the last two digits. The fit is still not satisfying as can be seen in Fig. 5.9, which shows the differences between predicted (solid line) and observed times (symbols) for the beginning of the white dwarf egress. The O-C plot implies rather a variable period change on a time scale of years than a long-term period decrease at a constant rate.

5.5.1   Possible explanations of the period decrease

As already explained in Chapter 1, CVs lose angular momentum due to magnetic braking and gravitational radiation, which results in a period decrease. We therefore compare the observed period decrease with the expected period decrease. The ephemeris from Eq. 5.1 gives $\dot{P} = -1.3 \times 10^{-11}$ ss^{-1} and a total period change over the 11.75 years of observations of $\Delta P = 4.9 \times 10^{-3}$ s. The angular momentum of the binary system is given by

$$J = \left(\frac{Ga}{M}\right)^{\frac{1}{2}} M_1 M_2 \tag{5.2}$$

where a is the binary distance. Combining this equation with Kepler's third law the angular momentum loss (AML) is given by

$$\dot{J} = \frac{2}{6}\left(\frac{G^2}{2\pi M}\right)^{\frac{2}{6}} M_1 M_2 P^{-\frac{4}{6}} \dot{P} \tag{5.3}$$

resulting in an AML of -5.8×10^{35} erg. The above equation is strongly valid only for constant masses of the white dwarf and the secondary, but for the low mean accretion rates in cataclysmic variables below the gap ($\sim 10^{-10} M_\odot$/yr) the mass transfer can be neglected on those time scales. For increasing accretion rates the mass transfer will lead to higher angular momentum loss rates.

According to the standard theory HU Aquarii as a system below the period gap should lose angular mometum solely by gravitational radiation. The AML caused by gravitational radiation (Landau & Lifschitz 1958) is given by

$$\left(\frac{dJ}{dt}\right)_{\text{gr}} = -\frac{32}{5}\frac{G^{\frac{7}{2}}a^{-\frac{7}{2}}}{c^5}M_1^2 M_2^2 \left(M_1 + M_2\right)^{\frac{1}{2}} \tag{5.4}$$

resulting in $\dot{J}_{\text{GR}} = 1\times 10^{34}$ erg. This is a factor of 60 below the observed value. Thus, there must be an additional braking mechanism. As explained in Section 1.6, it is still under discussion if the magnetic braking breaks down, when the star becomes fully convective, as supposed by the standard model. The reduced magnetic braking model inferred from open-cluster low-mass stars (Andronov et al. 2003) suggests that there is no cut-off of the magnetic braking when the secondary becomes fully convective and that the AML rate predicted by the standard model is to high. According to Andronov et al. (2003) the AML for the reduced magnetic braking model can be modelled with

$$\left(\frac{dJ}{dt}\right)_{\text{rmb}} = -K_w \left(\frac{r_2}{m_2}\right)^{\frac{1}{2}}\frac{2\pi}{P}\omega_{\text{crit}}^2 \tag{5.5}$$

for systems with $2\pi/P > \omega_{\text{crit}}$, where ω_{crit} is the critical angular frequency at which the AML rate enters a saturated regime. The constant $K_w = 2.7 \times 10^{47}$ g cm s^{-1} is calibrated to give the known solar rotation period at the age of the sun. r_2 and m_2 are radius and mass of the secondary in solar units. This results in an AML of $\dot{J} = 1.4 \times 10^{33}$ erg, which is two orders of magnitude below the required one and thus is also not able to explain the period decrease of HU Aqr.

Ignoring the cut-off of magnetic braking the predicted loss rate for the standard model (Rappaport et al. 1983) is given by

$$\left(\frac{dJ}{dt}\right)_{\text{mb}} \approx -3.8 \times 10^{-30}MR_{\odot}^4 \left(\frac{R}{R_{\odot}}\right)^{\gamma}\omega^3 \tag{5.6}$$

where $0 \le \gamma \le 4$ is a dimensionless parameter. The resulting AML is $5.6 \times 10^{34} < \dot{J} < 2.2 \times 10^{37}$ erg and thus can explain the loss rate implied by the observed period decrease, but this induces severe problems since neither period gap nor period minimum are compatible with that explanation (see Sect. 1.6).

Either our data imply a higher AML than predicted by the standard model and thus an additional braking mechanism below the period gap or the period decrease is not a pure AML effect. A change of the orbital period is observed in several classes of close binary sytems (Algol-type binaries, W Ursae Majoris systems, RS CVn, CVs). Some of the observed period changes are confirmed to be cyclic. In general the period of cyclic changes is rather large, e.g. 56 years in the case of the Algol-type WW Cyg (Zavala et al. 2002), which requires observations extending over decades to identify cyclic changes. Since

HU Aquarii was discovered in 1992, the baseline is far too short to make any statement about a periodicity of the period change. Three mechanisms have been proposed to explain cyclic changes of the period.

Apsidal motions - a change in the orientation of the binary's major axis - require binary systems with large eccentricities. Since close binaries possess circular orbits this mechanism is unlikely to cause the observed period change.
Another possibility involves an unseen third body. As in the case of apsidal motions the period change is just a light-time effect and is strongly sinusoidal. To determine the mass of the third body we fitted our eclipse timings with a linear ephemeris superimposed by a sinusoidal modulation:

$$T = T_0 + P \times E + A_3 \times \sin\left(\frac{2\pi}{P_3}E + E_0\right) \qquad (5.7)$$

where T_0 denotes the zero point of the ephemeris, P the period of the binary system, A_3 and P_3 the amplitude and period of the sinusoidal modulation, E the cycle number and E_0 the offset between T_0 and the zero point of the sinusoidal modulation. To arrive at the minimum mass, P_3 was fixed at the shortest possible period of the sinusoidal modulation, i.e. 2×11.75 years. With the obtained amplitude A_3 of 37.6 seconds the mass M_3 of the third body can be determined (Borkovits & Hegedues 1996) by

$$\frac{4\pi^2 (a_{12}\sin i)^3}{GP_3^2} = \frac{(M_3 \sin i)^3}{(M_1 + M_2 + M_3)^2} \qquad (5.8)$$

where a_{12} is the semiaxis of the eclipsing-pair orbit around the center of mass of the triple system and is given by $a_{12}\sin i = A_3 c$. Since we are interested in the minimum mass, we assume an inclination of 90° for the orbit of the third body. This gave $M_3 = 0.007$ for the minimum mass of the third body. An upper limit for the mass can be derived from the fact, that the third body must be fainter than the observed brightness during eclipse, which limits the maximum mass to $M_3 < 0.2$.

The third possibility, the so-called Applegate mechanism (Applegate 1992, Lanza et al. 1998) involves the magnetic activity cycle of the secondary. The redistribution of angular momentum by a magnetic torque lead to a change in the rotational oblateness of the star. The changes of the shape of the star induce a change of the quadrupole moment of the star, which in turn is coupled to the binary orbit and causes a change in the orbital period, while the angular momentum of the binary remains constant. Applegates idea is supported by the investigation of Hall (1989), who found that Algol-type binaries with alternating period changes always possess secondaries with a spectral type later than F5, i.e. stars with an outer convective zone. He already concluded that the onset of convection, and thus magnetic activity, is connected with the orbital period modulation.
Since the original calculations of Applegate assumed a fixed shell mass of 0.1 $M_\odot$, which is certainly doubtable for a 0.2 $M_\odot$ secondary as in the case of HU Aquarii, and did not account for the quadrupole moment of the core, we used the improved method of

Figure 5.10:
The required energy (solid line) to drive the Applegate mechanism as a function of the outer shell mass (in solar units). The short dashed line indicates the total energy available (total radiant energy) of the star in 11.75 years.
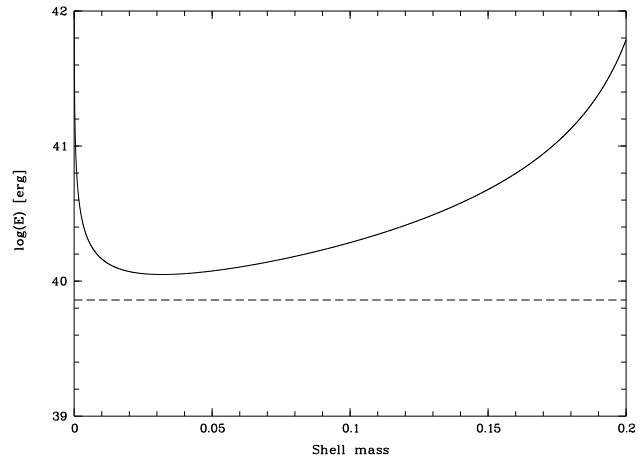
Brinkworth et al. (2006) to calculate the required energy to drive the Applegate mechanism. Fig. 5.10 shows the result as a function of the assumed shell mass. The total energy available over the time of observations can be determined from the luminosity of the star

$$E = L_2 \Delta t = 4\pi R^2 \sigma T_{\text{eff}}^4 \Delta t \tag{5.9}$$

where Δt is the span of time covered by observations. Assuming $T_{\text{eff}} < 3300$ for a spectral type later than M4 the total radiant energy is $E < 7.34 \times 10^{39}$ erg and thus less than needed. We therefore claim that the observed period decrease in HU Aquarii can not be caused by the magnetic activity of the secondary.

5.6   Summary

Using high-speed optical ULTRACAM observations during low state, we were able to get precise eclipse timings for the eclipse ingress and egress of the white dwarf. From these timings we could derive very accurate system parameters for HU Aquarii. The white dwarf is rather massive with $M_{\text{WD}} = 0.88 M_\odot$, the secondary with $M_2 = 0.21 M_\odot$ slightly more massive than the predicted $0.19 M_\odot$ from Knigge (2006). Together with HST-FOS and XMM-OM data the temperature of the white dwarf could be determined. The temperature of $T_{\text{eff}} = 13500 \pm 200$ K together with the derived white dwarf radius yields a distance of 183(3) pc.
Constructing a theoretical white dwarf light curve from our parameters and using MCCP, HST and OPTIMA data from 1993 to 2005, we determined accurate eclipse timings. With these eclipse timings we could establish a significant non-linear ephemeris. The implied angular momentum loss is a factor of 60 too high to be explained by gravitational radiation alone. This implies either an additional braking mechanism below the period gap - contrary to the standard model - which is under discussion since years (see Sect. 1.6) or evidence for an unseen third body with $0.007 < M_3 < 0.2$. The Applegate mechanism could be ruled

out as a reason for the observed period decrease in HU Aquarii. To improve the ephemeris and to detect a possible periodicity in the orbital period change, further observations with high time resolution are crucial.

Chapter 6

Conclusion and outlook

In this work data from the three systems WX LMi, 2XMM1312, and HU Aqr were analysed. The results suggest changes in the current picture of polars regarding different aspects.

The likely pre-polar WX LMi shows a spectral energy distribution dominated by the highly active secondary in the infra-red. In the optical regime emission from the cool white dwarf and cyclotron emission from the plasma being accreted contribute predominantly. The weak X-ray contribution is composed of emission from the corona of the secondary and from the accretion column. While the observed light curves and spectra are typical for a polar, the spectral energy distribution revealed immediately an unusual condition of WX LMi. The detailed analysis of optical, ultraviolet and X-ray observations identifies it as a progenitor of polars. The white dwarf temperature of < 8000 K is far below the observed in other polars. Considering the secular evolution of white dwarfs, this low temperature excludes a former accretion at higher rates than determined from the observations. The accretion rate is of the order of $10^{-13}\,\mathrm{M_\odot\,yr^{-1}}$, magnitudes below the observed accretion rates in normal polars, but within the same order as the wind mass-loss rate of the secondary star. The low accretion rate together with the high magnetic field strength allowed for testing current accretion models. At these low accretion rates probably no accretion shock forms. The plasma being accreted should cool mainly via cyclotron radiation instead of bremsstrahlung. This was confirmed by disentangling of the spectral energy distribution. Due to the rather unusual spectral energy distribution, these pre-CVs were hidden on their track towards Roche-lobe overflow. While polars were found to be numerously in the ROSAT all-sky survey, because of their prominent soft X-ray component, the progenitors of polars are only weak X-ray emitters. A dedicated search using optical spectroscopic surveys like SDSS will certainly recover new systems, giving a less biased view of the population and evolution of polars, and offering the opportunity to further explore the regime of very low accretion rates.

The polar 2XMM1312 showed a rather unusual spectral energy distribution too. Despite being in a high accretion state, there was no sign of the above mentioned soft X-ray

component. The low magnetic field strength of 2XMM1312 is a likely explanation, but this does not work for all of the few other systems also showing no soft component. Although they include system with low magnetic field strengths and with an asynchronously rotating white dwarf and thus supporting the thesis of an extended accretion region on the white dwarf as the reason for the missing soft component, they also include systems with a high magnetic field strength. The missing soft X-ray component – regardless of simply being shifted out of the observable wavelength range or being really absent – can have serious consequences for the current view of the polar population. The soft X-ray component was thought to be a key feature of polars. But systems without soft component like 2XMM1312 could reveal that this feature is not as characteristic as it was thought to be. In this case the polars discovered numerously in the ROSAT all-sky survey would constitute just a – strongly biased – fraction of the true population.

The analysis of optical and X-ray light curves and spectra of 2XMM1312 presented in this work, demonstrates nicely that, despite the superposition of different emission sources as typical for polars, the combined analysis of observational data covering a large wavelength range can be used to derive the system parameters very accurately.

The polar HU Aqr, in various aspects a prototype of a polar, was analysed with a different approach. Not the coverage in the spectral energy domain but the high resolution of the time domain could be used to re-determine the system parameters with high accuracy. This is a prerequisite for any detailed modelling of the energy balance in a polar.

An ephemeris with a highly significant quadratic term could be established. The underlying reason for the period decrease is still not clear. Beside HU Aqr three other CVs below the period gap show also a period change with the same order of magnitude, too large to be explained by the angular momentum loss due to gravitational radiation, as supposed by the standard model, the polar DP Leo (Schwope et al. 2002c), the SU UMa system OY Car (Greenhill et al. 2006) and the pre-CV NN Ser (Brinkworth et al. 2006). Actually NN Ser has a period of ∼187 minutes, but harbours a very low mass fully convective secondary. Thus for all three systems magnetic braking should have been ceased. Apart from being caused by angular momentum loss, possible explanations involve cyclic changes due to the Applegate mechanism or an unseen third body. The Applegate mechanism could be ruled out already for HU Aqr and NN Ser. While for other kinds of binaries as Algol-type systems and RS CVn systems both, period decrease and period increase – and even cyclic changes – are observed, the three CVs mentioned above all show a period decrease. Despite being statistically insignificant, it seems rather curious that all three confirmed period changes are negative. This suggests rather an enhanced angular momentum loss, than an unseen third body. This interpretation is in contrast to the standard model of CVs as explained in Chapter I., where CV systems below the period gap should lose angular momentum solely due to gravitational radiation. On the other hand both the observed orbital minimum period and empirical angular momentum loss rates obtained from open cluster stars implies a higher loss rate than caused by gravitational radiation alone.

The observed period change is in the order of 10^{-4} s yr^{-1}. This small change in period requires a highly accurate ephemeris and thus a long baseline of observations to be revealed.

The number of CV systems below the period gap with so highly accurately determined ephemerides is still too small to draw any firm conclusion.

Optical data with high time resolution were also used to derive size and temperature of the heated pole cap on the white dwarf for a low state. Such observations performed in frequent intervals could shed light on the cooling process of the accretion spot on the white dwarf, a rather unexplored domain.

Appendix A

Instruments and satellites

The following sections give a short overview of the instruments by which the data used in this work are collected or which played an important role for the work done in this thesis.

A.1 The X-ray satellite ROSAT and the RASS

ROSAT (**RO**entgen**SAT**ellit) was proposed already back in 1975 by the Max-Planck-Institut für extraterristrische Physik (MPE). It took fifteen years until ROSAT could be launched in 1990 on top of an american Delta-11 rocket.

ROSAT consisted of a Wolter-I telescope for the X-ray energy range of 0.1 – 2.4 keV (XRT – X-Ray Telescope) and another Wolter telescope for the soft X-ray/EUV energy range from 0.04 – 0.2 keV. The XRT was eqipped with a redundant proportional counter (PSPC – Position Sensitive Proportional Counter) with medium spatial and energy resolution and a MCP detector (HRI – High Resolution Imager) with a high spatial resolution of a few arc seconds but no energy resolution. The EUV telescope was equipped with a redundant MCP detector, the Wide Field Camera (WFC), providing a spatial resolution of one arc minute. In 1991 the satellite was faultily aligned towards the sun. This destroyed one of the PSPC detectors and damaged the WFC. The ROSAT mission was officially ended in February 1999.

One of the major goals of the ROSAT mission was an all sky survey in the soft energy range (RASS – ROSAT All Sky Survey), which was finished in February 1991. The RASS was the first – and is still the only one – all sky survey with a imaging X-ray telescope. The RASS increased the number of known (soft) X-ray sources from a few hundred before to tens of thousands afterwards.

Since magnetic cataclysmic variables are commonly soft X-ray emitters, the RASS played an important role for this field, since it doubled the number of known polars and thus boosted the knowledge of the field.
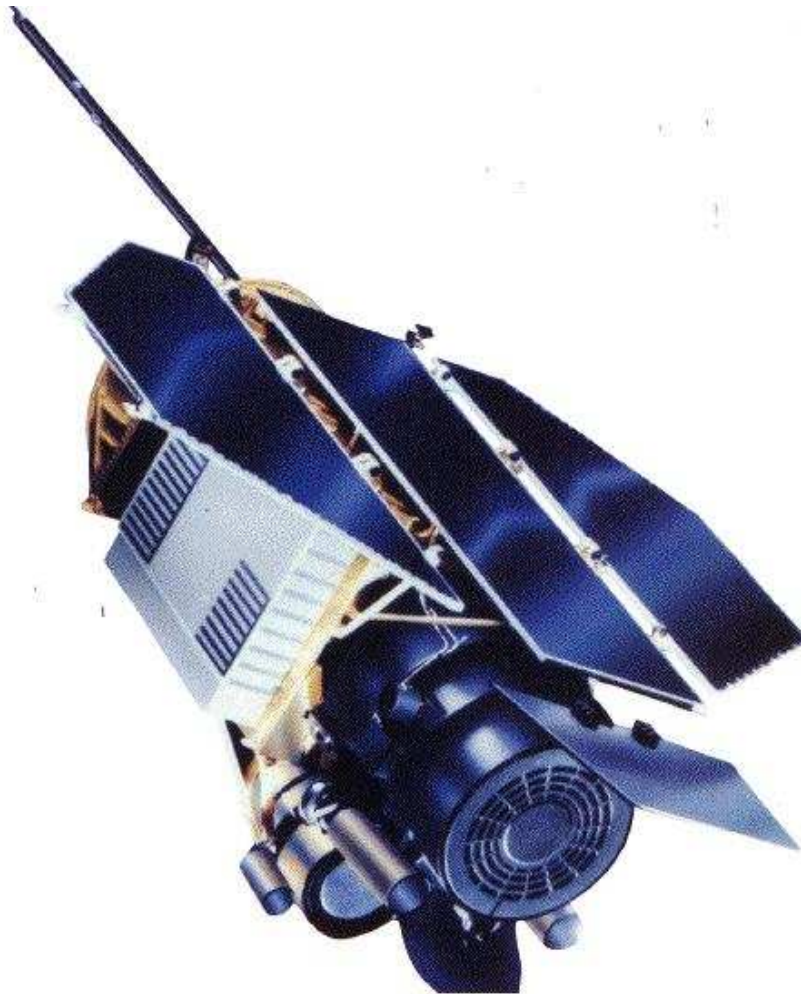
Figure A.1:
The german X-ray satellite ROSAT

A.2 The X-ray observatory XMM-Newton

XMM-Newton is a european X-ray satellite, launched into orbit in December 1999, consisting of three separate Wolter telescopes for X-ray imaging and spectroscopy and a 30 cm reflector for optical/UV imaging and spectroscopy. The three X-ray telescopes are equipped with the European Photon Imaging Camera (EPIC), which actually consists of three individual detectors, each capable of imaging and non-disperse spectroscopy in the energy range from 0.2 keV to 12.0 keV. Two telescopes are equipped with the EPIC-MOS detectors (MOS stands for Metal Oxide Semiconductor). They provide a spatial resolution of ∼2 arcseconds. The third telsecope is equipped with the EPIC-PN detector, which provides a spatial resolution of ∼4 arcseconds. All three detectors allow – besides the energy

Figure A.2:
The X-ray observatory XMM-Newton. Identifiable are the three X-ray telescopes and the optical telescope.

information – for a precise timing information for each collected X-ray photon. In the case of the MOS detectors the time resolution is 1.5 ms, while for the PN detector the time resolution is 0.03 ms. XMM is also capable of dispersive spectroscopy. Two of the three telescopes have grating assemblies in their light paths and share the infalling X-rays with the reflection grating spectrometer (RGS). The RGS allows spectroscopy in the energy range 0.35 – 2.5 keV with a resolution of 0.04 Å(first order). The 30 cm reflector is called Optical Monitor (OM) and provides six filters for optical and ultraviolet wavelengths in the range 1800 – 6000 Å as well as two grisms for low resolution spectroscopy. The OM detector is a micro-channel plate intensified CCD and can operate in different imaging modes and in a timing mode with a resolution of 0.5 seconds. The possibility of simultaneous observations in the X-ray and optical/UV regime makes XMM-Newton an important instrument for observing cataclysmic variables.

A.3 The Hubble Space Telescope

The Hubble Space telescope (HST) was launched in April of 1990. It consists of one reflector with a primary mirror diameter of 2.4 meters. Due to the large number of detectors the usable wavelength range extends from the UV to the near-infrared. During its life time the HST has undergone four space shuttle based in-orbit service missions. These

Figure A.3:
The Hubble Space Telescope

missions made it possible to change, repair and update the detectors. The initial equipment in 1990 consisted of the imaging Wide Field/Planetary Camera (WFPC1), the Goddard High Resolution Spectrograph (GHRS), the Faint Object Spectrograph (FOS), the Faint Object Camera (FOC) and a High Speed Photometer (HSP). The first service mission in 1993 replaced the WFPC by the WFPC2 and improved the corrective optics. During the second service mission in 1997 the GHRS was replaced by the Near Infrared Camera / Multi Object Spectrometer (NICMOS) and the FOS was replaced by the Space Telescope Imaging Spectrograph (STIS). The third service mission was flown end of 1999 after one of the gyroscopes failed. It replaced the failed gyroscope and the onboard computers. In 2002 the Advanced Camera for Surveys (ACS) and a cooling facility for the NICMOS were added. A fifth service mission is planned for 2008, replacing the WFC2 with the WFC3 and installing the Cosmic Origin Spectrograph (COS).

A.4   The high speed photometer ULTRACAM

ULTRACAM is a high-speed CCD camera with a time resolution down to a few milli-seconds. It was designed and built by a team lead by the University of Sheffield including the UK Astronomy Technology Centre and the University of Southampton. The optical light beam is separated into three separate beams by two dichroic beamsplitters, thus allowing simultaneous observations in three different filters (u,g and r,i or z). The detector
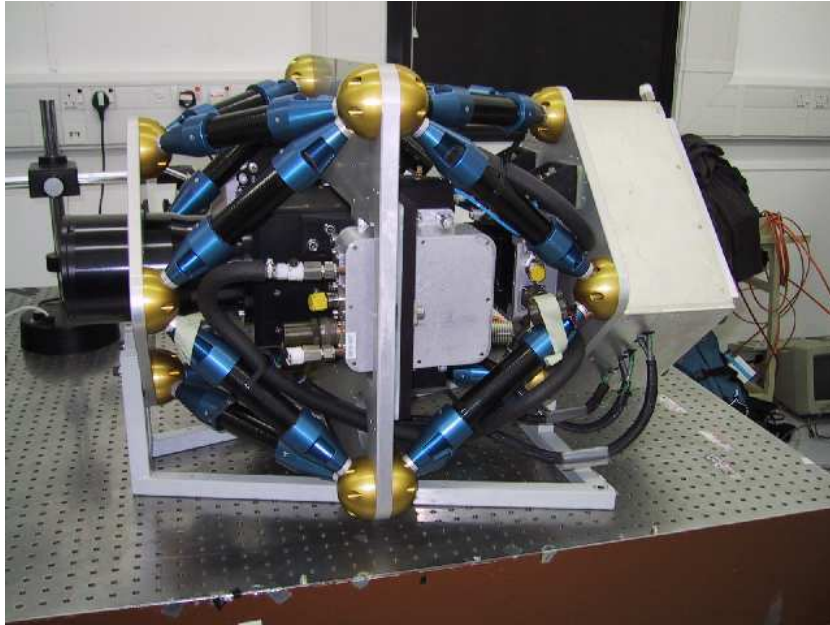
Figure A.4:
The finished ULTRACAM module as in 2002

system consists of back-illuminated, thinned frame transfer CCDs. The imaging area of
the CCD is 1024x1024. ULTRACAM was finalized in 2002 and since then used on a large
number of telescopes.

A.5   The high speed photometer OPTIMA

OPTIMA (**O**ptical **P**ulsar **TIM**ing **A**nalyzer) is a optical high-speed photometer originally
developed for the analysis of periodic changes in the intensity of pulsars at the Max-Planck-
Institut für extraterrestrische Physik Garching. The light from the focal plane of the
telescope is guided by seven fibre optics (and one additional fibre for measuring the sky
background) to a separate detector channel. The detector uses Avalanche photodiodes,
which have a greater quantum efficiency than the classically used photomultiplier, thus
it can reach a time resolution down to a few micro seconds. OPTIMA was completely
finalized in 2000, but was already used before for astronomical observations at different
telescopes - as the data used in this thesis show.

Bibliography

Andronov, N., Pinsonneault, M., & Sills, A. 2003, ApJ, 582, 358   15, 16, 105

Applegate, J. H. 1992, ApJ, 385, 621   106

Araujo-Betancor, S., Gänsicke, B. T., Long, K. S., et al. 2005, ApJ, 622, 589   15, 16

Baraffe, I., Chabrier, G., Allard, F., & Hauschildt, P. H. 1998, A&A, 337, 403   8

Beuermann, K. 2000, New Astronomy Review, 44, 93   8, 24, 25

Beuermann, K. 2004, in Astronomical Society of the Pacific Conference Series, Vol. 315, IAU Colloq. 190: Magnetic Cataclysmic Variables, ed. S. Vrielmann & M. Cropper, 187–+   51

Beuermann, K., Baraffe, I., & Hauschildt, P. 1999, A&A, 348, 524   25

Beuermann, K., Baraffe, I., Kolb, U., & Weichhold, M. 1998, A&A, 339, 518   9, 24, 25, 45

Beuermann, K. & Burwitz, V. 1995, in Astronomical Society of the Pacific Conference Series, Vol. 85, Magnetic Cataclysmic Variables, ed. D. A. H. Buckley & B. Warner, 99–+   40

Beuermann, K. & Weichhold, M. 1999, in ASP Conf. Ser. 157: Annapolis Workshop on Magnetic Cataclysmic Variables, ed. C. Hellier & K. Mukai, 283–+   25

Boffin, H. M. J., Steeghs, D., & Cuypers, J., eds. 2001, Lecture Notes in Physics, Berlin Springer Verlag, Vol. 573, Astrotomography   59

Borkovits, T. & Hegedues, T. 1996, A&AS, 120, 63   106

Bragaglia, A., Renzini, A., & Bergeron, P. 1995, ApJ, 443, 735   35

Bridge, C. M., Cropper, M., Ramsay, G., et al. 2002, MNRAS, 336, 1129   89, 90, 95

Brinkworth, C. S., Marsh, T. R., Dhillon, V. S., & Knigge, C. 2006, MNRAS, 365, 287   107, 110

Chabrier, G., Brassard, P., Fontaine, G., & Saumon, D. 2000, ApJ, 543, 216   37, 39

Chandrasekhar, S. 1935a, MNRAS, 95, 226 61

Chandrasekhar, S. 1935b, MNRAS, 95, 676 61

Chandrasekhar, S. 1939, An introduction to the study of stellar structure (Chicago, Ill.,
    The University of Chicago press [1939]) 61

Chanmugam, G. & Dulk, G. A. 1981, ApJ, 244, 569 32

Ciardi, D. R., Howell, S. B., Hauschildt, P. H., & Allard, F. 1998, ApJ, 504, 450 90

Clemens, J. C., Reid, I. N., Gizis, J. E., & O'Brien, M. S. 1998, ApJ, 496, 352 16

Cropper, M. 1988, MNRAS, 231, 597 33

Cropper, M., Wu, K., & Ramsay, G. 2000, New Astronomy Review, 44, 57 4, 11

Cruz, K. L. & Reid, I. N. 2002, AJ, 123, 2828 23, 24

Delfosse, X., Forveille, T., Ségransan, D., et al. 2000, A&A, 364, 217 25

Dhillon, V. S. & Watson, C. A. 2001, in Lecture Notes in Physics, Berlin Springer Verlag,
    Vol. 573, Astrotomography, Indirect Imaging Methods in Observational Astronomy, ed.
    H. M. J. Boffin, D. Steeghs, & J. Cuypers, 94–+ 75

Durney, B. R., De Young, D. S., & Roxburgh, I. W. 1993, Sol. Phys., 145, 207 15

Durney, B. R. & Latour, J. 1978, Geophysical and Astrophysical Fluid Dynamics, 9, 241
    15

Ferrario, L., Wickramasinghe, D., Bailey, J., & Buckley, D. A. H. 1995, in Astronomical
    Society of the Pacific Conference Series, Vol. 85, Magnetic Cataclysmic Variables, ed.
    D. A. H. Buckley & B. Warner, 336–+ 51

Fischer, A. & Beuermann, K. 2001, A&A, 373, 211 33, 36

Frank, J., King, A. R., & Lasota, J.-P. 1988, A&A, 193, 113 2

Frank, J., King, A. R., & Raine, D. J. 1985, Accretion power in astrophysics (Cambridge
    and New York, Cambridge University Press, 1985, 283 p.) 65

Gänsicke, B. T. 2000, Reviews of Modern Astronomy, 13, 151 6, 39

Gänsicke, B. T., Beuermann, K., & de Martino, D. 1995, A&A, 303, 127 34

Glenn, J., Howell, S. B., Schmidt, G. D., et al. 1994, ApJ, 424, 967 89, 90, 94

Greenhill, J. G., Hill, K. M., Dieters, S., et al. 2006, MNRAS, 372, 1129 110

Hagen, H.-J., Groote, D., Engels, D., & Reimers, D. 1995, A&AS, 111, 195 18

Hakala, P. J. 1995, A&A, 296, 164   90

Hakala, P. J., Watson, M. G., Vilhu, O., et al. 1993, MNRAS, 263, 61   89

Hall, D. S. 1989, Space Science Reviews, 50, 219   106

Hamada, T. & Salpeter, E. E. 1961, ApJ, 134, 683   62, 64

Harrop-Allin, M. K., Cropper, M., Hakala, P. J., Hellier, C., & Ramseyer, T. 1999, MN-RAS, 308, 807   90

Harrop-Allin, M. K., Potter, S. B., & Cropper, M. 2001, MNRAS, 326, 788   90

Hawley, S., Reid, I. N., & Gizis, J. 2000, in ASP Conf. Ser. 212: From Giant Planets to Cool Stars, ed. C. A. Griffith & M. S. Marley, 252–+   25

Heerlein, C., Horne, K., & Schwope, A. D. 1999, MNRAS, 304, 145   90

Hellier, C. & Naylor, T. 1998, MNRAS, 295, L50+   14

Hessman, F. V., Gänsicke, B. T., & Mattei, J. A. 2000, A&A, 361, 952   5

Horne, K. 1985, MNRAS, 213, 129   59

Howell, S. B., Ciardi, D. R., Sirk, M. M., & Schwope, A. D. 2002, AJ, 123, 420   89

Howell, S. B., Rappaport, S., & Politano, M. 1997, MNRAS, 287, 929   14, 15

Jones, B. F., Fischer, D. A., & Stauffer, J. R. 1996, AJ, 112, 1562   15

Kepler, S. O., Kleinman, S. J., Nitta, A., et al. 2007, MNRAS, 375, 1315   7

King, A. R. 1989, MNRAS, 241, 365   5

King, A. R. 1995, in Astronomical Society of the Pacific Conference Series, Vol. 85, Magnetic Cataclysmic Variables, ed. D. A. H. Buckley & B. Warner, 21–+   5

King, A. R. & Cannizzo, J. K. 1998, ApJ, 499, 348   5

King, A. R. & Lasota, J. P. 1979, MNRAS, 188, 653   3

King, A. R. & Schenker, K. 2002, in ASP Conf. Ser. 261: The Physics of Cataclysmic Variables and Related Objects, ed. B. T. Gänsicke, K. Beuermann, & K. Reinsch, 233–+   16

Kirkpatrick, J. D. & McCarthy, Jr., D. W. 1994, AJ, 107, 333   45

Kirkpatrick, J. D., Reid, I. N., Liebert, J., et al. 1999, ApJ, 519, 802   23

Knigge, C. 2006, MNRAS, 373, 484   8, 9, 53, 90, 94, 107

Koester, D. 2002, A&A Rev., 11, 33   6

Koester, D., Napiwotzki, R., Voss, B., Homeier, D., & Reimers, D. 2005, A&A, 439, 317   68

Koester, D. & Schoenberner, D. 1986, A&A, 154, 125   62, 64

Kolb, U. & Baraffe, I. 1999, MNRAS, 309, 1034   8, 15, 16

Kolb, U. & de Kool, M. 1993, A&A, 279, L5   15

Kolb, U., King, A. R., & Ritter, H. 1998, MNRAS, 298, L29+   16

Krzeminski, W. & Serkowski, K. 1977, ApJ, 216, L45   2

Kuijpers, J. & Pringle, J. E. 1982, A&A, 114, L4   2, 4

Lamb, D. Q. & Masters, A. R. 1979, ApJ, 234, L117   3

Landau, L. & Lifschitz, E. 1958, The Classical Theory of Fields (Pergamon, Oxford)   105

Lanza, A. F., Rodono, M., & Rosner, R. 1998, MNRAS, 296, 893   106

Leggett, S. K., Allard, F., Berriman, G., Dahn, C. C., & Hauschildt, P. H. 1996, ApJS, 104, 117   28, 30, 50

Li, J. & Wickramasinghe, D. T. 1998, MNRAS, 300, 718   15

Li, J., Wickramasinghe, D. T., & Wu, K. 1995, MNRAS, 276, 255   15, 39

Li, J. K., Wu, K. W., & Wickramasinghe, D. T. 1994a, MNRAS, 270, 769   15

Li, J. K., Wu, K. W., & Wickramasinghe, D. T. 1994b, MNRAS, 268, 61   15

Livio, M. & Pringle, J. E. 1994, ApJ, 427, 956   5

Marsh, T. R. & Horne, K. 1988, MNRAS, 235, 269   59

Martín, E. L., Delfosse, X., Basri, G., et al. 1999, AJ, 118, 2466   23

Nauenberg, M. 1972, ApJ, 175, 417   35, 62, 63, 64

Osborne, J. P., Giommi, P., Angelini, L., Tagliaferri, G., & Stella, L. 1988, ApJ, 328, L45   41

Pallavicini, R., Golub, L., Rosner, R., et al. 1981, ApJ, 248, 279   28

Pandel, D., Cordova, F. A., Shirey, R. E., et al. 2002, MNRAS, 332, 116   11

Panei, J. A., Althaus, L. G., & Benvenuto, O. G. 2000, A&A, 353, 970   35, 62, 64

Pizzolato, N., Maggio, A., Micela, G., Sciortino, S., & Ventura, P. 2003, A&A, 397, 147
28, 50

Podsiadlowski, P. 2004, http://www-astro.physics.ox.ac.uk/ podsi/lecture11_c.pdf 4

Radon, J. 1917, Berichte Sächsische Akademie der Wissenschaften Leipzig, 69, 262 59

Ramsay, G. & Cropper, M. 2007, MNRAS, 379, 1209 49

Ramsay, G., Cropper, M., Córdova, F., et al. 2001, MNRAS, 326, L27 4

Rappaport, S., Verbunt, F., & Joss, P. C. 1983, ApJ, 275, 713 13, 105

Reimers, D. & Hagen, H.-J. 2000, A&A, 358, L45 28

Reimers, D., Hagen, H.-J., & Hopp, U. 1999, A&A, 343, 157 18, 21, 24, 31, 35

Ritter, H. & Kolb, U. 2003, A&A, 404, 301 7

Schmidt, G. D., Szkody, P., Henden, A., et al. 2007, ApJ, 654, 521 28, 30

Schmidt, G. D., Szkody, P., Vanlandingham, K. M., et al. 2005, ApJ, 630, 1037 18, 28, 30, 39

Schreiber, M. R. & Gänsicke, B. T. 2003, A&A, 406, 305 37

Schwarz, R., Schwope, A. D., & Staude, A. 2001, A&A, 374, 189 18, 22, 24, 33, 39

Schwope, A. 2000, Indirect imaging of polars, Habilitation thesis, tU Berlin 12

Schwope, A., Hasinger, G., Lehmann, I., et al. 2000, Astronomische Nachrichten, 321, 1 50

Schwope, A. D. 1995, in Reviews in Modern Astronomy, Vol. 8, Reviews in Modern Astronomy, ed. G. Klare, 125–146 10

Schwope, A. D., Brunner, H., Buckley, D., et al. 2002a, A&A, 396, 895 40

Schwope, A. D., Brunner, H., Hambaryan, V., & Schwarz, R. 2002b, in ASP Conf. Ser. 261: The Physics of Cataclysmic Variables and Related Objects, ed. B. T. Gänsicke, K. Beuermann, & K. Reinsch, 102–+ 19, 32

Schwope, A. D., Hambaryan, V., Schwarz, R., Kanbach, G., & Gänsicke, B. T. 2002c, A&A, 392, 541 110

Schwope, A. D., Mantel, K.-H., & Horne, K. 1997, A&A, 319, 894 89, 90, 94

Schwope, A. D., Schwarz, R., Mantel, K., Horne, K., & Beuermann, K. 1995, in ASP Conf. Ser. 85: Magnetic Cataclysmic Variables, ed. D. A. H. Buckley & B. Warner, 166–+ 11, 90

Schwope, A. D., Schwarz, R., Sirk, M., & Howell, S. B. 2001, A&A, 375, 419   41, 54, 89, 90, 93, 95, 100

Schwope, A. D., Staude, A., Koester, D., & Vogel, J. 2007, A&A, 469, 1027   68

Schwope, A. D., Thomas, H. C., & Beuermann, K. 1993, A&A, 271, L25+   89, 90

Schwope, A. D., Thomas, H.-C., Mante, K.-H., Haefner, R., & Staude, A. 2003, A&A, 402, 201   90

Sills, A., Pinsonneault, M. H., & Terndrup, D. M. 2000, ApJ, 534, 335   15

Silvestri, N. M., Hawley, S. L., & Oswalt, T. D. 2005, AJ, 129, 2428   26

Sion, E. M. 1995, ApJ, 438, 876   6

Sion, E. M. 1999, PASP, 111, 532   6, 15, 53, 63

Smith, D. A. & Dhillon, V. S. 1998, MNRAS, 301, 767   7, 9

Sproats, L. N., Howell, S. B., & Mason, K. O. 1996, MNRAS, 282, 1211   90

Suh, I.-S. & Mathews, G. J. 2000, ApJ, 530, 949   63

Szkody, P., Harrison, T. E., Plotkin, R. M., et al. 2006, ApJ, 646, L147   68

Szkody, P., Henden, A., Mannikko, L., et al. 2007, AJ, 134, 185   40

Szkody, P., Homer, L., Chen, B., et al. 2004, AJ, 128, 2443   28, 30

Townsley, D. M. & Bildsten, L. 2002, in ASP Conf. Ser. 261: The Physics of Cataclysmic Variables and Related Objects, ed. B. T. Gänsicke, K. Beuermann, & K. Reinsch, 31−+   6

Townsley, D. M. & Bildsten, L. 2003, ApJ, 596, L227   39

Vennes, S., Fontaine, G., & Brassard, P. 1995, A&A, 296, 117   62, 64

Vennes, S., Thejll, P. A., Galvan, R. G., & Dupuis, J. 1997, ApJ, 480, 714   35

Verbunt, F. 1997, MNRAS, 290, L55   14

Verbunt, F. & Zwaan, C. 1981, A&A, 100, L7   13

Vogel, J. 2004, Diplomarbeit, Technische Universität Berlin   56, 90

Vrielmann, S. & Schwope, A. D. 2001, MNRAS, 322, 269   90, 95

Walkowicz, L. M., Hawley, S. L., & West, A. A. 2004, PASP, 116, 1105   26

Warner, B. 1995, Cataclysmic variable stars (Cambridge Astrophysics Series, Cambridge, New York: Cambridge University Press, —c1995) 1, 48

Watson, C. A., Dhillon, V. S., Rutten, R. G. M., & Schwope, A. D. 2003, MNRAS, 341, 129 90

Watson, M. G., King, A. R., & Williams, G. A. 1987, MNRAS, 226, 867 54

Webbink, R. F. & Wickramasinghe, D. T. 2002, MNRAS, 335, 1 14, 15

Webbink, R. F. & Wickramasinghe, D. T. 2005, in ASP Conf. Ser. 330: The Astrophysics of Cataclysmic Variables and Related Objects, ed. J.-M. Hameury & J.-P. Lasota, 137–+ 30, 39

Weicker, K. 2007, Evolutionäre Algorithmen (Teubner) 71

West, A. A., Hawley, S. L., Walkowicz, L. M., et al. 2004, AJ, 128, 426 26

Wheatley, P. J. 1995, MNRAS, 274, L51 15

Wickramasinghe, D. T. & Wu, K. 1994, MNRAS, 266, L1+ 15

Woelk, U. & Beuermann, K. 1996, A&A, 306, 232 4

Wood, J. H., Irwin, M. J., & Pringle, J. E. 1985, MNRAS, 214, 475 92

Wood, M. A. 1995, LNP Vol. 443: White Dwarfs, 443, 41 37, 62, 64

York, D. G., Adelman, J., Anderson, Jr., J. E., et al. 2000, AJ, 120, 1579 18

Zavala, R. T., McNamara, B. J., Harrison, T. E., et al. 2002, AJ, 123, 450 105

Zombeck, M. V. 1990, Handbook of space astronomy and astrophysics (Cambridge: University Press, 1990, 2nd ed.) 50

Publications

Refereed Publications

2008   Vogel, J., Byckling, K.J.K., Schwope, A., Osborne, J.P., Schwarz, R., Watson, M.G.: "Serendipituous discovery of a short-period eclipsing polar in 2XMM", submitted to Astronomy and Astrophysics

2007   Staude, A., Schwope, A.D., Schwarz, R., Vogel, J.,Krumpe, M., Nebot Gomez-Moran, A.: "The changing accretion states of the intermediate polar MU Camelopardalis", submitted to Astronomy and Astrophysics

Schwope, A. D., Staude, A., Koester, D., Vogel, J.: "XMM-Newton observations of EF Eridani: the textbook example of low-accretion rate polars" Astronomy and Astrophysics, 469, 1027S

Vogel, J., Schwope, A. D., Gänsicke, B. T.: "An in-depth study of the pre-polar candidate WX Leonis Minoris" Astronomy and Astrophysics, 464, 647V

2004   Schwope, A. D., Staude, A., Vogel, J., Schwarz, R.: "Indirect imaging of polars", AN, 325, 197S

Proceedings

2008   Vogel, J., Schwope, A. D., Schwarz R., Kanbach, G., Dhillon, V.S. and Marsh, T.R.: "On the orbital period of the magnetic cataclysmic variable HU Aquarii" High Time Resolution in Astrophysics Conference, Edinburgh, AIP Conf. Proc. 984,264 (2008)

2006   Vogel, J.., Schwope, A., Schwarz, R., Staude, A.: "Magnetic accretion in an extreme environment: the case of the low-accretion rate polar WX LMi", ESASP, 604, 311V